Monte Carlo Transport Methods for Semiconductor X-ray Imaging Detectors

by

Yuan Fang

A thesis
presented to the University of Waterloo
in fulfillment of the
thesis requirement for the degree of
Doctor of Philosophy
in
Electrical and Computer Engineering

Waterloo, Ontario, Canada, 2013

I hereby declare that I am the sole author of this thesis. This is a true copy of the thesis, including any required final revisions, as accepted by my examiners.

I understand that my thesis may be made electronically available to the public.

Abstract

This thesis describes the development of a novel comprehensive Monte Carlo simulation code, ARTEMIS, for the investigation of electron-hole pair transport mechanisms in a-Se x-ray imaging detectors. ARTEMIS allows for modeling of spatiotemporal carrier transport in a-Se, combining an existing Monte Carlo simulation package, PENELOPE, for simulation of x-ray and secondary electron interactions and new routines for electron-hole pair transport with three-dimensional spatiotemporal signal output considering the effects of applied electric field. The detector Swank factor, an important imaging performance metric is calculated from simulated pulse-height spectra and shown to depend on incident x-ray energy and applied electric field. Simulation results are compared to experimental measurements and are found to agree within 2%. Clinical x-ray spectra are also used to study detector performance in terms of energy weighting and electronic noise. Simulation results show energy-weighting effects are taken into account in the ARTEMIS model, where the Swank factor and DQE have a higher dependence on the high-energy incident x rays due to increased carrier yield. Electronic noise is found to widen the pulse-height spectra and degrade the Swank factor. The effect of recombination algorithms and burst models are studied. A comparison of a first-hit algorithm and a nearest-neighbor approach shows no significant difference in the simulation output while achieving reduced simulation time. The examination of the initial generation of carriers in the burst shows that the recombination efficiency of carriers is dependent on the carrier density and electric field. Finally, the spatial resolution characteristics of a flat-panel a-Se detector are studied by using the ARTEMIS model for spatial output and image generation. The modulation transfer functions are calculated from simulated detector point response functions for monoenergetic and clinical radiation qualities.

Acknowledgements

I consider myself very fortunate to have Professor Karim S. Karim from University of Waterloo and Dr. Aldo G. Badano from the U.S. Food and Drug Administration (FDA) as cosupervisors, and for their constant support and advice that led me to numerous academic accomplishments during the course of my degree. I am particularly grateful for the chance to pursue my research interests at the FDA. I am deeply indebted to my parents, Dr. Yabin Fang and Xuehui Liu, for their continuing encouragement and support.

Much of this work could not have been completed without the effort of others from the University of Waterloo Silicon Thin-film Applied Research (STAR) group. Many thanks go to Dr. Nicolas Allec for many insightful discussions, Dr. Kai Wang, Shiva Abbaszadeh, Dr. Hasibul Majid for their help in laboratory training and assistance in the fabrication of a-Se devices needed for experiments.

I am indebt to everyone in the Division of Imaging and Mathematics, Office of Science and Engineering Laboratory, Center for Device and Radiological Health, FDA, for a pleasant and rewarding experience. In particular, I would like to thank Dr. Andreu Badal and Diksha Sharma for their Monte Carlo modeling and simulation efforts, and Dr. Robert Jennings, Dr. Cecilia Marini-Bettolo and Eugene O'Bryan for their help in the spectroscopy laboratory. In addtion, I am thankful for the support from the division director, Dr. Kyle Myers to pursue collaborations with industry.

I am appreciative of the help provided by the people at FUJIFILM, especially Robert Uzenoff, Yuuichi Hosoi, Takaaki Itou, and Fumito Nariyuki for a fruitful collaboration with flat panel detector characterizations. I would like to acknowledge Mitsui Canada Scholarship (Grand prize, Ontario Japanese Speech Contest) for partially supporting this effort.

In addition, I am thankful for the opportunity to exchange at the University of Maryland Fischell Department of Bioengineering to further my academic training and many friendships: Samir Abboud, Mina Choi, Joel Wang, Kimberly Konston, and Han Dong. This opportunity was supported in part by an ORISE Fellowship administered through US Department of Heath and Human Services (HHS) and Department of Energy (DOE).

I would like to thank the Government of Canada for its support of my research in the form of the NSERC Alexander Graham Bell Canada Graduate Scholarship, and the University of Waterloo President's Graduate Scholarship and the Faculty of Engineering Carl A. Pollock Fellowship award. This also include the Department of Electrical and Computer Engineering (E&CE) for the numerous teaching assistantships, scholarships and travel assistance funds to conferences.

Lastly, my everlasting gratitude goes to Crystal Zhang for her immense support of my work. And to Maran Ma, Janice Cheng, Namratha Rajagopal, Ling Guo and Hugo de las Heras, the best friends money can't buy − couldn't have done it without you.

Contents

List of Tables

List of Figures

List of Abbreviations

Symbol	Descriptions	Value and/or units
A	Detector area	cm^2
α	Linear attenuation coefficient	cm^{-2}
c	Velocity of light in vacuum	$2.9979x10^8$ m s^{-1}
CT	Computed tomography	
D	Diffusion coefficient	cm^2s^{-1}
DQE	Detective Quantum Efficiency	
e	Electron charge	$1.6022x10^{-19}$ C
E_{app}	Applied electric field	V μm^{-1}
E_{ehp}	Bandgap energy	eV
FFDM	Full field digital mammgraphy	
I(E)	Swank factor or Information factor	
$L_{detector}$	Detector thickness	μm
$L_{diffusion}$	Diffusion distance	nm
λ	wavelength	m
MTF	Modulation transfer function	
m_e	Electron mass	$9.1094x10^{31}$ kg
μ	Carrier mobility	cm^2 V^{-1} s^{-1}
η_{QE}	Quantum efficiency	
η_{recomb}	Recombination efficiency	
$P_{trapping}$	Trapping probability	
r_{burst}	Burst radius	nm
r_0	Thermalization distance	nm
Δt	Simulation time step	s
$\tau_{trapping}$	Trapping time	s
v_p	Photon frequency	Hz
ω_{pe}	Plasmon frequency	Hz
W_0	Ionization energy	eV
Z_{eff}	Effective atomic number	

Chapter 1

Introduction

1.1 Overview and aim

X-ray detectors are important components of medical imaging, security screening, spectroscopy, dosimetry and industrial imaging systems. Semiconductor detectors are advantageous for these applications because of their good energy resolution, high efficiency, and high carrier yield[12]. Semiconductor detectors employ photoconductive materials such as silicon, germanium, and amorphous selenium to convert x rays directly into electric signal. In medical imaging applications, semiconductor detectors are used in a wide range of modalities including general radiography, full-field digital mammography (FFDM) and computed tomography (CT)[13, 14]. Semiconductor materials such as stabilized a-Se and other high-Z materials have recently emerged as candidates for new imaging technologies including breast tomosynthesis and photon-counting mammography[15, 16].

Monte Carlo methods can be used for the study of charge generation and transport in semiconductors materials, for design validation and optimization of imaging systems. An open-source MC package (MANTIS) already exists for modeling indirect detectors[17], and some simulation models have been previously proposed and developed for direct detectors [18, 19, 20, 21, 22]. However, no comprehensive, open-source simulation tool exists for imaging applications with direct detectors.

The purpose of this work is to evaluate the assumptions and limitations of previous models, and develop a simulation code for performing fully detailed Monte Carlo simulation of carrier transport and recombination processes in photoconductor x-ray detectors. This work describes a novel method for complete Monte Carlo tracking of x rays, energetic

electrons and electron-hole pairs to characterize the signal statistics and image quality metrics in a-Se direct x-ray detectors. The objectives of this research are:

1. Investigate the use of Monte Carlo methods to model transport of charged carriers in semiconductor x-ray imaging detectors, and develop a simulation code for modeling the complete signal formation process.

2. Validation of the simulation models with experimental comparisons, such as Swank factor as a function of incident energy and applied electric field, and the modulation transfer function.

3. Perform simulation studies of a-Se x-ray detector using the simulation code and material specific parameters to investigate different effects and models on the detect performance.

1.2 Thesis layout

The focus in this thesis is primarily on Monte Carlo modeling of semiconductor x-ray detectors for medical imaging applications. First, background on x-ray radiation, x-ray imaging detectors and photoconductive materials used for x-ray detection are presented in Chapter 2. Methods of x-ray generation are compared taking into account the physics of atomic x-ray interactions and possible impacts on experimental measurements. Possible photoconductor candidates for x-ray detection are compared in terms of absorption efficiency, sensitivity, transport properties and dark current.

Previous work in the area of modeling of x-ray detectors is reviewed in Chapter 3, including a brief overview of existing Monte Carlo simulation models used for both direct and indirect detectors. Some simulation codes focus only on the primary x-ray and high-energy electron interactions, while other focus on the transport of secondary carriers such as optical photons for indirect detectors, and electron-hole pairs for direct detection. This chapter also provides a brief overview of the methodology of pulse-height spectroscopy and experimental challenges.

Chapter 4 describes the proposed Monte Carlo simulation model, using a combined approach for modeling x-ray radiation transport in direct detectors. The x-ray and secondary electron interactions are modeled with PENELOPE, and a transport simulator is developed for charge generation and transport of electron-hole pairs. The theory and implementation of these models are also covered in detail. Pulse-height spectra (PHS) simulations can be

used to study the spectral response of the detector to different x-ray inputs, and useful for calculation of performance metrics such as the Swank factor. Monoenergetic x-ray inputs are preferred because it shows the detector spectral response at each x-ray energy and gives more details to the detector performance at each energy. This chapter als contain PHS simulations and the comparison to experimental measurements with monoenergetic x-rays.

Chapter 5 includes simulation studies with clinical x-ray spectra used in mammography. The effect energy weighting and electronic noise on the detector Swank factor and the DQE at zero spatial frequency are studied. This chapter also contain an optimization study of clinical spectra for a-Se detectors.

The effects of different recombination algorithms and burst models on detector performance are explored using the simulation code in Chapter 6. This chapter contains the theoretical and MC comparison of recombination fractions for single electron-hole pairs. The MC model for single electron-hole pair is extended for multiple electron-hole pairs via the burst model, and the effect of applied electric field and x-ray energy is studied for clinical x-ray spectra.

Chapter 7 describes the spatial resolution study of flat-panel a-Se detector. Image quality measurements are made following International Electrotechnical Commission (IEC) guidelines using a prototype a-Se detector provided by FUJIFILM Corporation. The modulation transfer function (MTF), normalized noise power spectra (NNPS) and detective quantum efficiency (DQE) are measured as a function of spatial frequency, applied electric field, and detector thickness. The point responses are simulated to determine the pre-sampled MTF and are compared with experimental measurements. Lastly, Chapter 8 concludes this research and summarizes the contributions of this thesis to the field of x-ray medical imaging.

Chapter 2

Background

2.1 X rays

X rays were discovered by Professor Wilhelm C. Roentgen of Wuerzburg University, Germany in 1895, and the first x-ray image was captured later that year. Professor Roentgen was awarded the first Nobel Prize in physics for his contributions in the field of science[23]. X rays are a part of the electromagnetic spectrum and are located between ultraviolet and gamma rays. High-energy electron interactions produce x rays, and emissions from nuclear reactions are called gamma rays. An x-ray photon can have a wavelength of 0.01 nm to 10 nm. X-ray energy is proportional to frequency and inversely proportional to the wavelength[24]:

$$E = hf = h\frac{c}{\lambda} \ , \tag{2.1}$$

where h is the Planck's constant, c is the speed of light, f is the frequency, and λ is the wavelength.

2.1.1 X-ray generation

X rays can be generated from an x-ray tube. An x-ray tube is made up of a cathode and anode assembly sealed in high vacuum. The cathode assembly encloses a filament circuit containing a thin thoriated Tungsten wire (filament). When a current is passed through the filament, the electrical resistance causes the filament to heat up and discharge

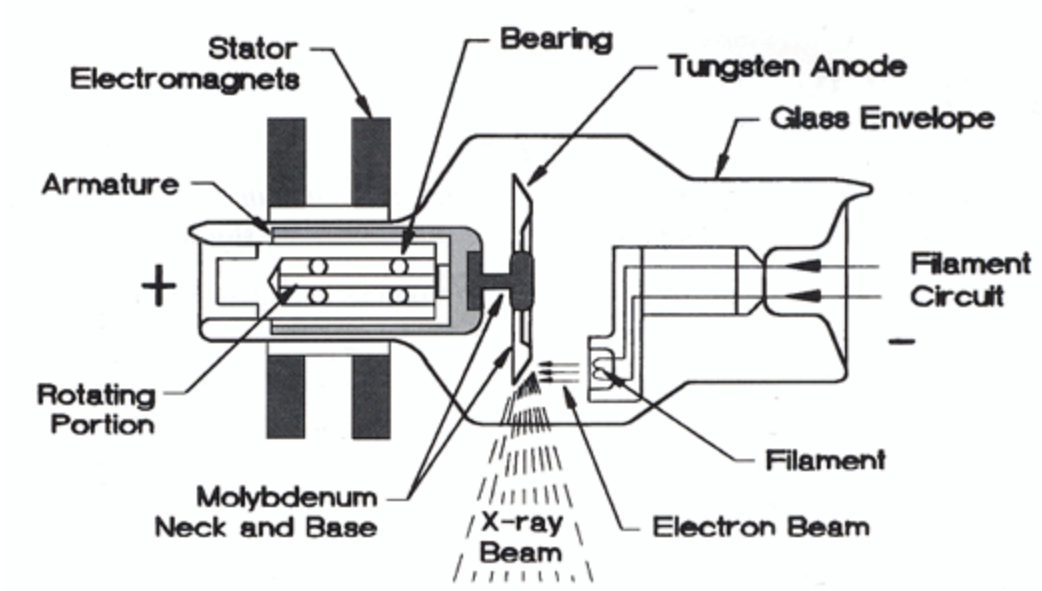

Figure 2.1: Schematic of an x-ray tube. The rotating tungsten anode in the center of the tube is enclosed in vacuum. On the left side is the rotor with an armature connected to the anode. On the right is the cathode assembly consisting of the filament wire and circuit used to produce beam of electrons[1].

electrons in a process called thermionic emission. The anode consists of a target often made of tungsten or molybdenum. When a high voltage (kVp) is applied, the electrons from the cathode accelerate toward the anode, striking the target both by collisional and radiative transfer. The schematic diagram of an x-ray tube is shown in Figure 2.1[1].

The generation of x rays with an x-ray tube is an inefficient process, and only about 1 percent of the energy deposited lead to x rays and the remaining 99 percent turns into heat. Rotating anodes are used to prevent the target from melting, and can rotate up to 10,00 revolutions per minute (rpm). In addition, anode cooling curves and convection cooling in the tube housing are used to prevent overheating. An x-ray spectrum with a Tungsten anode for 32 kVp (peak kilovoltage) is shown in Figure 2.2.

The majority of the x rays produced are due to Bremsstralung (radiative transfer) and also some characteristic x rays are produced (collisional transfer). The Bremsstralung x rays range from 0 to the maximum kVp applied to be x-ray tube. While the characteristic x-ray fluorescent energies are dependent on the material properties. For medical imaging applications, a filter is used to absorb low-energy x-ray photons that have low penetrability

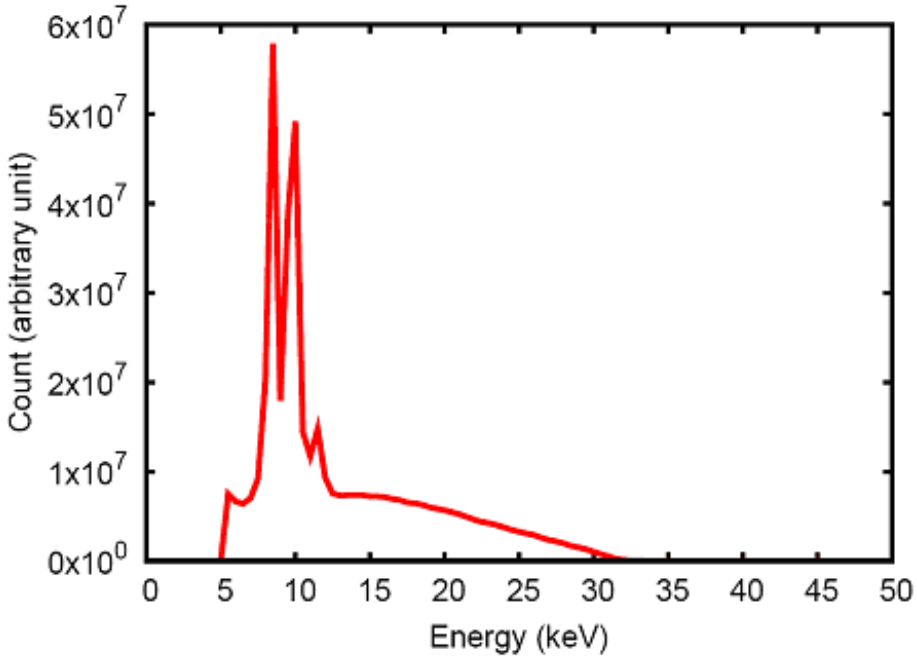

Figure 2.2: Calculated x-ray spectrum for a tungsten anode with peak tube voltage of 32 kVp. The y-axis is a linear scale counting the number of x rays, the x-axis is the energy of the x rays produced.

to reduce patient exposure. The most common material used to filter x rays is aluminum (1-2 mm thick), which is considered the standard x-ray filter material. Filters can be used to significantly "harden" the x-ray beam.

A radioisotope is an atom with an unstable nucleus, and undergoes radioactive decay that can emit alpha particles, beta particles, gamma rays and x rays or some combination. An element and its isotope have the same number of protons, and the same chemical behavior. However, the number of neutrons is different, which causes the nucleus to be unstable. Some radioisotopes occur naturally and some can be synthesized in nuclear reactions. Radioisotopes are very useful as a source of radiation, because they have clearly defined energies for the emitted gamma rays.

2.1.2 X-ray attenuation

Attenuation is the gradual loss in intensity, and the amount of incident x rays attenuated by the photoconductor is directly proportional to the number of generated charge carriers with a significant impact on the performance of the direct x-ray system. When a beam of x-ray photons impinge onto a photoconductor, some photons are absorbed in the material leading to a decrease in the intensity of the transmitted beam. Increasing the thickness of the photoconductor, $L_{detector}$, leads to an increase in absorption. The absorption capability of a photoconductor is directly proportional to its thickness and is modeled by the performance parameter, quantum efficiency (QE)[25]:

$$\eta = 1 - e^{-\alpha L_{detector}} \ . \tag{2.2}$$

The quantum efficiency, η, is dependent on the linear attenuation coefficient, α, and thickness of the material, $L_{detector}$. As the thickness increases, the exponential term approaches zero, and theoretically, the quantum efficiency of the detector becomes effectively 100%. Figure 2.3 shows the x-ray interaction quantum efficiency for selenium as a function of detector thickness and x-ray energy. As the detector become thicker, more x-ray photons are attenuated, leading to a higher quantum efficiency. Quantum efficiency is also dependent on the x-ray photon energy.

The linear attenuation coefficient is the fraction of photons removed from a monoenergetic beam of x rays per unit thickness of the given material. For a given thickness, the probability of interaction is dependent on the number of atoms per volume. This dependence can be overcome by normalizing the linear attenuation coefficient for the density of the material. The mass attenuation coefficient is the linear attenuation coefficient normalized to unit density. The mass energy transfer coefficient is the mass attenuation coefficient multiplied by the fraction of the energy of the interacting photon that is transferred to charged particles as kinetic energy (due to scattering). Mass energy absorption coefficient is the fraction of the mass attenuation coefficient that gives rise to the initial kinetic energy of electrons in a small volume of absorber[26].

2.1.3 X-ray interactions

In the diagnostic x-ray range, the absorbed photon can interact within the photoconductor via three main mechanisms: photoelectric absorption (or photoelectric effect), Compton scattering and Rayleigh scattering. Figure 2.4 and 2.5 show the atomic models of these

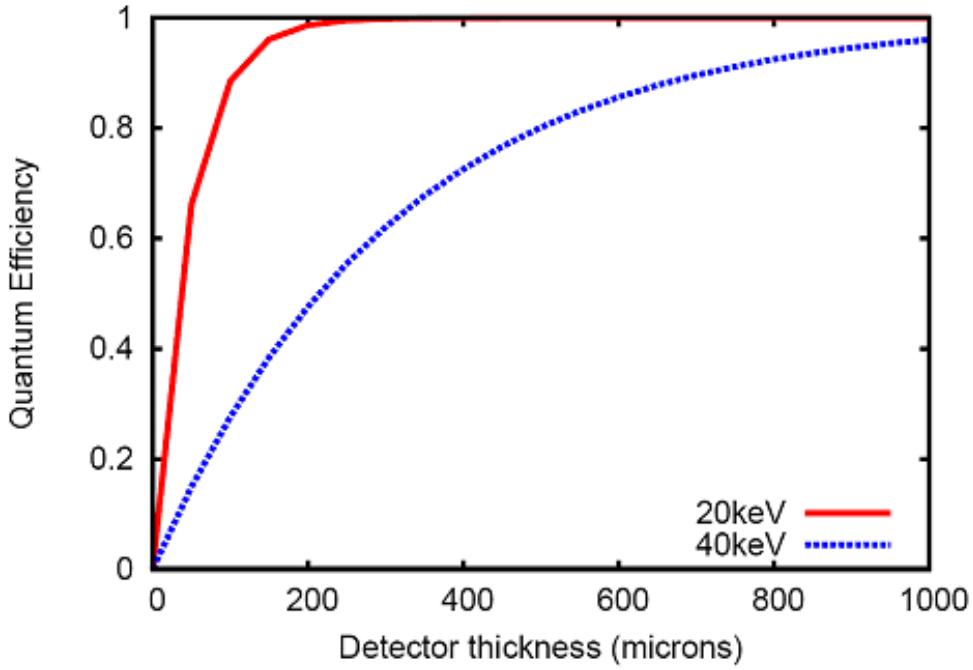

Figure 2.3: X-ray interaction quantum efficiency as a function of thickness and incident photon energy. The red curve is the quantum efficiency for a-Se with 20 keV x rays. The QE increases as a function of detector thickness, and saturates at 1 with thicknesses greater than 300 μm. For 40 keV x-ray photons (the blue curve in the plot), QE increases more gradually with thicker detectors, almost reaching 1 at 1000 μm.

interactions. During photoelectric absorption, the incident x ray ionizes an atom by transferring all of its energy to an inner shell electron that is ejected from the atom shown in Figure 2.4. The kinetic energy of this ejected photoelectron can be calculated from the difference between the incident photon energy, E_{photon} and the binding energy of the orbital electron, $E_{bindingEnergy}$[27]:

$$E_{photoelectron} = E_{photon} - E_{bindingEnergy} \ . \tag{2.3}$$

A more outer-shell electron may fill the vacancy in the inner-shell and generate a characteristic x ray or Auger electron. The photoelectric absorption is the dominant interaction mechanism in the diagnostic x-ray energy range for a-Se, and leads to generation of many electron-hole pairs in direct x-ray photoconductors.

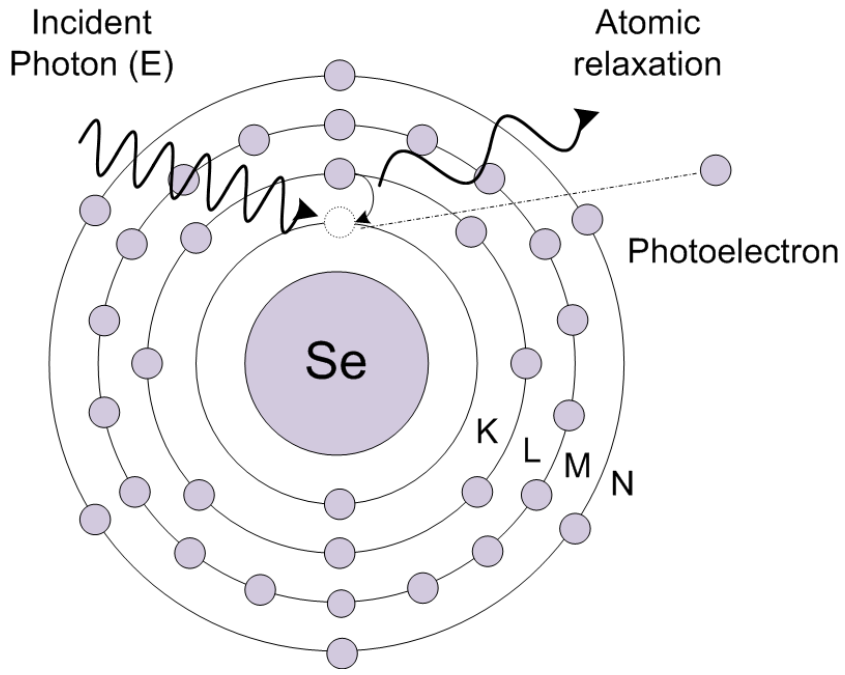

Figure 2.4: Photoelectric absorption process in a selenium atom. The incident x ray photon interacts directly and ionize a inner K-shell electron, transferring majority of its energy and creating a photoelectron. To reach the lowest energy state, fluorescent x rays may be produced and atomic relaxation may occur for an outer shell electron to fill the space left by the photoelectron.

Rayleigh (coherent) scattering is the interaction between an incident photon and the whole atom, where the energy of the atom and the scattered x ray remain unaltered. Compton (incoherent) scattering is the interaction between an incident photon and an outer-shell electron. The Rayleigh and Comptom scattering interactions are shown in Figure 2.5. Compton scattering yield a high-energy Compton electron and the incident photon is scattered. Generally, Compton scattering leads to a noisier images and is not desired in diagnostic imaging.

2.2 X-ray imaging

From its initial discovery, the medical application of x rays was evident. X rays are observed to be able to identify skeletal structures, and x-ray imaging (radiology) quickly developed

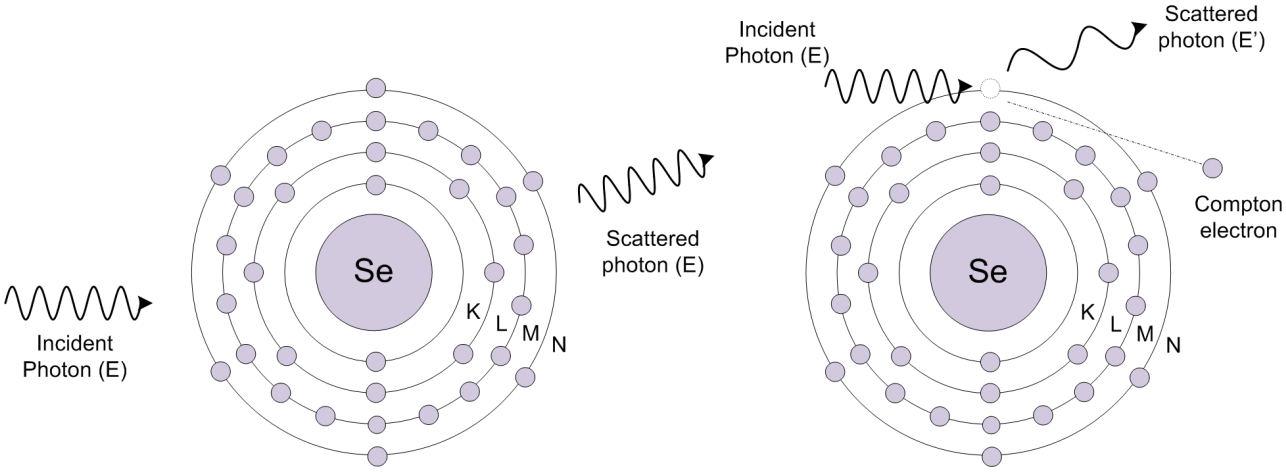

Figure 2.5: (a) Rayleigh scattering process in a selenium atom. The incident photon interacts with the entire atom as oppose to an individual electron as in photoelectric absorption or Compton scattering. During Rayleigh scattering, the photon retain all of its energy and is only scattered to a different direction. (b) Compton scattering process in a selenium atom. Compton scattering results in the ionization of an electron in the outer shell of the atom creating a Compton electron. The incident photon loses some energy and is scattered.

as a branch in medicine. For the x-ray spectrum, energy ranges from several hundred electron volts (eV) to hundreds of kilo electron volts (keV). X rays with low energy are considered soft x rays, and high-energy x rays are considered to be hard x rays. For the purpose of medical imaging, x rays with energies at the keV range are used, because they are considered hard x rays with penetrability of the tissue. Furthermore, for different imaging modalities, the x-ray detector is designed for different energies and pixel sizes. Table 2.1 summarizes typical x-ray imaging parameters for the purpose of mammography, fluoroscopy and chest x-ray modalities[28].

Table 2.1: Modalities of medical x rays and typical parameters.

Application	Mammography	Fluoroscopy	Chest x-ray
Mean x-ray energy	20 keV	40 keV	70 keV
Tube peak voltage	30 kVp	70 kVp	120 kVp
Detector size	18 x 24 cm^2	25 x 25 cm^2	35 x 43 cm^2
Pixel size	50 x 50 μm^2	250 x 250 μm^2	200 x 200 μm^2
Number of pixels	3600 x 4800	1000 x 1000	1750 x 2150

Mammography and chest x ray are projection radiography techniques used to image the breast and chest surrounding areas; fluoroscopy is a real-time imaging technique used to take moving images of internal structures of a patient. From Table 2.1, mammography, compared to all other applications, employs the least amount of energy, with a mean energy of 20 keV and maximum peak energy of 30 kVp. This is because mammography is imaging the soft tissues of the breast and does not require penetrability with high energies to see bone tissues. In comparison, chest x ray uses the highest energy at a mean energy of 70 keV and maximum peak energy of 120 kVp, because the incident chest x-ray photons require high energies to penetrate the skeletal structures. Mammography detectors have the smallest detector size but also the smallest pixel size, this allows for the highest resolution to identify small tumors and calcifications. For chest x ray, even though the detector is large, the pixels are relatively large too, which reduces patient exposure and therefore helps to avoid damage to vital organs. The many advantages of digital x-ray detector technology (described in the following sections), such the fast readout times and ability to save the images electronically, have also supported the development of emerging imaging modalities such as breat tomosynthesis[15].

Digital x-ray detection is an active area of research because traditional x-ray detectors are film-based and have many disadvantages: the readings are analog and cannot be stored electronically; the film cassettes are often bulky, expensive and easy to damage; additionally, the development time of the x-ray film often lead to patient waiting time and delayed diagnosis. Figure 2.6 depicts the traditional film-based x-ray system[2].

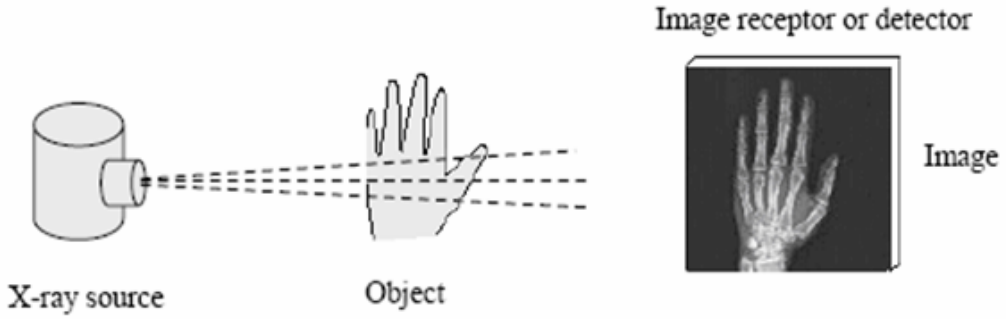

Figure 2.6: Illustration of a traditional film-based x-ray system consisting of an x-ray source[2], image receptor or detector and the object to be imaged. Depending on the object composition, the incident x rays are attenuated. The difference in the amount of x rays that reaches the detector lead to an image.

Digital x-ray detectors are film-less and converts the x-ray radiation directly into elec-

tric signals to form a digital image shown in Figure 2.7[2]. This x-ray image is stored electronically in real time, saving the patient and physician precious time making real time diagnosis possible.

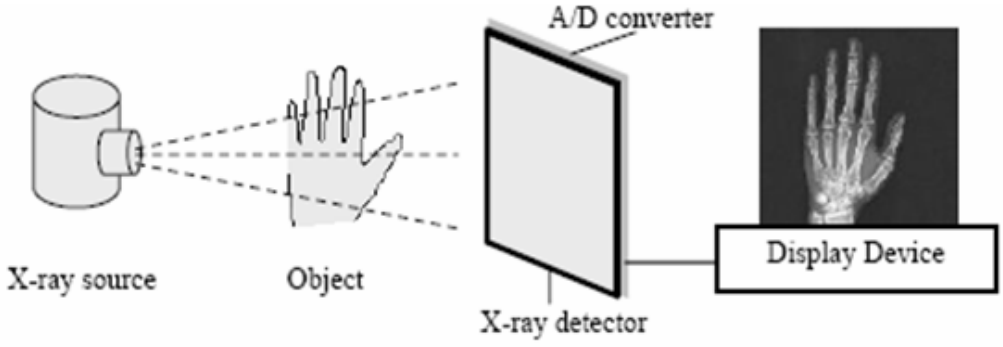

Figure 2.7: Illustration of a digital x-ray system[2]. In comparison to film-based systems, an analog to digital (A/D) converter is used to translate incident x rays into a digtial signals. Digital images can be conveniently stored, shared and displayed.

Another advantage of digital x-ray systems is the ability to electronically transfer x-ray images with its original quality and clarity. With digital x-ray images, physicians can consult with other doctors for a second opinion to improve the accuracy of diagnosis. There are two methods of digital x-ray detection: the indirect method with scintillator based detectors, and direct method with semiconductor based detectors.

2.2.1 Scintillator-based detectors

In scintillator-based detectors, a phosphor scintillator converts x-ray photons into multiple optical light photons detected as electric signals in a photodiode or photomultiplier tube, hence an indirect conversion process[29]. Figure 2.8 shows the structure of a scintillator detector.

One of the advantages of indirect detection method is the high absorption efficiency of the scintillator material (e.g. CsI) capable of absorbing a high percentage of incident x-ray photons. However, one disadvantage of the indirect method is the loss of resolution due to isotropic generation of optical photons[30], shown in Figure 2.8. Thinner scintillator material can be used to limit the effect of spreading, however at a cost of reduced absorption efficiency of incident x rays. Scintillators with columnar phosphor structures are also used to confine and reduce the spreading of optical photons[31].

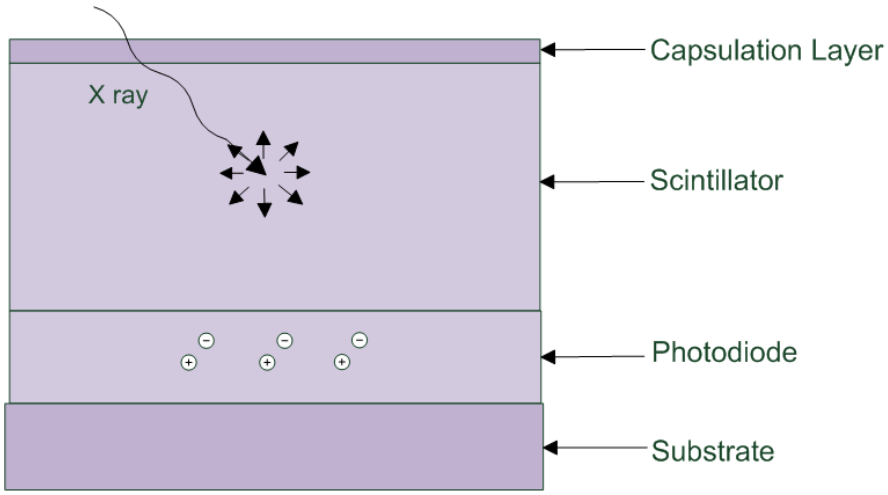

Figure 2.8: Indirect conversion process in scintillator based digital x-ray imaging detectors. The layered detector structure consists of a scintillator and photodiode sandwiched between a substrate and capsulation. The scintillator material is used to absorb and convert high-energy x ray photons into optical photons in an isotropic process. The emitted optical photons are detected by a photodiode and read out to form a digital image. Due to the isotropic nature of optical photon generation in the scintillator, indirect detectors have an inherent limit on image resolution.

2.2.2 Semiconductor-based detectors

In semiconductor-based detectors, x-ray photons are absorbed in the photoconductor and converted directly into charge carriers called electron-hole pairs (EHPs). Figure 2.9 is an illustration of the direct conversion method. As x-ray photons are absorbed in the photoconductive material, many electron-hole pairs are generated near the region of interaction, and are eventually collected at the electrodes[32].

Due to the direct conversion process, resolution of semiconductor x-ray detectors depends only on the spreading of the incident x-ray photons, secondary high-energy electrons and electron-hole pairs. In general, photoconductive materials used in semiconductor detectors have lower atomic numbers compared to scintillators, and require a thicker detector to absorb the same amount of incident x rays[26]. Often a biasing voltage is used to collect the electron-hole pairs and blocking or (electron/hole) transport layers are used to prevent leakage. Figure 2.10 shows a commercially available amorphous selenium (a-Se) direct x-ray detector developed by ANRAD Corporation (http://www.anrad.com/products-direct-xray-detectors.htm).

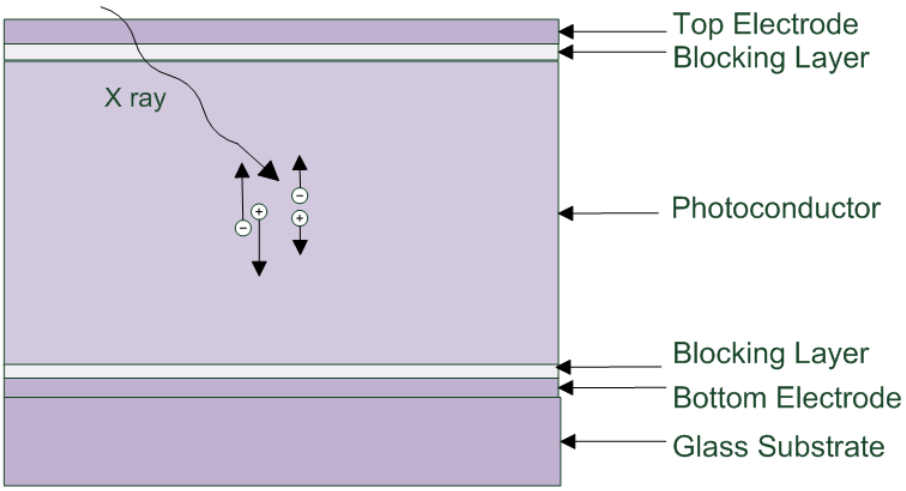

Figure 2.9: Direct conversion process in semiconductor based x-ray detectors. The layered detector structure consist of a photoconductor sandwiched between blocking layers and electrodes sitting on a glass substrate. The photoconductor is a semiconductor material capable of absorbing and converting incident x-ray photons directly into electric signal. Due to the large number of charge carriers generated, an applied bias is used to facilitate in the charge collection and transport. Upon carrier generation, charge carriers under the influence of the electric field flow to opposing electrodes to be detected. Blocking layers are used to prevent leakage and reduce dark current in the detection process.

2.3 Photoconductors

X-ray detectors contain photoconductive materials that will absorb the energy of the incident x ray and convert it to electrical signals to generate the digital x-ray image. For good performance, an x-ray photoconductor needs to have the following[33]:

1. Good absorption of incident x-ray photons with a practical thickness.
2. Good signal response with many secondary carriers generated from x-ray exposure.
3. Good carrier transport and collection, minimal loss of carriers.
4. Good material stability and uniformity for large areas.

Figure 2.10: Commercial a-Se semiconductor direct x-ray detector for full-field digital mammography (FFDM).

Table 2.2 summarizes the properties of several photoconductor materials that have been investigated for direct x-ray detection. X-ray absorption is dependent on the photoconductor atom size, where the effective atomic numbers are calculated based on the Murty formula[34]:

$$Z_{eff} = \sqrt[2.94]{f_1(Z_1)^{2.94} + f_2(Z_2)^{2.94} + f_3(Z_3 + ...)^{2.94}} \,, \tag{2.4}$$

where f_n is the fraction of the total number of electrons associated with each element, and Z_n is the atomic number of each element. The computed effective atomic numbers for CdZnTe, HgI_2, PbO and Se are 50, 67, 74 and 34 respectively. As the Z_{eff} increases, the attenuation coefficient of the material increases as well, leading to higher absorption.

Sensitivity is dependent on the number of EHPs generated, and is a function of maximum collectable charge, Q_0[2]:

$$Q_0 = \frac{5.46x10^{16} eAX\alpha_{photoconductor}}{E_{ehp}(\alpha/\rho)_{air}} \int_0^\infty e^{\alpha x} = \frac{5.46x10^{16} eAX}{E_{ehp}(\alpha/\rho)_{air}} \frac{\alpha_{photoconductor}}{\alpha_{air}} \,, \tag{2.5}$$

Table 2.2: Comparison of photoconductors: CdZnTe, HgI_2, PbO, and Se.

	CdZnTe	HgI_2	PbO	a-Se
X-RAY ABSORPTION				
Z_{eff}	50	67	74	34
ELECTRIC SIGNAL				
Band gap (eV)	1.7	2.1	1.9	2.3
Sensitivity (μC/R/cm^2)	24	10	-	0.2
CHARGE COLLECTION				
Hole mobility-lifetime (cm^2/V)	1.0x10^{-4}	1.0x10^{-7}	5.0x10^{-7}	0.6-6.0x10^{-5}
Electron mobility-lifetime (cm^2/V)	5.0x10^{-4}	1.5x10^{-5}	5.0x10^{-7}	0.3-3.0x10^{-6}
DARK CURRENT				
Dark current (nA/cm^2)	7	0.2-1.8	5	0.01

the maximum collectable charge is a function of x-ray exposure, X, detector area, A, elementary charge, e, and absorption coefficient ratio of photoconductor material and air, $\alpha_{photoconductor}/\alpha_{air}$. High sensitivity is desired because more collectable charges lead to an increase in the output electric signal. Charge collection is dependent on the carrier mobility-lifetime product and the applied bias. Even though high mobility-lifetime is desired, the detector can be externally biased with high applied electric field to significantly decrease the carrier transit time and increase the number of charges collected. However, the material stability is a big concern due to two reasons: change in morphology over time and change in performance due to temperature. Due to exposure and time, the morphology of the material may change, causing degradation in sensitivity and material transport properties. For example, a-Se based detectors are amorphous, and crystallize over time. Polycrystalline grain boundaries act as traps, greatly reducing the carrier mobility product and the detector sensitivity. Uniformity and material properties for large area coating is highly dependent on the fabrication technique and will be discussed in detail in the following subsections. For performance change due to temperature, the dark current of HgI_2 can be used as an example to demonstrate this point discussed in Section 2.3.3.

2.3.1 Amorphous selenium

Selenium has an atomic number (Z) of 34, and the outer shell contains six valence electrons with a density of 4.79 g/cm^2. For a-Se, a lower density ranging from 3.5 to 4.5 g/cm^2 have been reported by Yun *et al.*, and Lachaine *et al.* due to different outer shell cross-section compared to atomic Se[20, 35]. Inherently, a-Se is not stable and crystallizes over time,

which is not a desirable property in a detector material. To minimize this problem, arsenic (As), approximately 0.2 to 0.5% of the bulk material, is mixed with a-Se to stabilize the structure. Although arsenic prevents crystallization, it also causes more traps to be formed in the bulk a-Se, thereby reducing the charge collection. In order to improve the charge transport properties, Chlorine (Cl) is doped, nominally at 20 ppm to reduce traps[36]. Figure 2.11 shows the stabilized selenium pellets used in vacuum evaporation technique for fabrication[3].

Figure 2.11: Stabilized selenium tablets with Arsenic doping and Chlorine used for fabrication of uniform a-Se films via vacuum evaporation technique[3].

For fabrication of flat-panel imagers, selenium is deposited onto a large area via vacuum evaporation, a physical vapour deposition technique[3]. Vacuum evaporation techniques mainly uses physical processes to produce reactant species into gas phase for film deposition[28], and are used for deposition of x-ray photoconductors where high uniformity

is required[37]. Vacuum evaporation requires a thermal evaporation chamber, where electric resistance heaters melt source material. In a typical vacuum evaporation chamber, the source material is positioned in the bottom, and wafers directly above. Figure 2.12 shows the vacuum evaporation technical used for fabrication of Se detectors.

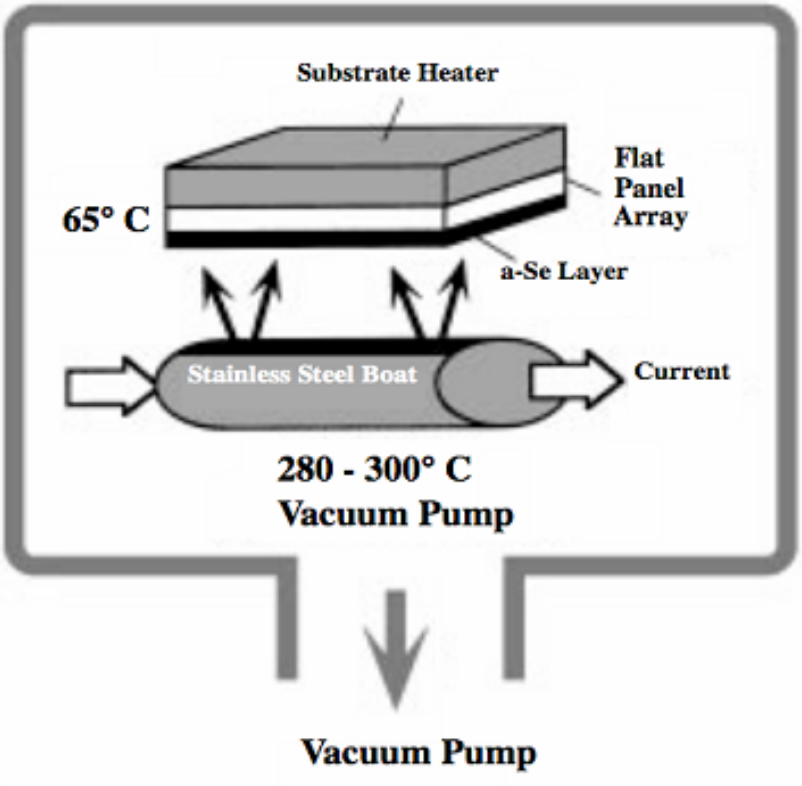

Figure 2.12: Vacuum evaporation process of uniform a-Se films[3]. The vacuum deposition chamber consist of a stainless steel boat and a substrate holder. The stabilized selenium tablets are heated in the stainless steel boat, and evaporated particles are deposited onto the substrate surface.

Pellets of stabilized selenium with arsenic and chlorine doping are placed in a steel boat heated to between 280 and 300 degrees Celsius by resistance heaters. Vacuum conditions (10_{-5} torr) allow the particles to evaporate and reach the target substrate without scattering (large man free path) and form thin layers on the wafer. The substrate wafer temperature is kept at 65 degrees to ensure constant growth rate and uniform films[36].

Stable a-Se is a good candidate for semiconductor-based, direct x-ray detection because

it has very low reported dark current at 0.01 nA/cm^2, and can be coated onto a large area, for example 40x40 cm^2 with uniform properties. Crystallization is avoided with arsenic and chlorine doping allows for improvement material stability and charge collection. The mobility-lifetime product of Se is in the order of 10^{-5} cm^2/V for holes, and 10^{-6} cm^2/V for electrons. Even though the mobility-lifetime product is relatively low compared to CdZnTe, but still much higher than that of PbO and HgI_2.

The x-ray sensitivity in a-Se is dependent on the detector thickness, applied electric field, and material properties such as carrier mobility and lifetime. As the electric field increases, the ionization energy required to generate a detectable electron-hole pair decreases thus increasing in the sensitivity. Increases in the carrier mobility or lifetime can also increase the sensitivity because the carriers are traveling faster towards the electrodes and have less probability of getting trapped. From the same spectral x-ray input, thicker detectors would have a higher attenuation coefficient, and thus more x-ray absorption and detected signal.

2.3.2 Cadmium Zinc Telluride

Cadmium Zinc Telluride (CdZnTe) has been used in gamma ray detectors[38]. The advantages of CdZnTe detectors include high atomic number, low band gap, excellent sensitivity and high electron/hole mobility-lifetimes. With a high Z_{eff} of 50, CdZnTe is not only used for x-ray detection, but also been reported for the use of higher energy gamma ray detectors[38]. Out of the materials reviewed, CdZnTe has the lowest band gap energy of 1.7 eV, and since carrier yield is an inverse function of E_{gap}, excellent sensitivity and maximum collectable charge are observed. The highest sensitivity of 24 μC/(cm^{2}R) is reported, more than two orders of magnitude higher than the sensitivity of a-Se[32].

Cadmium Zinc Telluride films can be grown via the Close-Space Sublimation (CSS) technique[5, 4, 6]. Figure 2.13 shows a CSS quartz chamber. The CdZn and CdTe powders are placed in the hollow carbon plate, and the substrate is supported on top of the source with a carbon spacer between 3 to 20 millimeters. Vacuum is maintained with a rotary pump.

The source and substrate temperatures can be controlled separately with halogen lamps. From Figure 2.14, the source and substrate temperatures are 650 and 500 °C respectively during the growth. The growth rate of the CSS technique is very high, between 5-10 μm/min, and film thickness of 50 to 300 μm can be easily deposited. Figure 2.15 plots the growth rate as a function of source and substrate temperatures.

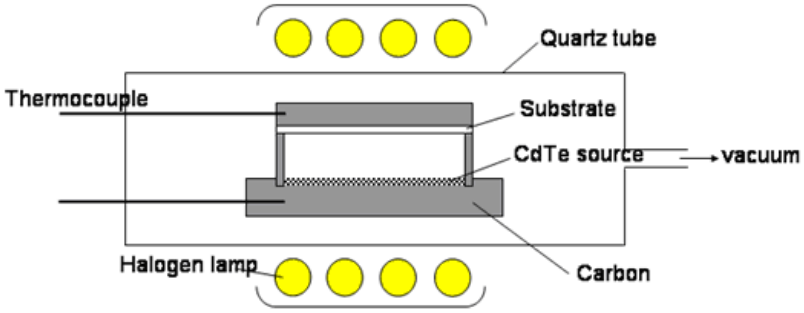

Figure 2.13: Close-Space Sublimation chamber[4].

From Figure 2.15(a), when substrate temperature is constant, and only varying the temperature of the source, the growth is observed to increase as the source temperature is raised. From Figure 2.15(b), with constant source temperature, the growth rate increases initially but a sharp decrease is observed. The sharp decrease occurs when the temperature difference between the source and substrate is below 100 degrees Celsius. Optimal growth rate is observed when this temperature difference is 150 degrees. Figure 2.16 shows SEM images of the deposited CdZnTe film with a range of different grain sizes and porosity.

The CdZnTe photoconductor are polycrystalline with average grain size of approximately 10 μm. For charge collection, minimum charge trapping and recombination is observed due to high electron and hole mobility-lifetimes. However, there two main disadvantages that plague CdZnTe for x-ray detection: high dark current and high substrate temperature during fabrication. From Table 2.2, even though the sensitivity of CdZnTe is high, two orders higher than that of a-Se, the dark current are also high, almost three orders higher. Thus the improvement in the final output signal detected is significantly reduced. The advantages are diminished due to high dark current. Lastly, for large area coating, high substrate temperature limits the detector size, and only relatively small CdZnTe x-ray detectors have bee reported in the literature.

2.3.3 Mercuric Iodide

Mercury Iodide (HgI_2) photoconductors have a very high atomic number and reported sensitivity. From Table 2.2, the effective atomic number for HgI_2 is 67, higher than that of CdZnTe, and HgI_2 detectors can absorb high percentage of the incident photons with relatively thinner photoconductor thicknesses. Excellent sensitivity have also been reported

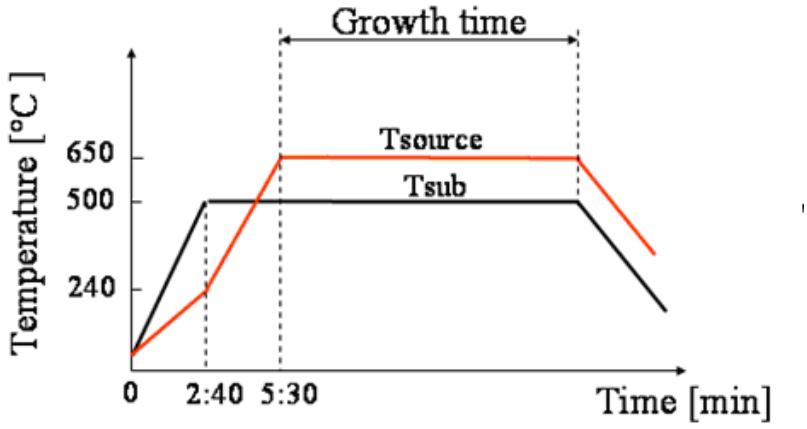

Figure 2.14: Source and substrate temperatures during Close-Space Sublimation[4].

at 10 μC/(cm^{2}R). However, the material stability and dark current dependence on temperature are major disadvantages for HgI_2[39, 40]. The HgI_2 dark current have a high dependence on temperature, and with a 15 degrees difference the dark current have almost a two order of magnitude difference from 0.02 to 18 nA/cm^2. Thus, good material stability with constant performance is desired. The following equations demonstrate the preparation of HgI_2:

$$[h]2Hg + I_2 \rightarrow Hg_2I_2 \ , Hg_2I_2 \rightarrow Hg + HgI_2 \ . \tag{2.6}$$

Mercuric iodide can be prepared with the basic reaction between metal mercury and iodine, where the product of this reaction is photosensitive and decomposes to mercury and HgI_2. HgI_2 powders can be used to fabricate x-ray detectors using wet Particle-In-Binder (PIB) and physical vapour deposition techniques. Figure 2.17 show examples of HgI_2 grown on various substrates[41] courtesy of DxRay Inc ($http://www.dxray.com/?page_id = 115$).

The HgI_2, similarly to PbO molecules can be mixed with acid precursor to be cured and form a uniform film via the wet PIB technique. For vacuum evaporation, the same powder can be heated to evaporate and deposit films on the large area TFT. Figure 2.18 shows the final direct x-ray detector produced by vacuum evaporation courtesy of DxRay Inc[42] ($http://www.interon.no/?page_id = 18$). This particular detector is the size of 10x10 cm^2, however the maximum detector of 20x25 cm^2 have been reported in the literature[43, 44].

The wet Particle-In-Binder (PIB) technique can be used to fabricate lower quality HgI_2 and PbO photoconductor films[45, 46, 39, 40], and is based on organic chemistry. A

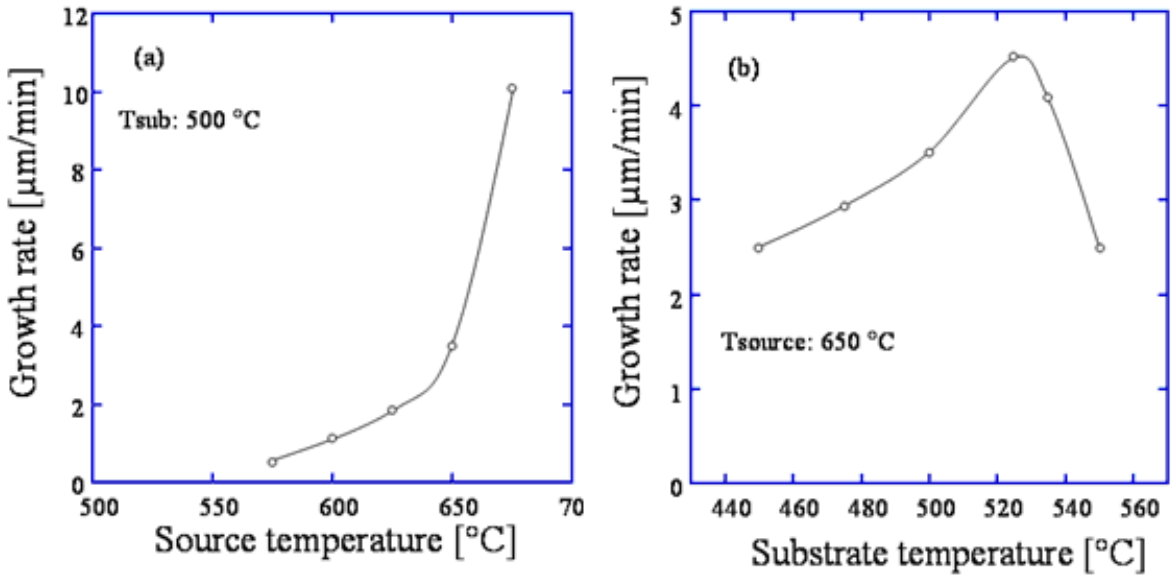

Figure 2.15: (a) Growth rate dependence on source temperature. As the source temperature increases, keeping the substrate temperature constant, the growth rate increases. (b) Growth rate dependence on substrate temperature. For a constant source temperature, there is an optimal substrate temperature to maximize the growth rate[5].

polyimide polymer chain contains an imide group and is used to bind photoactive molecules together into a film. Figure 2.19 shows an imide functional group consisting of two carbonyl groups bounded to oxygen and three free bonds for the photoactive molecules to attach to.

The General Electric (GE) Company holds a patent on the wet PIB technique, and Figure 2.20 illustrates the final detector structure[45]. From the bottom, the detector glass substrate has three metal pixel electrodes, each electrode containing a small capacitor for charge collection. Then a polyamic acid solution containing the photoactive materials can be coated on the thin-film-transistors (TFTs) using screen printing method. With heat, the precursor coating is cured and imidized, where the x-ray sensitive particles are bounded in the polyimide matrix. After the photoconductor film is printed, a passivation layer such as parylene can be deposited on top, followed by the top metal electrode.

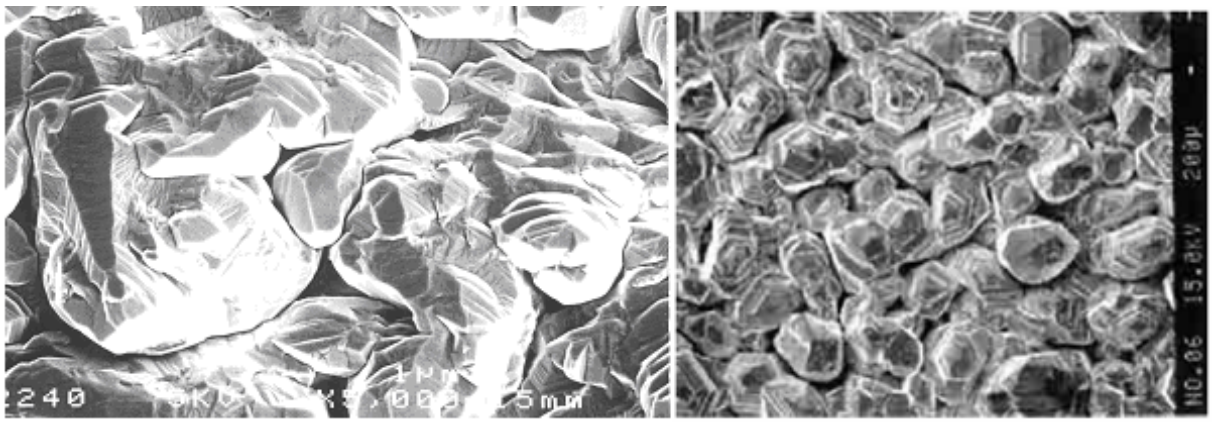

Figure 2.16: SEM images of CCS films with a range of grain sizes and porosity[6].

2.3.4 Lead Iodide

Lead Oxide (PbO) photoconductors are actively investigated by Simon *et al.* at a research group from Phillips in collaboration with Thunder Bay Research Center in Canada[7, 8]. The main advantage of PbO detectors is the high atomic number; it has the highest Z_{eff} from Table 2.2 at 74 and has much higher attenuation for high-energy x-ray photons such as for chest x-ray application. PbO detectors are relatively new and still under research, where the sensitivity data is not yet available. However, there are several limitations including high dark current and low mobility-lifetime product. The dark current is in the same order of magnitude as CdZnTe detectors, and reported to be as high as 5 nA/cm^2[7]. This high dark current effectively diminished the performance of the detector. The electron/hole mobility-lifetime product for PbO is the lowest, at 10^{-7} cm^2/V, almost three orders of magnitude lower than that of CdZnTe. Where significant charge trapping and recombination can be observed in the photoconductor film[8]. For possible improvements, the morphology and compatible blocking layers can be explored. Red lead (lead tetroxide) is prepared by heating yellow lead (lead monoxide) to above 500 degrees Celsius. The red lead particles can be mixed in the precursor acid used in the wet Particle-In-Binder, and printed on the TFT surface to form relatively thick and uniform films. Figure 2.21 shows the cross sectional view of PbO film fabricated by the wet PIB technique.

From Figure 2.21(a), small pores are observed in the cross-sectional view of the printed photoconductor film. Figure 2.21(b) zooms into one of the pores, and large voids are observed. For PbO, pores and voids up to 20% of the density have been reported[8]. The wet PIB method is a simple process with low cost, and sensitivity improvements are also

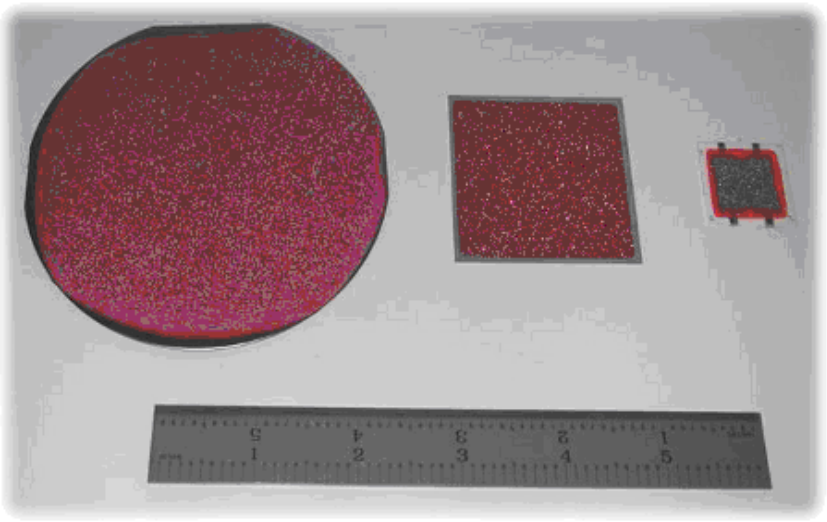

Figure 2.17: Example of polycrystalline mercuric iodide x-ray detector films grown on various substrates and sizes (courtesy of DxRay Inc.).

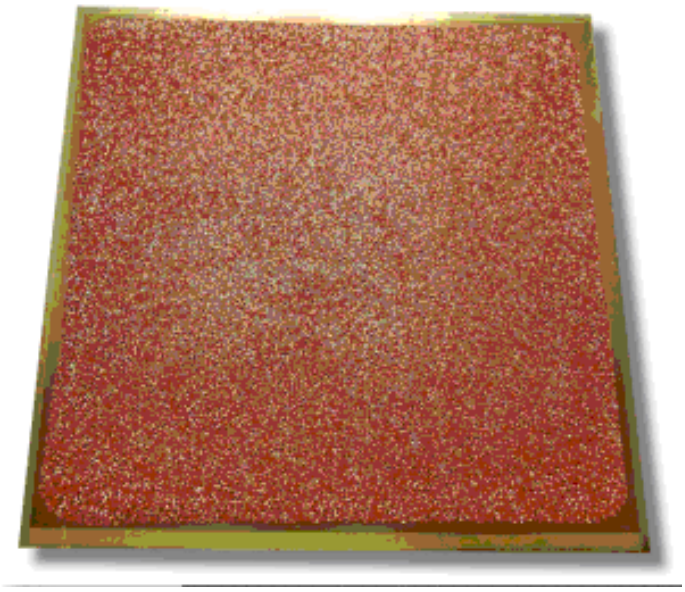

Figure 2.18: Direct conversion polycrystalline Mercuric Iodide detector coated onto a 10M pixel CMOS imaging array device (courtesy of DxRay Inc.).

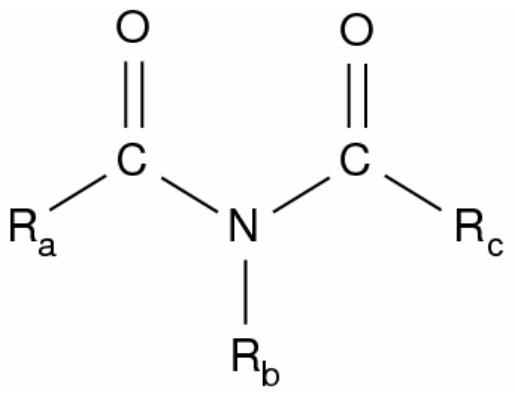

Figure 2.19: Imide organic functional group used in PIB technique for fabrication of photoconductor films.

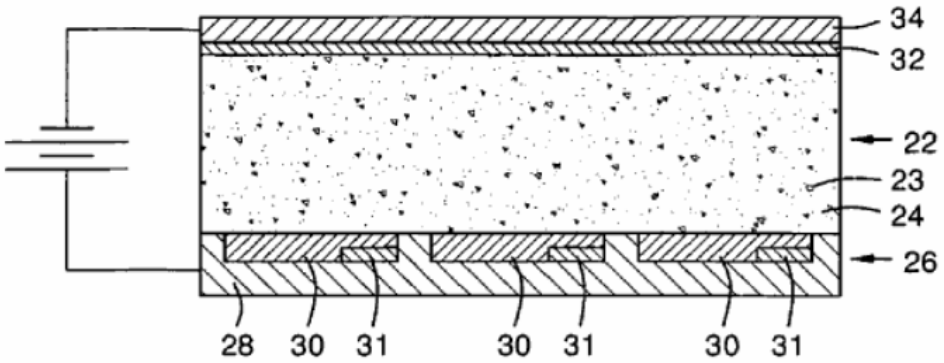

Figure 2.20: Wet Particle-In-Binder (PIB) method for fabrication of x-ray films.

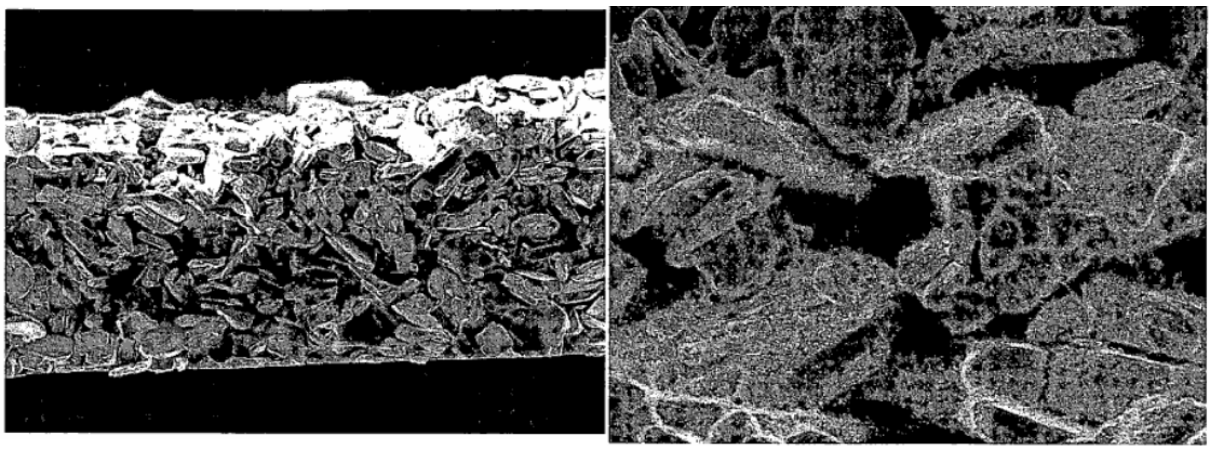

Figure 2.21: (a) SEM image of porosity in the PbO PIB photoconductor[7, 8]. (b) SEM image (zoomed-in) cross-sectional view.

reported due to the surface state passivation by the polyimide. However, some challenges include precise control of film thickness and high porosity.

Chapter 3

Methods

3.1 Modeling approaches

The complete signal formation process in semiconductor x-ray detectors from incident x rays to electric signal can be divided into four sub-processes: incident x-ray interactions, secondary electron interactions, electron-hole pair generation and charge transport illustrated in Figure 3.1[47].

Incident x-ray photons can interact in the semiconductor material through Rayleigh scattering, Compton scattering, photoelectric absorption, and characteristic x rays may be created during atomic relaxation. Photoelectric absorption and Compton scattering, can generate high energy electrons where the kinetic energy is deposited in the semiconductor via elastic and inelastic scattering events. In some cases, Bremsstrahlung or braking radiation can be produced during particle deceleration. Generation of electron-hole pairs require sampling algorithms for the number of carriers generated, and spatial distribution of electron-hole pairs through calculation of burst and thermalization distances. The charge transport model should include recombination and trapping effects. Photon-electron and electron-hole pair interactions can be simulated separately or coupled together in Monte Carlo models, and this section briefly describes some existing methods available for modeling direct x-ray imaging detectors.

3.1.1 Photon and secondary electron interactions

A number of available MC simulators exist for modeling radiation transport: ETRAN, ITS3, PENELOPE, and EGSnrc can be used for simulation of photon, electron, and

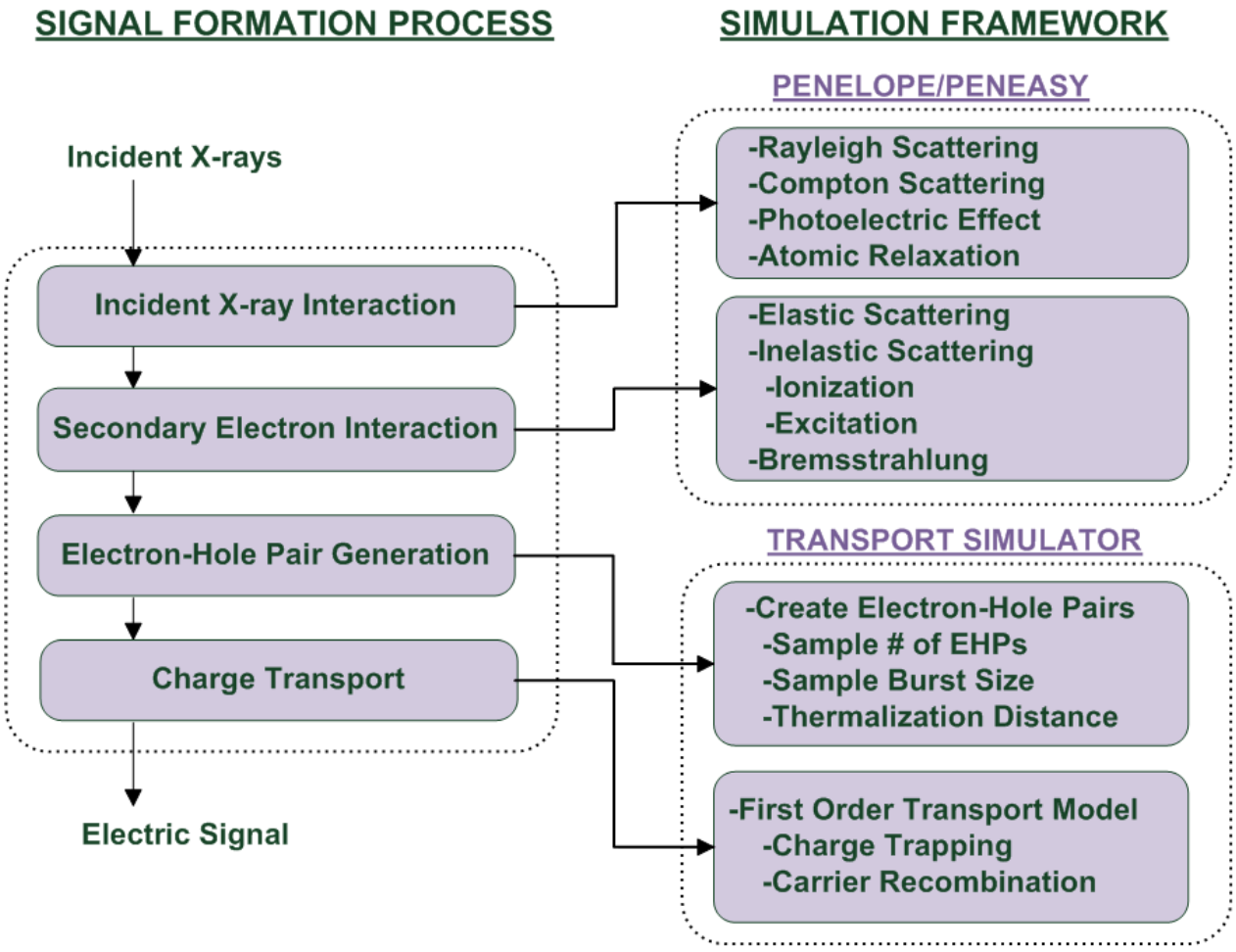

Figure 3.1: Block diagram of the signal formation process in semiconductor x-ray detectors including: incident x-ray interaction, secondary electron interaction, electron-hole pair generation and charge transport.

positrons[48, 49, 50, 51]. MCNP, GEANT4, and FLUKA can be used for additional simulation of heavy charged particles and neutrons[52, 53, 54]. The probability distributions for the different atomic interaction mechanisms are characterized by a corresponding differential cross-section (DCS), which can be used to determine various relevant quantities such as energy transfer and angular deflection. These interaction cross-section models implemented in the aforementioned MC codes have been already benchmarked with established databases and offer an accurate model for simulation of various mechanisms. Figure 3.2 and 3.3 show the photon and electron interaction cross-sections in selenium, generated with PENELOPE 2006[50].

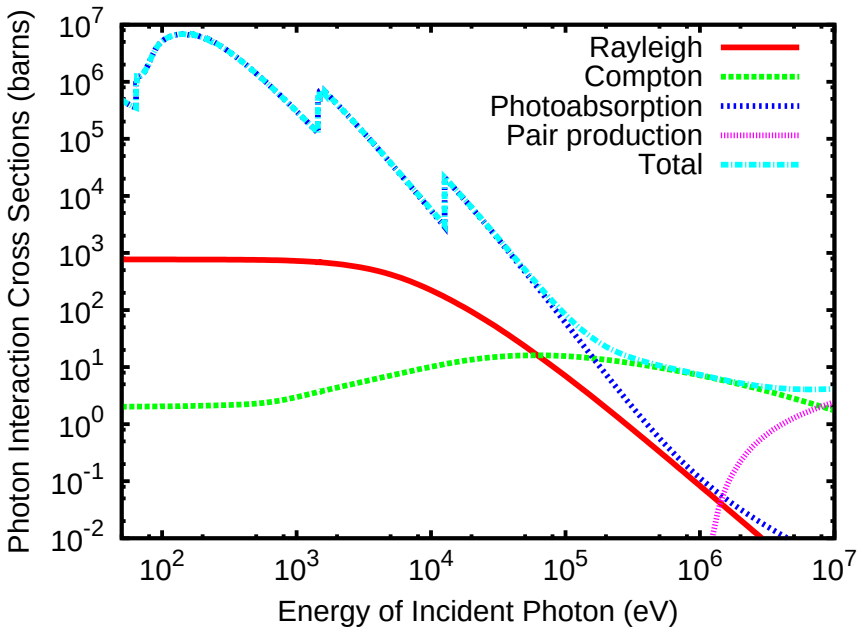

Figure 3.2: PENELOPE photon interaction cross-sections in selenium from 100 eV to 10 MeV.

The interactions are a function of particle energy and material properties. For the x-ray energy range of medical applications in a-Se, the main interaction mechanisms are: Rayleigh scattering, Compton scattering, and photoelectric absorption. Pair production may occur at higher photon energies, where positron emission decays create a pair of annihilation photons moving in approximately opposite directions. Pair production due to radiotracers injected in the body is the basis of a functional imaging technique called

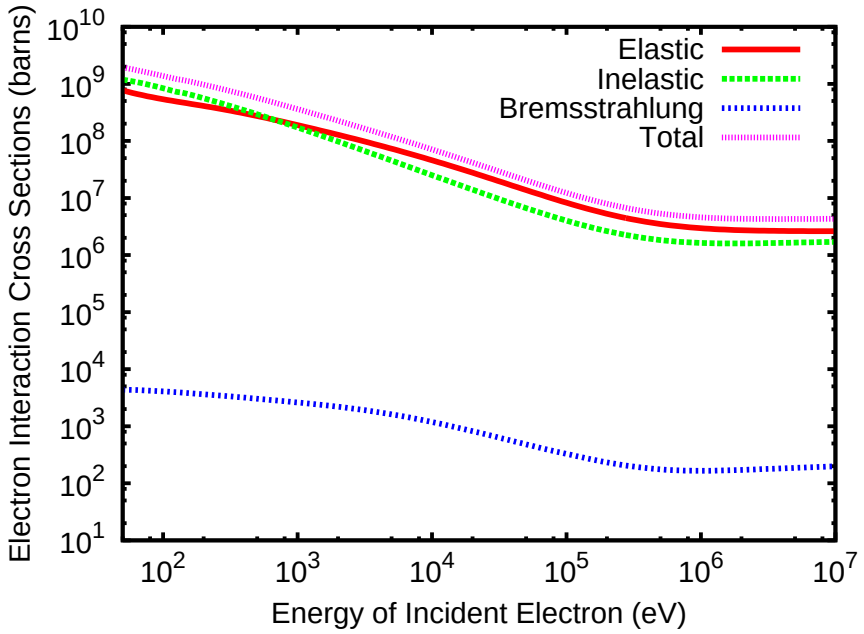

Figure 3.3: PENELOPE electron interaction cross-sections in selenium from 100 eV to 10 MeV.

positron emission tomography (PET). For electrons the main mechanisms are elastic scattering, inelastic scattering and Bremsstrahlung. The total interaction cross-section can be computed as the sum of the cross-sections for all possible interaction mechanisms, and is used to compute the mean free path required for sampling the location of the random scattering events in the material.

Existing MC models offer advanced geometric packages that allow for simulation of complex detector geometries and experimental setups. The interaction models and cross-Fsections have already been benchmarked and validated with established databases and offer an accurate model for simulation of various interactions. MC models require simulation of many histories in order to reach high accuracy and low variance. Some MC codes allow for different modes of simulation such as: condensed, detailed and mixed in PENELOPE. In the condensed mode, many soft interactions that do not change significantly the direction and energy of the particle are reproduced into a single interaction using multiple scattering theories to single condensed interaction to greatly reduce simulation time. In the case that details of locations and small energy changes are needed, a detailed simula-

tion mode can be used to track all interactions by the particle. Often, a mixed simulation mode can be used that optimize between simulation time and detail. Another advantage is that the energy and dose distribution profiles can be readily calculated using existing MC models[55, 56, 57]. One limitation of using most available MC simulators for modeling of semiconductor detectors is the lack of simulation library and models for generation and transport of electron-hole pairs.

3.1.2 Electron-hole pair transport

Several customized MC simulators have been developed that focus on modeling of electron-hole pair interactions[19, 58]. The effect of trapping and recombination of electron-hole pairs on sensitivity reduction and ghosting[19], leading to temporal artifacts in the x-ray image, and time-of-flight simulations of electron-hole pair to determine the density of state in a-Se[58] have been previously studied. Figure 3.4 shows the setup for time-of-flight simulations in an a-Se detector. A low-energy x-ray photon or high-energy laser is used as the source for excitation in the photoconductor. Many electron-hole pairs are created near the surface and carriers have to travel the detector length in order to be detected. A simplified one dimensional model is used for photon absorption and creation of electron-hole pairs, however significant flexibility is attained for implementation of carrier transport in the detector material without having to consider the interaction high-energy electrons.

Customized electron-hole pair simulators allow for focused studies of carrier transport in semiconductor x-ray detectors, and offer significant flexibility for the implementation of complex recombination and trapping models. Compared to detailed photon-electron simulations, exponential attenuation models for x-ray photons are used assuming completed absorption of incident energy for carrier generation and an one-dimensional model for electron-hole pair transport. This ignores the charge spreading due to high energy photoelectric and Compton electrons, the lateral spreading due to diffusion of electron-hole pairs, and noise in the detector response from Compton scattering and fluorescent x rays.

3.1.3 Coupled simulations

The coupled simulation method combines the simulation x-ray radiation with electron-hole pair transport, and utilize the advantages of the two previous methods. For example, energy deposition events in the semiconductor or scintillator material can be simulated with an available MC simulator, combined with a customized simulator for electron-hole pairs.

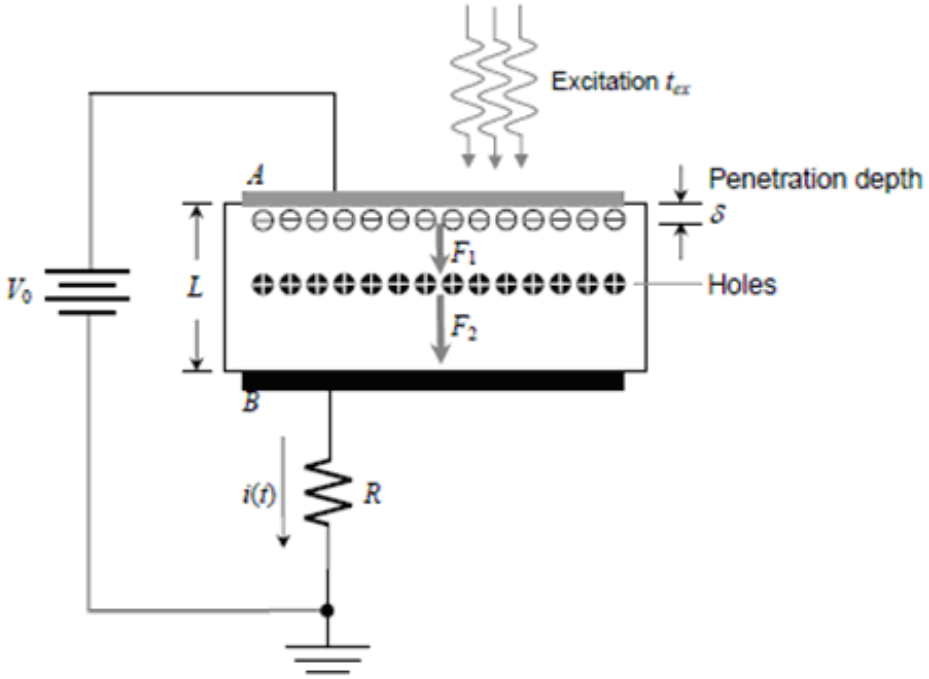

Figure 3.4: Setup for Time-of-flight simulation for a-Se detector.

Combined simulation can be used to simulate the complete signal formation process in x-ray detectors, by taking advantage of existing validated MC simulators for photon-electron interactions, and this framework can allow for significant customization of the EHP transport models. However, modifications are often required to efficiently interface the existing simulator with the transport code. A large number of simulation histories is required to achieve low variance for studies such as the point response function needed for the calculation of modulation transfer function and detective quantum efficiency (DQE). These limitations drive the need to further improve simulation efficiency, including parallelization implementations with computer clusters and utilization of graphic units for further speed-ups.

Moisan *et al.* at TRIUMF[59, 60] developed a Monte Carlo simulator for PET imaging utilizing a Gamma-Ray Interaction Tracking (GRIT) for high energy photons and DETECT routines for optical photon simulations. The GRIT program uses a simple gamma-ray model taking into account only photon interactions. The locations of interaction are saved as the input to the DETECT routine, and allow for only simple detector geometries. The DETECT routines are used for optical photon transport simulation allowing for real-

istic transport of optical photons in scintillator detectors. More sophisticated gamma and x-ray simulation can be achieved by replacing GRIT with more complex programs such as Geant4, EGSnrc or PENELOPE.

Blakesley *et al.* has done work in the area of modeling organic x-ray imagers utilizing EGSnrc[61]. The DOSxyznrc code was used to generate the photon absorption probability distribution function and the optical photon transport is modeled by DETECTII[62, 63, 64] routines. For simplicity, this model assumes the incident photons only interact and deposit energy in a single location of the detector.

Extensive work has been published by Badano *et al.* on MANTIS for modeling indirect x-ray detectors by interfacing PENELOPE with DETECTII routines[65]. The detector model includes a CsI:TI columnar screen and takes into account not only x-ray photon interactions but also high energy secondary electron interactions and spreading that may degrade detector performance. The generation of optical photons inside the scintillator material is coupled from energy deposition events caused by the incident x-ray photons. In addition, the optical model takes into account the gain variance due to conversion with a Poisson random variable, and supports a realistic columnar model for anisotropic blur of optical photons. Previous work has been published for accelerating Monte Carlo simulations using GPUs[66, 67, 68] and the disadvantage of long simulation time has been addressed with the development of hybridMANTIS for parallelization simulations utilizing GPU[69, 70], where PENELOPE simulations are ran in the CPU and the slow optical DETECTII transport is parallelized to achieve faster simulation speeds.

3.1.4 Analytical approximations

Analytical models can be used alone or in combination with MC methods for simulation of imaging detectors. For example, a semiconductor gamma ray detector was modeled analytically to show the effect of electrode size on performance with significant charge trapping[9]. With large electrodes, charge induced by both electrons and holes are of equal importance. But when the bottom electrode is segmented into an array of small elements, the contribution of one type carrier is reduced. For the case that the hole and electron mobilities are different, small pixel design can allow for unipolar detection that significantly reduce the contribution of slow carriers due to charge trapping. This is demonstrated in the pulse-height spectra shown in Figure 3.5, where a much sharper peak is observed along with reduction in the noisy tail in the measurement and simulated pulse-height distributions.

In this work, the electron-hole pairs generated are assumed to be only from photoelectric absorption. The classic electrostatic Green's function is used to calculate the output on

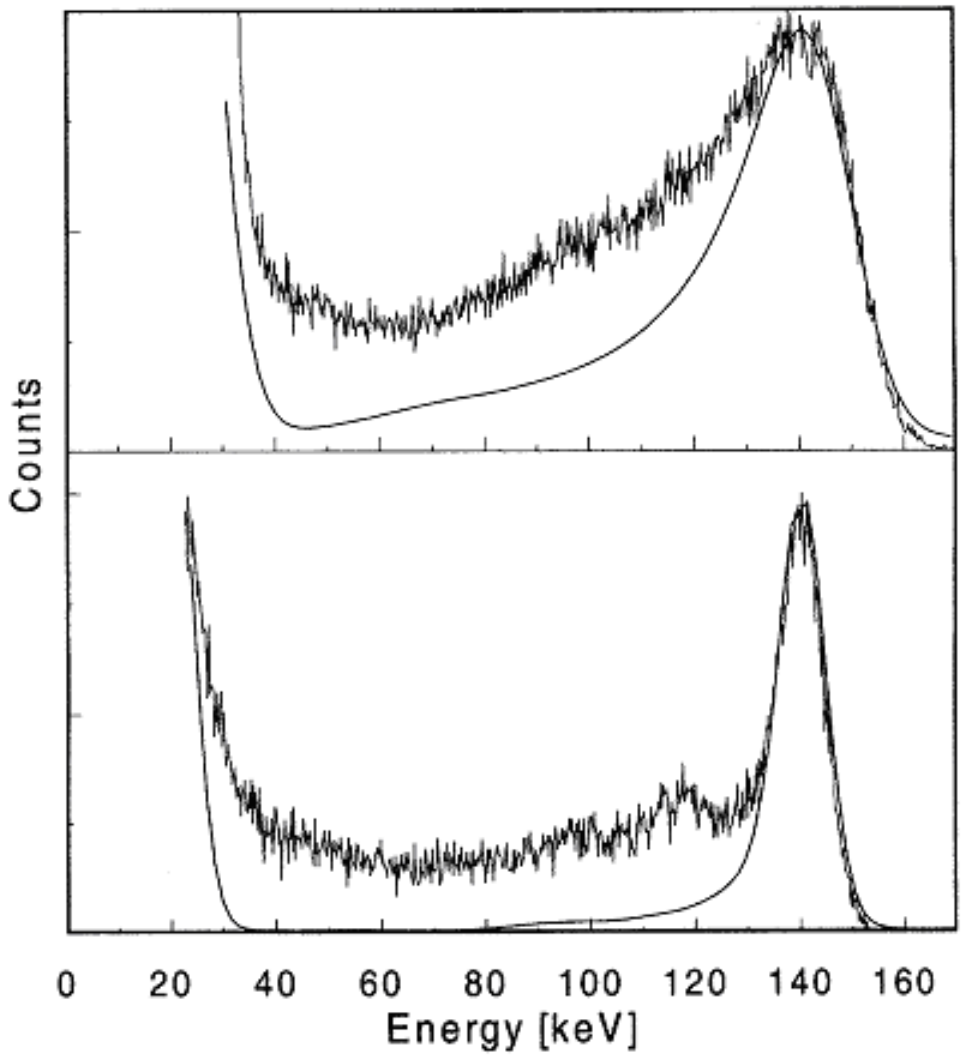

Figure 3.5: Theoretical and experimental pulse-height spectra for two different pixel sizes: 1.25 and 0.375 mm for top and bottom, respectively[9].

individual pixels based on carrier drift neglecting diffusion and recombination. Compared to MC methods, analytical methods do not require long simulation times and are efficient at solving problems with simple radiation fields that can be mathematically represented. However, analytical methods have limitations for modeling three-dimensional carrier transport, and have difficulties taking into account the stochastic events that affect radiation transport, such as trapping and recombination.

3.2 Pulse-height spectroscopy

Pulse-height spectroscopy is an experimental technique used in the quantitative study of a detector's response such as energy spectra to radiation sources. The pulse-height spectrum (PHS) is closely related to the Swank factor, an important performance metric of a x-ray detector.

3.2.1 Theory

The Swank factor[71, 72, 73], also known as the information factor, has been derived from the following expression relating the Detective Quantum Efficiency (DQE) at zero spatial frequency:

$$DQE(E) = \eta(E)I(E) \ , \tag{3.1}$$

where η is the quantum efficiency (or interaction efficiency) of the detector as a function of thickness and energy. The Swank factor, I, is a statistical factor that arises from the fluctuations in the number of electron-hole pairs detected per absorbed x-ray. The Swank factor is defined as:

$$I = \frac{M_1^2}{M_0 M_2} \ , \tag{3.2}$$

where M_n is the n^{th} moment of the detected electron-hole pair PHS distribution:

$$M_n = \sum_x p(x)x^n \ , \tag{3.3}$$

and the fluctuations in x (number of detected electron-hole pairs) are given by the probability distribution, $p(x)$. Alternatively, the definition of mean and standard deviation of the distribution can be used to estimate I,

$$m = \frac{M_1}{M_0} \ , \tag{3.4}$$

$$\sigma^2 = \frac{M_2}{M_0} - (\frac{M_1}{M_0})^2 \ , \tag{3.5}$$

$$I = \frac{m^2}{m^2 + \sigma^2} \ . \tag{3.6}$$

When the detector response is a single photo-peak, the Swank factor depends only on the mean and variance of the Gaussian distribution of the photo-peak:

$$I = \frac{m^2_{photo-peak}}{m^2_{photo-peak} + \sigma^2_{photo-peak}} \ . \tag{3.7}$$

However, this method for calculation of the Swank factor is accurate only for estimating a single-peak spectrum in the PHS, and cannot be used to model multiple spectral peaks in the PHS. Multiple spectral peaks are often observed in the PHS due to fluorescent x-rays escaping from the detector material and Compton scattering. Due to low spectral resolution and noise, the single Guassian fitting method is used in Blevis' experimental measurements[74, 75, 76]. For the simulation results presented in this work, Swank factors have been calculated considering the full PHS distribution and with a single Gaussian fitting method to provide a comparison with experimental results.

The Swank noise in semiconductor x-ray detectors arises from fluctuations in the number of electron-hole pairs detected per absorbed x ray and Figure 3.6 illustrate two sample PHS for two different incident photon energies, E_1 and E_2 in a-Se semiconductor-based x-ray detectors. Monoenergetic incident x-ray photons with energy, E_1 and E_2 ($E_1 < E_2$), are absorbed in the a-Se photoconductor creating many electron-hole pairs eventually detected at the opposing electrodes. For E_1, the detected PHS is a distribution with mean of m_{E1} and variance of σ_{E1}. Since E_2 has more energy than E_1, more energy deposition lead to an increase in the mean number of detected electron-hole pairs, m_{E2} with a variance of σ_{E2} in the detected PHS. The detected PHS shown here are of single peak, but multiple spectral peaks can be observed for cases of fluorescent ecape and Compton scattering illustrated in Figures 4.14 and 4.15. Swank noise is important because it can be used to study the lowest theoretical noise level achievable in the photoconductor material with an ideal x-ray source and signal readout system. Details of the signal formation process in semiconductor-based x-ray detectors are covered in detail in Section 4.1.1.

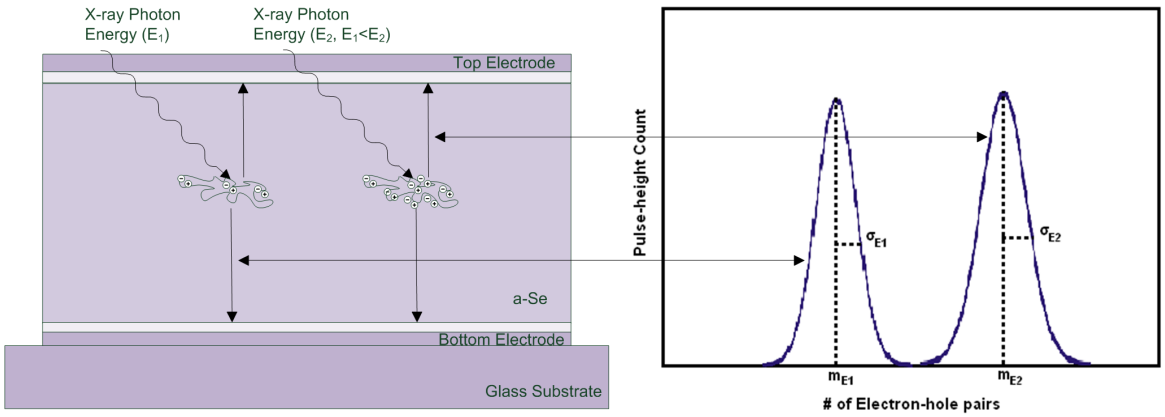

Figure 3.6: Illustration of two sample PHS for two incident photon energies (E_1 and E_2) in a-Se semiconductor-based x-ray detectors.

3.2.2 Experimental setup

When operating a radiation a detector in pulse mode, each individual pulse amplitude carry important information regarding the charge generated by that particular radiation interaction in the detector. Due to fluctuations in the inherent response of the detector, the pulse amplitudes are not all the same. If a large number of pulses are examined, a distribution can be measured and fitted to give the response of a detector. Figure 3.7 illustrate a setup for PHS measurements, which consist of a detector connected to a multi-channel analyzer (MCA) through pre-amplifier and amplifier circuitry. A high voltage source is used to bias the a-Se detector and improve sensitivity. Either an x-ray tube or radioisotope can be used as a source of photons.

Figure 3.8 shows the setup for pulse height spectroscopy measurements[74, 75, 76]. Figure 3.8(a) shows a pulse height spectroscopy setup at the Division of Imaging and Applied Mathematics (DIAM) laboratory. An x-ray tube and a Germanium (Canberra) detector[77] are mounted on an optical bench. The Germanium detector is purchased off-the-shelf, which includes the detector and pre-amplifier that are cooled with liquid nitrogen to reduce noise. Figure 3.8(b) shows the experimental setup, where an a-Se detector sample is interfaced with the system.

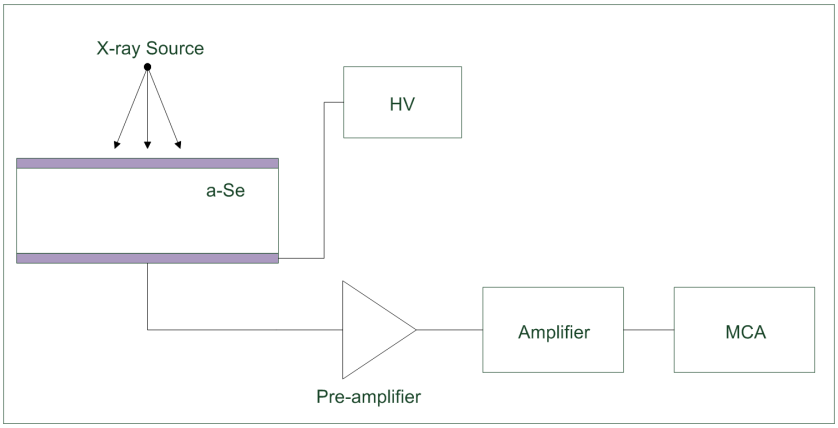

Figure 3.7: Experimental pulse height spectroscopy setup consisting of an a-Se detector biased with a HV source, connected to a MCA through pre-amplifier and amplifier circuits.

3.2.3 Isotope characterization

The emission spectrum of two radioisotopes is measured with the Germanium detector. Cobalt 57 (Co^{57}) and Cadmium 109 (Cd^{109}) are chosen for this experiment. Table 3.1 below shows the emission and half life data[78, 79, 80, 81, 82].

Table 3.1: Radioisotope emission data.

Isotope Name	Halflife (days)	Energy (keV)
Co^{57}	271.8	14.4, 122.1, 136.5
Cd^{109}	462.6	22.0, 22.2, 88.0

Figure 3.9 show the emission spectrum of Co^{57} and Cd^{109}. Distinct peaks at the emissions energies of Co^{57} at low energy range of 14.4 keV and high energy range of 122.1 and 136.5 keV are observed from the experimental measurement corresponding to the data shown in Table 3.1. Similarly, distinct peaks at emissions energies of approximately 22 and 88 keV for Cd^{109} are observed from the experimental measurement. These two radioisotopes are excellent gamma ray sources, but both have very high energies, much greater than the mammography range with an approximate mean energy of 20 keV.

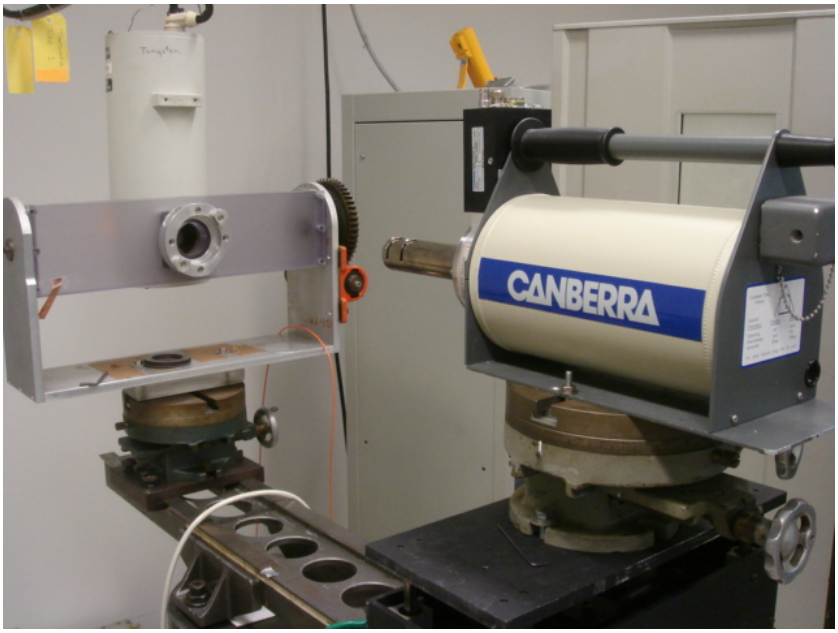

(a)

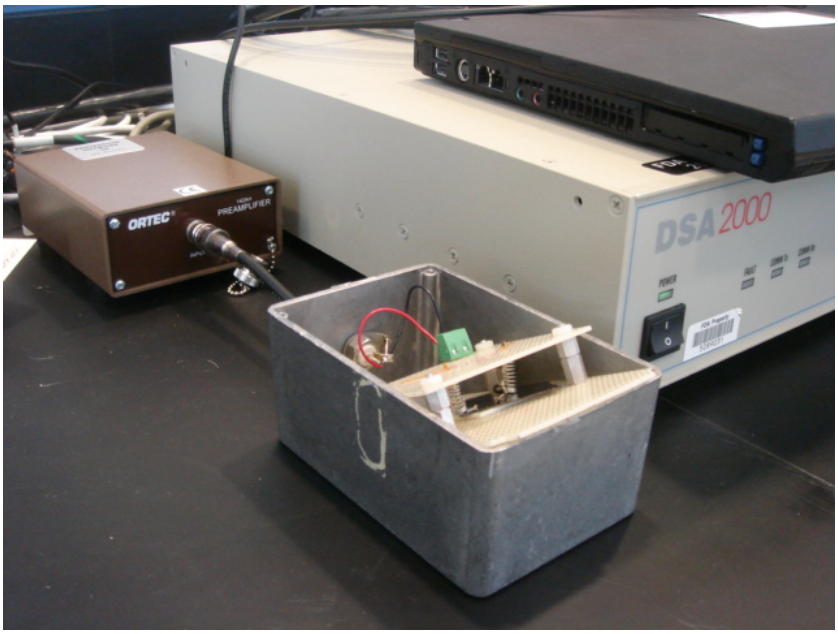

(b)

Figure 3.8: (a) X-ray tube with Germanium detector. (b) Detector holder interfaced with pre-amplifier and pulse height spectroscopy system.

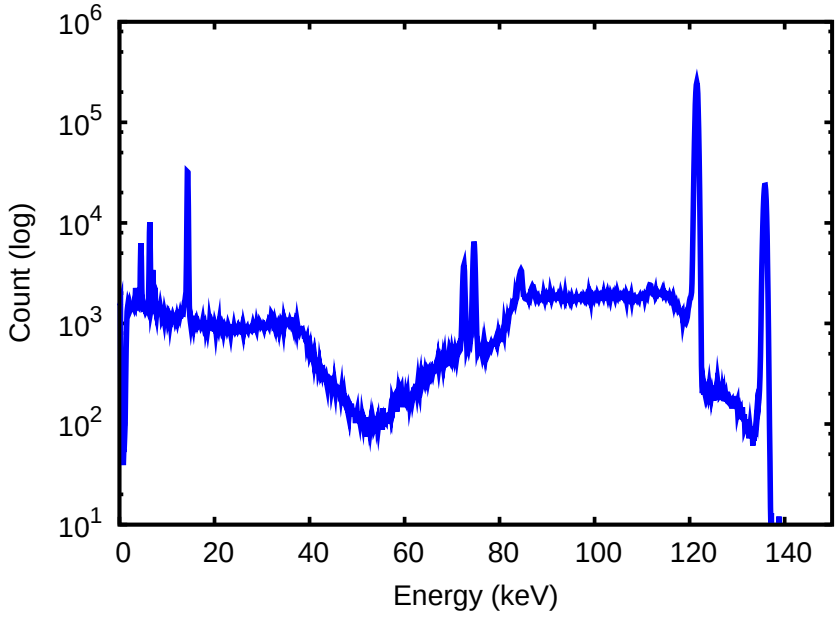

(a)

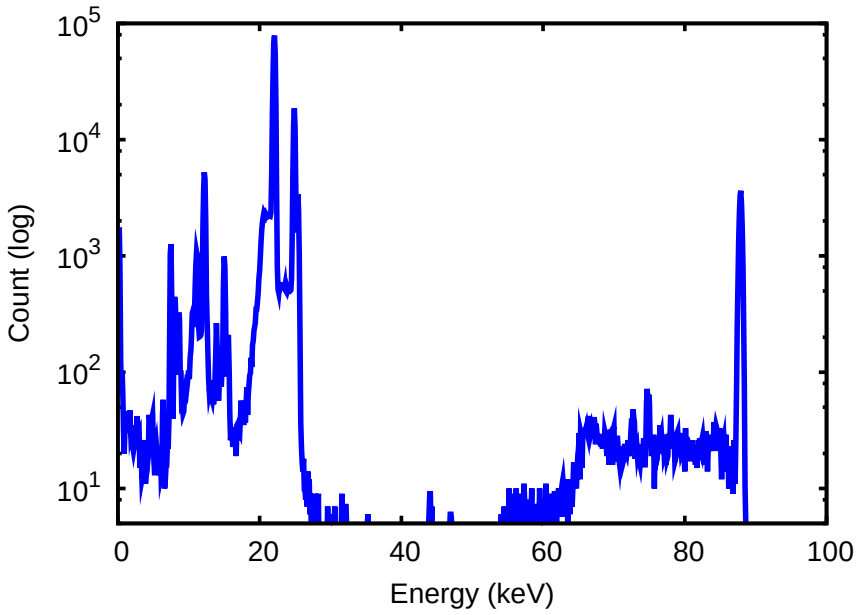

(b)

Figure 3.9: (a) Measured emission spectrum of Co^{57}. (b) Measured emission spectrum of Cd^{109}.

3.2.4 X-ray spectra optimization

The use of an x-ray tube with filters is examined to achieve a relatively mono-energetic x-ray beam at the mammography range. An x-ray tube with filters can be used to achieve a narrow spectrum beam, and used in pulse height measurements. A typical x-ray tube spectrum is very wide and is produced due to Bremsstralung radiation and characteristic x-rays. Figure 2.2 in Section 2.1.1 shows a calculated x-ray spectrum with a tungsten anode at 32 kVp. This wide spectrum beam can be filtered with materials with various thicknesses and characteristic x-ray energies, to produce a much narrow beam. Two palladium filters with thicknesses of 0.25 and 0.50 mm were made for the following measurements. Palladium K-edge energies are at 24.3 keV. Figure 3.10 shows the comparison of calculated[83] and measured tungsten x-ray spectrum, with the following conditions: 0.25 mm Pd filter, at 32.0 kVp tube voltage, 0.8 mA current, for 357.16 seconds, at 900 micron aperture size. The normalized calculated and measured x-ray spectrum shows very good agreement, except a secondary peak in the measured spectrum due to the characteristic x-ray escape. Characteristic x-ray escape occur when the incident x-ray energy is above the material K-edge, with enough energy to create fluorescent characteristic x rays which can be reabsorbed or escape the material. The secondary peak in measurements are from the escape of these characteristic x rays. In the calculated model, the detector is ideal and all characteristic x rays are reabsorbed.

The spectrum can be further narrowed with a thicker filter. Figure 3.11 shows the comparison of calculated and measured tungsten x-ray spectrum with a 0.5 mm Pd filter and 2 mm aperture. The measurement time was 358.46 seconds, and a narrower spectrum is observed. There is an eventual trade-off between narrow spectrum and count rate (photon fluence), where the number of incident photons becomes so small that experimental measurements are impossible.

3.2.5 Experimental challenges

Experimental pulse-height spectroscopy measurements are challenging due to several reasons. Compared to signal measurements over a long period of exposure usually in seconds for x-ray imaging, pulse-height spectroscopy is in essence capturing the response of each individual x rays through photon-counting in micro-seconds. The difficulties arise from the signal level for each individual photon being much lower compared to the case of integrating the signal over a long period of exposure, and the arrival of x rays impinging on the detector being a stochastic process. These problems can be solved in terms of carefully

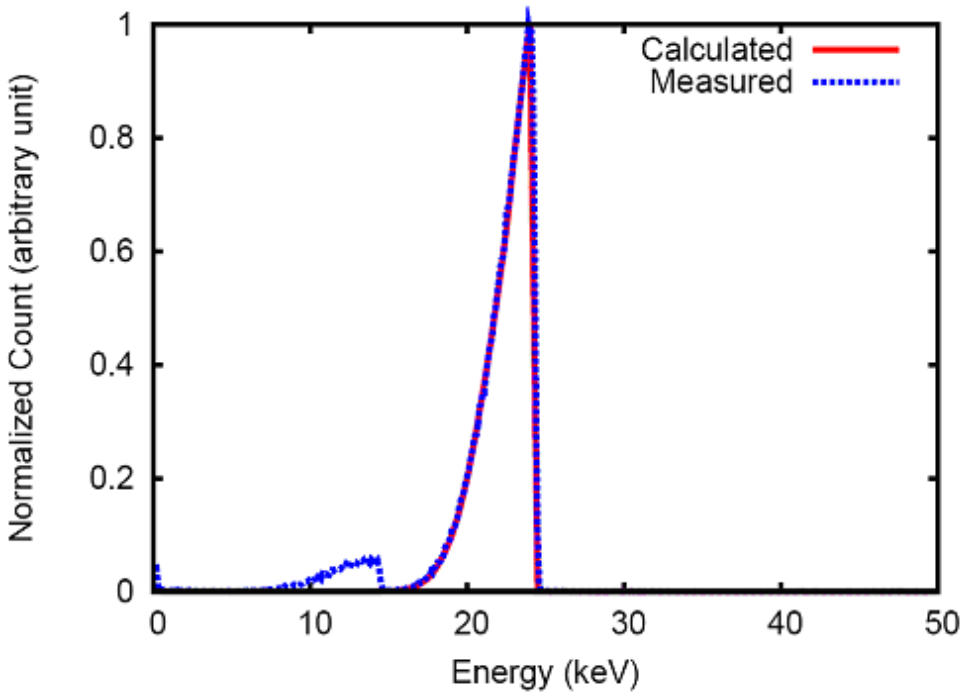

Figure 3.10: Comparison of calculated and measured x-ray spectrum of tungsten anode with 32.0 kVp, 0.25 mm of Pd filter.

selecting the x-ray input used, appropriate detector design to prevent leakage and noise reduction in the experiment.

Mono-energetic x-ray inputs are preferred for PH spectroscopy because the detector performance such as the Swank factor at the individual x-ray energy can be isolated and analyzed. Radioisotopes with distinct gamma-ray emission energies can be used. However, the photon flux levels for radioisotopes are often low compared to conventional x-ray tubes leading to prolonged measurement time, and most radioisotopes have several emission energies introducing additional sources of noise in the measurement. Alternatively, an x-ray tube with relatively much higher x-ray output can be combined with filter materials with specific characteristic x-ray energies for the generation of a quasi-mono-energetic spectrum. This method is limited by the x-ray anode material, maximum kVp of the x-ray tube and range of filter materials available. In addition, depending on availability, a synchrotron source may be the most ideal for mono-energetic photon and high photon fluence.

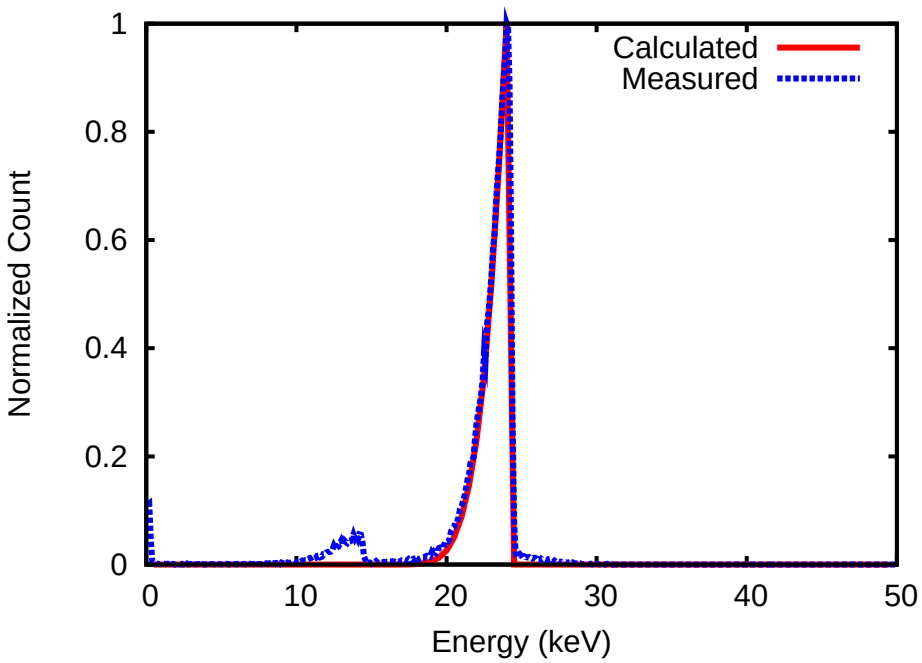

Figure 3.11: Comparison of calculated and measured x-ray spectrum of tungsten anode with 32.0 kVp, 0.50 mm of Pd filter.

The detector sensitivity to x-rays plays a major role in PH spectroscopy. In Table 2.2, the reported sensitivity for a-Se is two orders of magnitude lower than that of the CdZnTe. This means that the signal levels for a single incident photon is more than 100 times lower and pose a challenge for the detection. For a commercial off-the-shelf, charge-sensitive amplifier (Amptek 250CF), the output level for a 150 keV x-ray photon at 10 V/μm is in the range of approximately 1 mV, the same level as the noise floor and very difficult to detect. Since the sensitivity is a function of the applied electric field, an increase in the applied bias can improve the signal level at a cost of noise injection from the high-voltage source and the risk of possible breakdown of the photoconductor. Design improvements of a charge sensitive amplifier for detection of low signal output of a-Se detector can be a potential solution to this problem.

When using a radionuclide with relatively high gamma-ray energies above 100 keV, the detector thickness plays a significant role. For a Co^{57} source, and a 60 μm detector, the absorption probability or quantum efficiency of an incident photon is less than one percent. The quantum efficiency is a function of thickness, and with a thicker detector, more x-ray

photons are absorbed, leading to shorter measurement time and lower noise. In addition, a Faraday enclosure can be used to block out electromagnetic noise, and detector cooling with liquid nitrogen (similar to that of HPGe detectors) can be explored to improve the detector noise characteristics.

Chapter 4

Spatiotemporal Monte Carlo transport

4.1 Theory

The complete signal formation process in direct x-ray imaging detectors from incident x rays to electrical signals can be modeled by four sub-processes: incident photon interactions, secondary electron interactions, electron-hole pair generation, and charge transport. Figure 4.1 shows the block diagram for the signal formation process.

4.1.1 Charge generation for optical photons

For optical photon detection, only one pair of an electron-hole pair is generated and loses their initial kinetic energy in a thermalization process, after which the pair is separated by a finite distance r_0. This distance can be estimated using the Knight-Davis equation[84] given hv is the energy of the incident photon, E_{gap} is the material band gap, E_{app} is the applied electric field, D is the diffusion constant, ε is the dielectric constant and e is the elementary charge:

$$\frac{r_0^2}{D} = \frac{(hv - E_{gap}) + \frac{e^2}{4\pi\varepsilon r_0} + eE_{app}r_0}{hv_p^2} \ . \tag{4.1}$$

Figure 4.2 shows the thermalization distance as a function of ionization energy, in this case calculated from the difference of the incident photon energy and band gap. Since

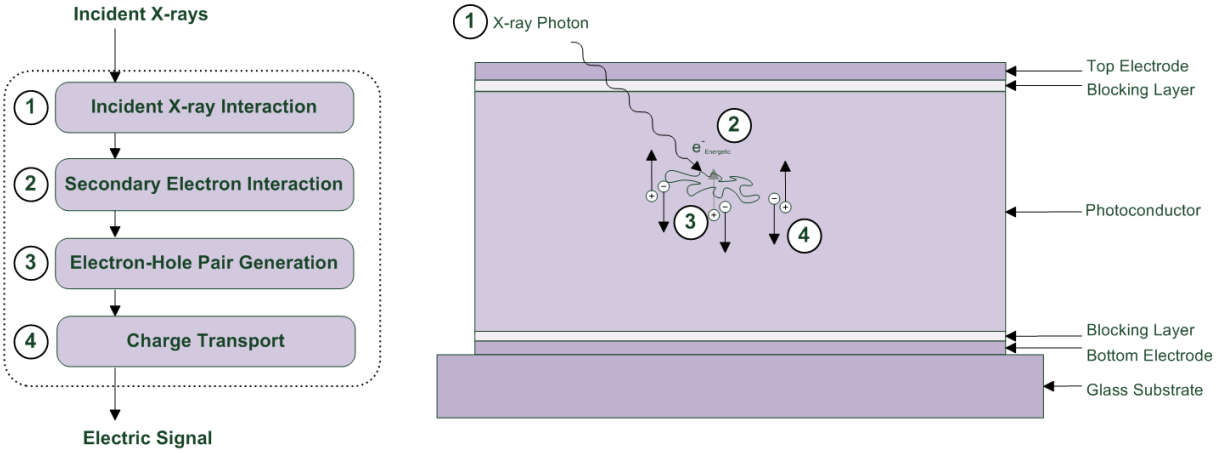

Figure 4.1: The signal formation model in direct x-ray detectors. The model consists of four sub-processes: incident x-ray interaction, secondary electron interaction, electron-hole pair generation and charge transport. The four sub-processes are illustrated graphically side by side in the layered detector structure. The detector is deposited on a glass substrate enclosed by blocking layers to reduce leakage and dark current. With an applied bias, the electron-hole pairs are collected at the opposing electrodes.

the band gap for a material is constant, when the incident photon energy increases, the ionization energy will also increase. This extra energy contributes to the separation of the electron-hole pair due to diffusion and electric field.

4.1.2 Charge generation for x-ray photons

Compared to optical detectors, the charge generation model in radiation detectors is more complicated due to creation of many electron-hole pairs. The dominant photon interaction mechanism in the energy range of interest is photoelectric absorption, which creates a secondary photoelectron with most of the energy of the initial x ray and capable of ionizing the material and producing many electron-hole pairs in the detector. It is important to note that a small fraction of photons that are Compton scattered can also produce energetic electrons capable of depositing energy, however the amount of kinetic energy is much lower compared to the photoelectron. As the high-energy electron travels through the detector material, it gradually loses energy through inelastic scattering and the energy lost, E_d, is deposited in the semiconductor material leading to creation of many electron-hole pairs in its path. The mean number of electron-hole pair generated, $\overline{N}_{EHP}$, can be estimated with

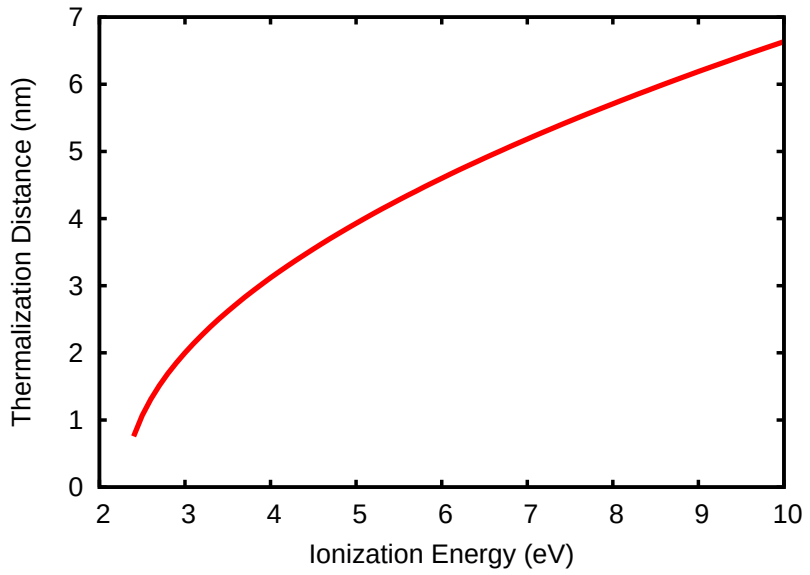

Figure 4.2: Thermalization (separation) distance as a function of ionization energy for each electron-hole pair. As the initial energy given to each EHP increases, the thermalization distance also increases.

a Poisson random variable from the energy deposited and the material ionization energy, W_0:

$$\overline{N}_{EHP} = E_d/W_0 \ , \tag{4.2}$$

where the concept of W_0 for semiconductors was originally developed by Klein[85]:

$$W_0 \approx K * E_{gap} + rhv_p \ , \tag{4.3}$$

where hv_p is the material phonon energy, and r is a uniform random number between 0 and 1, representing the ionization and photon emission components. The constant K is found to be 2.8 for crystalline materials in the semi-empirical formula and to be 2.2 for amorphous materials[86]. Figure 4.3 shows the correlation between the ionization energy and band gap, the solid and dashed lines represent K as 2.8 and 2.2, respectively. According to Que

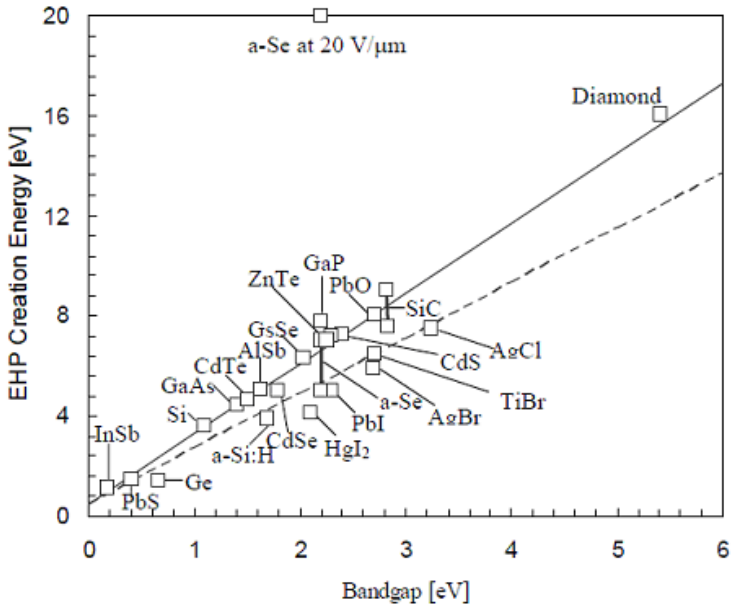

Figure 4.3: Ionization energy versus band gap energy for various materials.

and Rowlands[86, 87], the reduction in K is due to the inherent disordered structure in polycrystalline and amorphous materials[88].

4.1.3 Burst

Several models have been developed to simulate carrier generation in silicon, where all the electron-hole pairs generated in a sphere following either Gaussian or uniform distribution[89, 90, 91]. The use of Monte Carlo simulations of large number of electron track sizes have been also proposed to estimate the center of gravity and distributing a proportion of the photon energy into a bubble and a line portion uniformly[92]. In silicon, W_0 is not field dependent and the dominant effect of charge sharing is diffusion of carriers. However in a-Se, carrier drift also plays a major role due to the field dependence of carrier generation and transport. Hence for modeling carrier generation in a-Se, we introduce the concept of electron-hole pair bursts. A burst is defined as the cloud (spatiotemporal distribution) of electrons and holes generated after a local deposition of energy[10]. Energy transferred by inelastic electron collisions with outer-shell electrons can lead to excitation of plasma waves and create multiple electron-hole pairs[21]. These pairs constitute a burst, and the burst size is dependent on the energy of the incident particle and the material plasma frequency.

According to the Bohr adiabatic criterion[93], the burst size, r_{burst}, can be approximated using the following expression:

$$r_{burst} \approx \frac{v}{\omega_{pe}} \ , \tag{4.4}$$

where v is the velocity of the incident particle, and ω_{pe} is a material parameter known as the plasma frequency. The plasma frequency is dependent on the electron density in the material. The plasma frequency can be calculated with the following equation:

$$\omega_{pe} = \sqrt{\frac{n_e e^2}{m_e \varepsilon_0}} \ , \tag{4.5}$$

where n_e is the electron density in cm^{-3}, and m_e is the electron mass. Figure 4.4 shows the dependence of burst size on the electron kinetic energy. The concept of a burst is introduced in conjunction to the thermalization of carriers, in order to provide a three-dimensional distribution model for electron-hole pair creation.

4.1.4 Recombination

According to Rowlands and Kasap, there are two processes that exist for recombination of carriers in a-Se: geminate and columnar recombination[86, 88]. Geminate recombination based on the Onsager models assumes carriers can only recombine with their original geminate pair. While the columnar model argues that the high energy electron produces electron-hole pairs continuously in a column surrounding its track, and carriers recombine in this columnar fashion. Our model takes into account both arguments, by considering both geminate and columnar recombination in bursts. Where recombination can occur between any electron and hole traveling towards each other, and trapping can occur when an electron or hole reaches a lower energy state due to material impurities. The drift component takes into account both the applied electric field, E_{app}, and the Coulomb field due to other charge carriers. For the i^{th} charge carrier, the resulting electric field acting on it is given by:

$$\vec{E}_i = \vec{E}_{app} + \sum_{j \neq i} \frac{1}{4\pi\varepsilon} \frac{q_j}{r_{ij}^2} \hat{r}_{ij} \ , \tag{4.6}$$

where r_{ij} is the separation distance between charge carrier i and j, and $\hat{r}_{ij}$ is the field direction vector. In turn, the displacements in the three-dimensional x, y and z directions due to drift can be found:

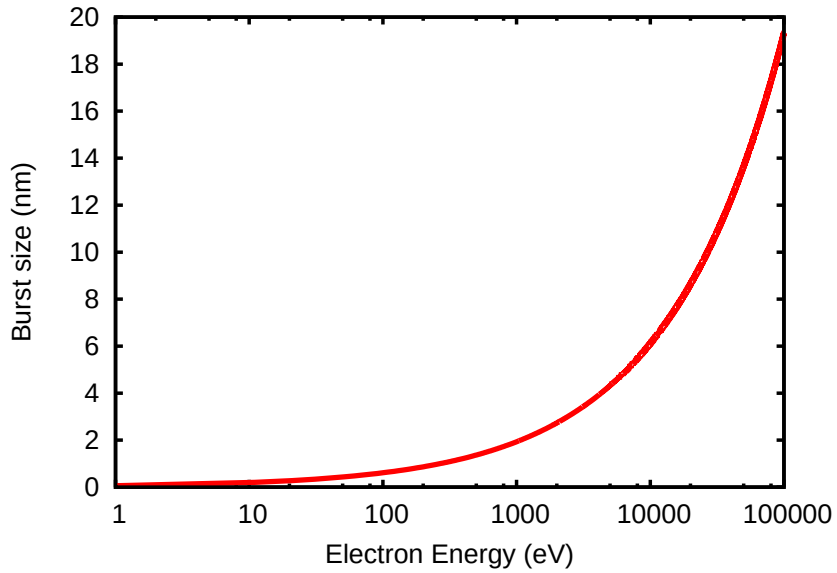

Figure 4.4: Burst size as a function of electron kinetic energy. Burst size decreases as the electron kinetic energy and velocity decreases.

$$\Delta x_{dr} = \mu_i E_{x,i} \Delta t \ , \tag{4.7}$$

where μ is the carrier mobility, E_x is the x component of the electric field, and Δt is the simulation time step. The components of the y and z directions can be found similarly. To find the diffusion components, the polar and azimuth angles are sampled from a uniform distribution, where the diffusion distance is given by $\sqrt{6D\Delta t}$ [94]. The total displacement in each direction is a sum of the drift and diffusion components:

$$\Delta x = \Delta x_{dr} + \Delta x_{dif} \ . \tag{4.8}$$

During transport, both drift and diffusion of carriers are calculated at each time step, where the drift component depends on the carrier mobility, electric field acting on the carrier and the simulation time step, and the diffusion component depends on the diffusion coefficient and the time step. As the carrier mobility increase/decrease, a carrier would

travel faster/slower in the semiconductor material (with increase and decrease in the drift and diffusion components).

4.1.5 Trapping

Many trapping effects have been modeled previously in one-dimension (z-direction) for a-Se detectors[19]. These include deep trapping, shallow trapping, trap releasing, trap filling and trap center generation due to incident x rays. Deep and shallow trapping differs in the trapping time of carriers. Deep traps have long trapping times on the order of seconds to minutes, while shallow traps may release carriers in fractions of a microsecond or less. For simulation purposes, when a carrier is trapped in a deep trap, it is considered lost. However, when a carrier is trapped in a shallow trap, the release of this trapped carrier (perhaps in subsequent exposures) can contribute to the detected signal as well. As electron-hole pairs start to move in the material and get trapped, the number of available traps decreases as a function of time, x-ray exposure and carrier concentration. At the same time, a competing process of trap center creation is occurring due to x-ray bombardment of the semiconductor material.

The current implementation of trapping uses a simple model that only considers deep trapping. The probability of trapping, P_t, can be calculated as [19]:

$$P_t = 1 - e^{-\frac{\Delta t}{\tau_t}} \ , \tag{4.9}$$

where τ_t is the trapping time. Constant trapping times are used for electrons and holes, to give an estimate of the average carrier lifetime and the effect of the applied electric field on carrier trapping probabilities in the semiconductor material. Figure 4.5 is the percent collected carriers for two trapping conditions. At low trapping conditions, more than 95% of electron-hole pairs are collected. At high trapping conditions, 80% of the electron-hole pairs are collected.

Constant trapping times are used for electrons and holes, to give an estimate of the average carrier lifetime and the effect of applied electric field on carrier trapping probabilities in the semiconductor material. The probability of trapping is a function of time, and the applied electric field affects the total carrier transit time from the interaction site to the appropriate electrode. The same trapping model implementation could be used to study different trapping mechanisms with the simulation framework.

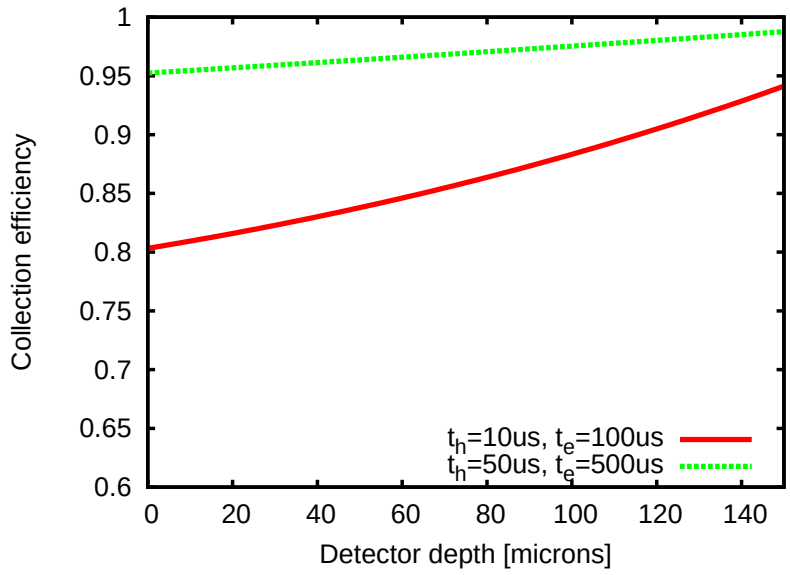

Figure 4.5: Collection efficiency for electron-hole pairs in 150 μm detector with deep trapping. The carrier lifetimes for holes t_h and electrons t_e are 10 μs and 100 μs, respectively for the high trapping case, and 50 μs and 500 μs for the low trapping case.

4.2 Implementations

4.2.1 Simulation model

A Monte Carlo transport code, ARTEMIS (pArticle transport, Recombination, and Trapping in sEMiconductor Imaging Simulation) was developed for the purpose of simulation of the signal formation process in direct x-ray detectors[95]. Various functions are implemented to model the physics outlined in the subsequent sections. The flow diagram for the implemented simulation framework is shown in Figure 4.6.

ARTEMIS consists of PENELOPE for x-ray and high-energy electron simulations, and a modular code for electron-hole pair creation and transport. For generation of electron-hole pairs, the locations of energy deposition by the high-energy electron are used as the site of initialization. The number of electron-hole pairs generated is calculated as a Poisson random variable using Equation 4.2 as a function of energy deposition and ionization

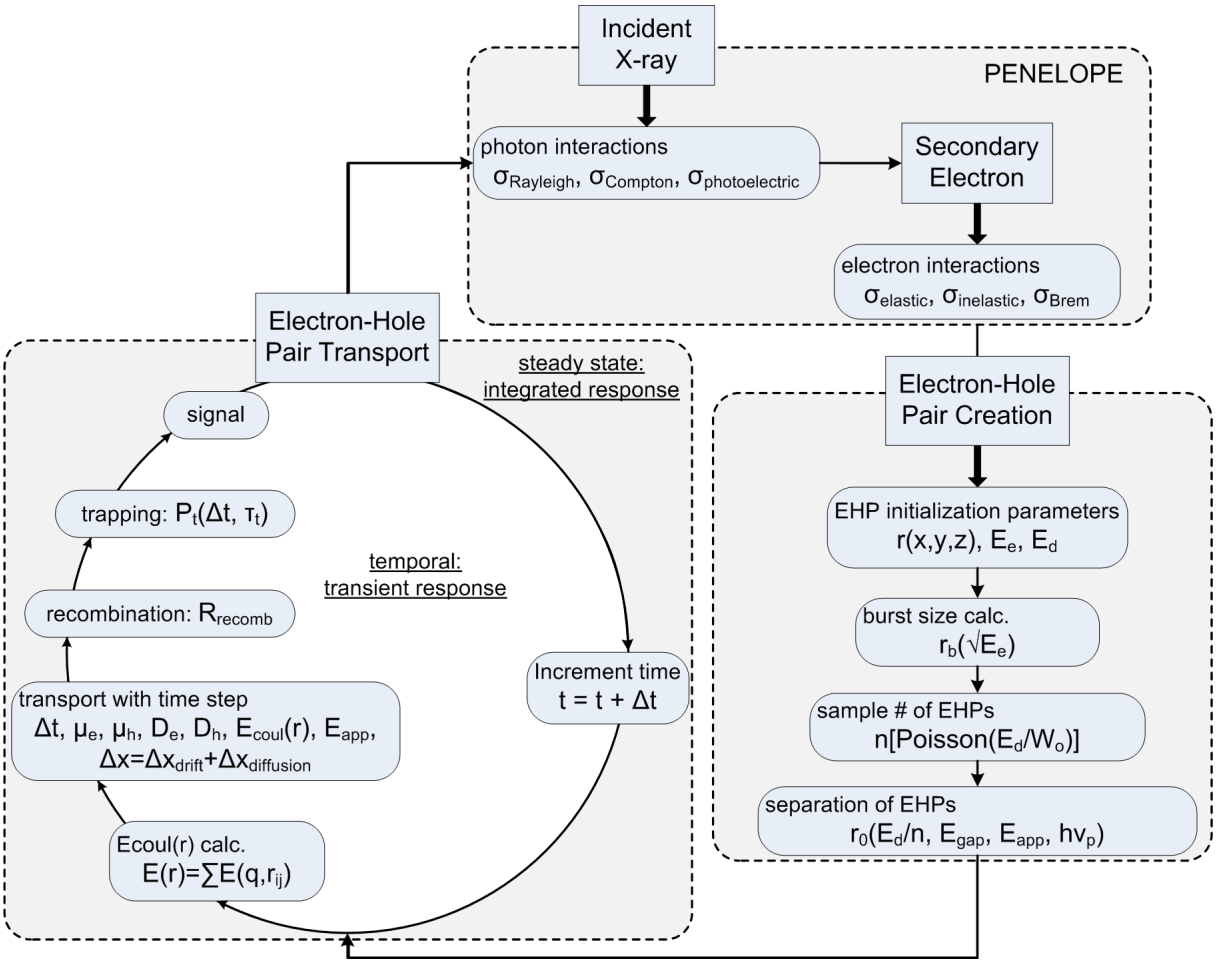

Figure 4.6: Flow chart for the simulation of the signal formation process in semiconductor x-ray detectors. Simulation of photon and secondary electron with PENELOPE is coupled with novel transport code for detailed spatiotemporal simulation of electron-hole pairs.

energy (Equation 4.3). In this work, the energy deposited is divided equally among the electron-hole pairs generated, and the thermalization separation distance between the pair is obtained using Equation 4.1. The burst radius is calculated as a function of the high-energy electron velocity, and in conjunction with the thermalization distance, generating a distribution of electron-hole pair locations with Equation 4.4 and 4.5.

For the electron-hole pair transport, a temporal model is implemented considering the three-dimensional distribution of carriers. The applied bias and coulomb field between neighbouring carriers are taken into account using Equation 4.6 and material parameters such as the electron and hole carrier mobilities and used for the calculation of drift and diffusion components of carrier movement using Equation 4.7 and 4.8. At each time increment, carrier recombination and trapping (Equation 4.9) are checked, and carriers that recombine or trapped are removed from simulations.

4.2.2 Radiation transport

X-ray photon and secondary electron interactions in the presence of an external electric field are modeled by PENELOPE[50], and the locations of inelastic electron interactions with energy deposition are coupled with the transport routines for electron-hole pair simulations. The photon and electron particle tracks of 100 keV monoenergetic x rays are simulated. Figure 4.7 depicts the absorption of a pencil beam of x-ray photons perpendicularly incident on the a-Se detector (in green). Most photons are absorbed in the center of the detectors, and the off-center photons are due to Compton scattering, and fluorescence.

Since fluorescent photons emission is isotropic in the detector material, there is a high probability of escape when the photon is created at the surface of the detector, and not reabsorbed. In the case of reabsorption, the interaction site of fluorescent photon can be far from the initial interaction site depending on the photon energy. Figure 4.7(b) is the close-up of (a) and shows the secondary electrons moving in a random walk fashion and deposit energy at random locations in the photoconductor (in red). The range of electrons are dependent on the carrier energy and the amount of spreading increases when the carriers have more initial energy. The off-center oblique x rays in Figure 4.7(b) are due to generation and reabsorption of fluorescent photons above the a-Se material K-edge. The combined effect of Compton scattering, fluorescent reabsoprtion and spreading due to high-energy electrons are major causes of loss of spatial resolution in direct detectors. Figure 7.14(d) is the pixelated intensity profile in terms of number of electron-hole pairs detected for 100 keV monoenergetic x rays. Additionally, cone beams are more commonly used in clinics instead of point sources or pencil beams, which lead to oblique incidence of

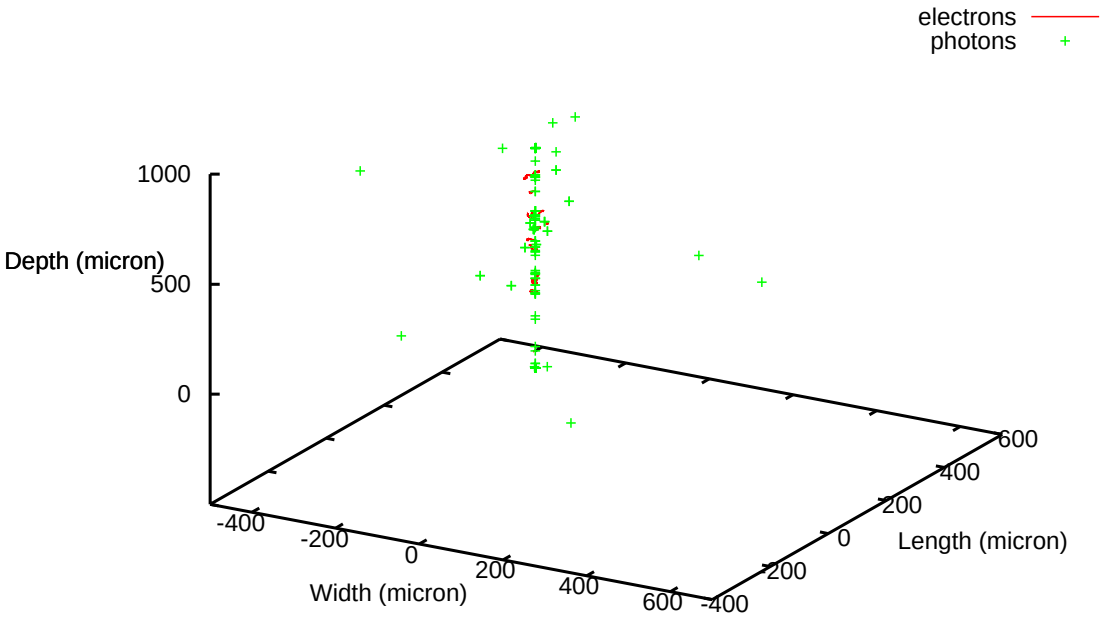

(a)

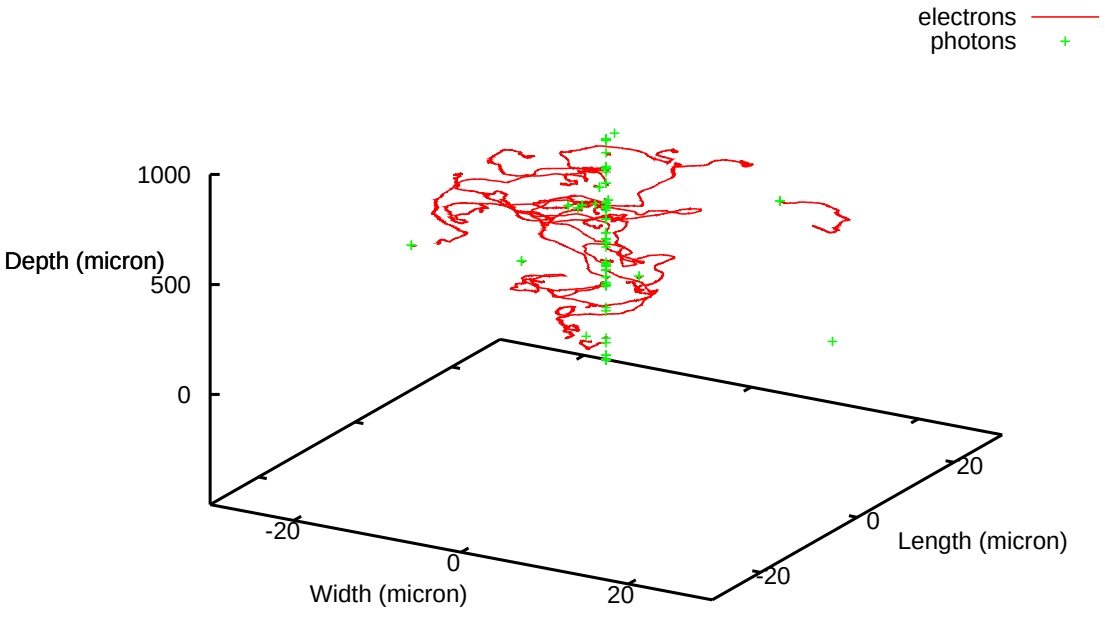

(b)

Figure 4.7: (a) Particle track of 100 keV incident photons (100 histories) in selenium. (b) Close-up of (a).

x rays that are not directly perpendicular to the detector surface. These oblique x rays can lead to additional blurring in the detector response.

4.2.3 Secondary electron interactions

To further show the energy deposition events as high energy electron loses kinetic energy in the semiconductor material, Figure 4.8 depicts the single high-energy electron track produced by a 40 keV and 140 keV x-ray photons. The bubble size is largest at the beginning of the track where the high-energy electron is created and gradually decreases as energy is deposited in the semiconductor material. The size of each bubble correspond to the burst size, r_{burst}, calculated using Equation 4.4.

Each electron track corresponds to one photon history, and the tracks are random because of the stochastic nature of the electron random walk in the detector. The bubble size corresponds to the electron kinetic energy depicted previously in Figure 4.8 and is proportional to the burst size. The amount of spreading due to electron energy is demonstrated for 40 and 140 keV incident photons. According to Equation 4.4, the high-energy secondary electron created from photoelectric absorption of a 40 keV photon is much lower compared to that of a 140 keV photon. Thus, the charge spreading due to the electron random walk is also much more significant for the 140 keV case. Each bubble in the plot corresponds to a site of energy deposition which will lead to generation of electron-hole pairs.

4.2.4 Generation of electron-hole pairs

The electron-hole pairs in bursts are generated from the deposition of energy are transported to the electrodes and may get trapped or recombine using Equation 4.2. All of these processes take place under an applied electric field. Figure 4.9 through 4.11 illustrate the creation of two burstst of electron-hole pairs from sites of energy deposition with a random distribution inside the burst radius calculated using Equation 4.4. Once the electron-hole pairs are initialized, many recombine due to the concentration of carriers in close proximity shown in Figure 4.10, and the remaining carriers are pulled by applied electric field toward opposing electrodes where recombination and trapping occurs shown in Figure 4.11 simulated using Equation 4.8 and 4.9.

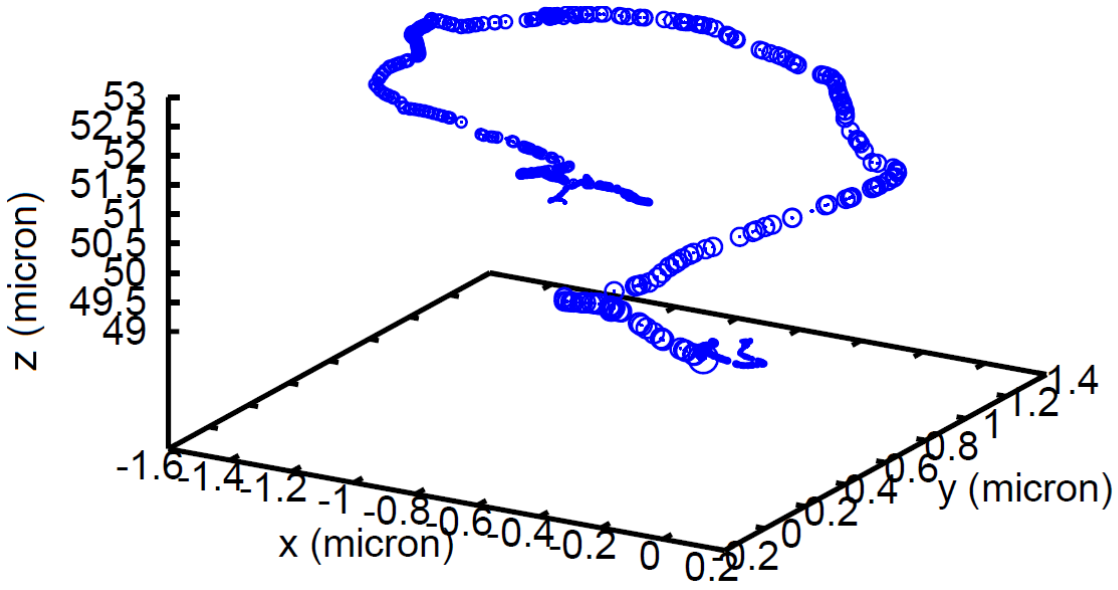

(a)

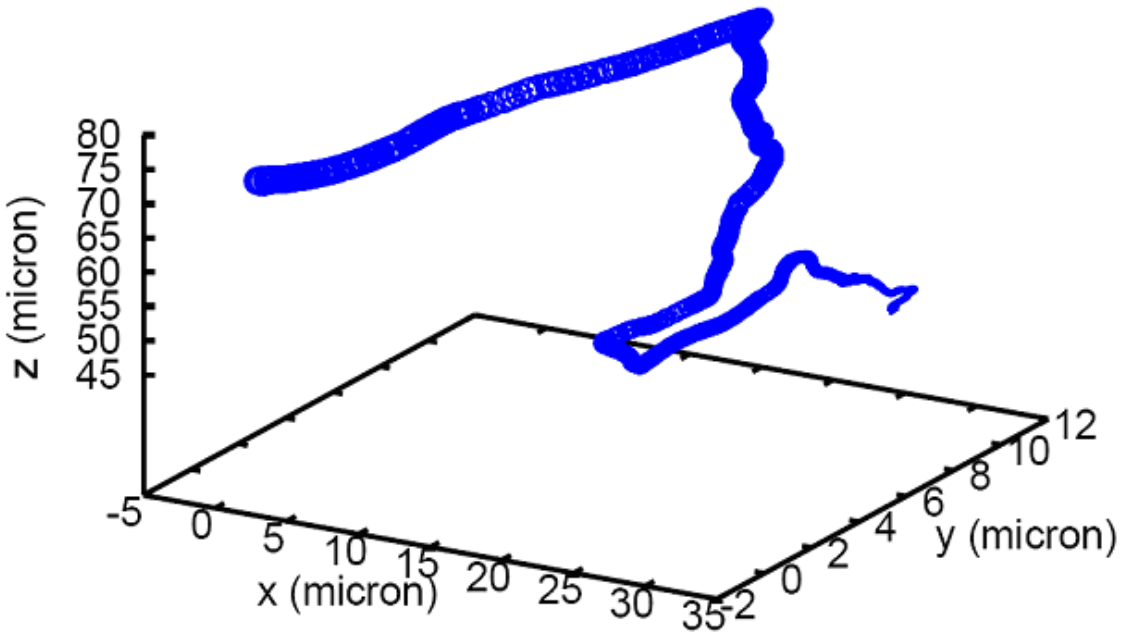

(b)

Figure 4.8: (a) 3D bubble plot of energy deposition events by secondary electrons from one simulation history of a 40 keV photon. (b) 3D bubble plot of energy deposition events by secondary electrons created from one simulation history of a 140 keV photon.

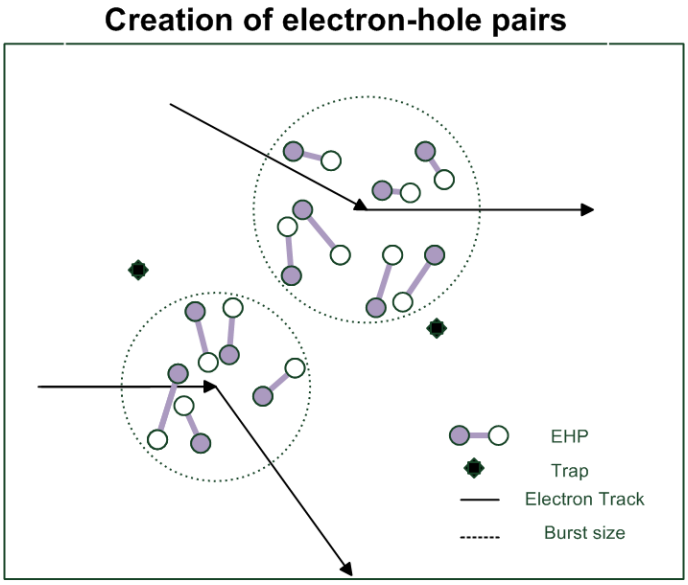

Figure 4.9: Generation of electron-hole pairs from inelastic electron interactions, with varying burst size and thermalization distance.

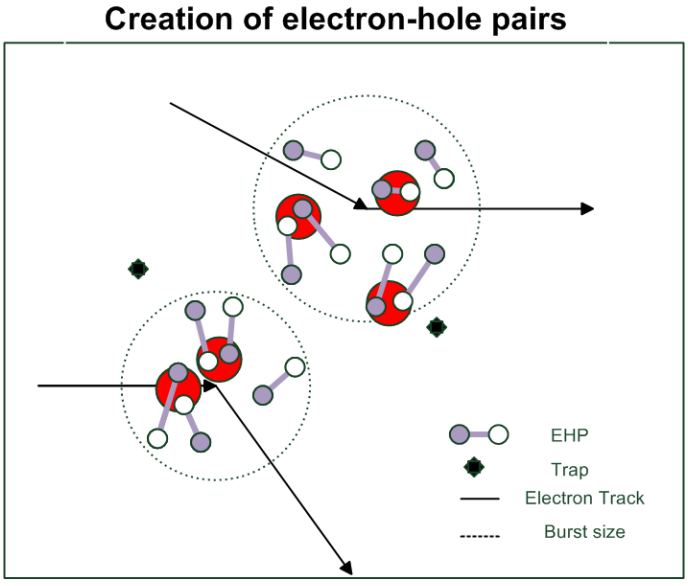

Figure 4.10: Recombination of many electron-hole pairs upon creation.

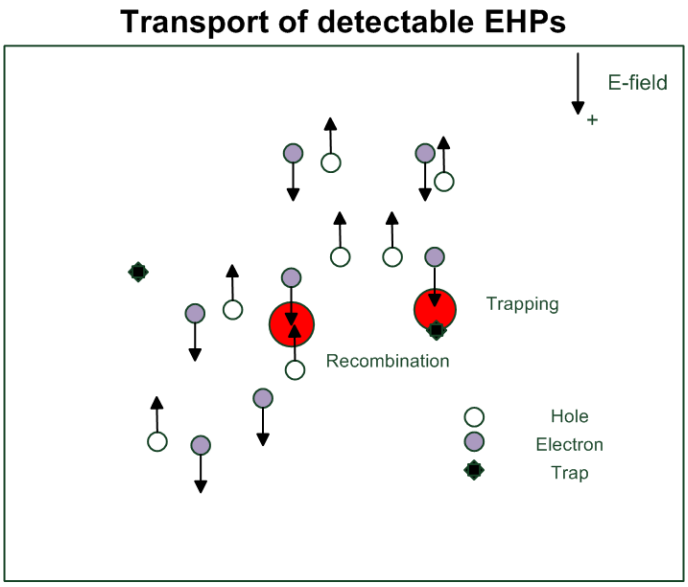

Figure 4.11: Transport of electron-hole pairs, charged carriers can be lost due to bimolecular recombination and deep trapping.

4.2.5 Carrier transport

The recombination of carriers is checked at each simulation step, Δt, in Equation 4.8. Recombination occurs when an electron and a hole are sufficiently close together, making the Coulomb attraction so strong that they cannot escape each other. As carriers approach each other due to Coulomb attraction, their drift component from the Coulomb field increases as an inverse function of separation distance squared shown in Equation 4.6. Thus, as the separation distance is reduced, the simulation time step also should be reduced in order to accurately capture the movement of the carriers as they come close to each other. However, this comes at the expense of simulation time. To solve this problem, a recombination distance was used by Bartczak *et al.*[96, 97, 98, 99] in their study of ion recombination in irradiated nonpolar liquids. In Bartczak's work, the recombination radius is a threshold used in the recombination model to stop simulations when a hole and an electron are found sufficiently close to each other. This parameter is needed because as oppositely charged carriers approach each other, their Coulomb attraction increases, and the distance between the electron and hole invariably decreases but never reachs zero, coupled with an increase in the probability of recombination. Therefore, each carrier's trajectory is tracked until they reach a critical recombination radius with an oppositely charged carrier.

At that point, recombination occurs. For electron-hole pair transport, typical electron-hole pair separation distances are in the range of 4 to 7 nm depending on the amount of energy deposited per pair described in Equation 4.1. Since the carrier attraction due to Coulomb field is governed by Coulomb's law with inverse separation distance squared, at 1 nm separation, the magnitude of the attraction has been increased by at least one order of magnitude from the initial separation, thus much less likely to escape recombination. For simulation purposes, recombination radii of 0.5 and 1 nm have been tested, and the 1 nm case in comparison to the 0.5 nm case has been found to not hinder accuracy of the recombination statistics while improving simulation time. This assumption is consistent with previous works by Bartczak *et al.*[96, 97, 98, 99].

Figure 4.12 show the sample transport tracks of three electron-hole pairs in electric field taken into account drift alone using Equation 4.7, with both drift and diffusion using Equation 4.8. In Figure 4.12(a), holes are clearly attracted to electrons, and drift towards them leading to recombination.

Electron tracks are much smaller compared to holes because the hole mobility is approximately thirty times greater than the electron mobility in a-Se [100]. In Figure 4.12(b), the random Brownian motion is taking into account as carrier diffusion and the carrier tracks are altered.

4.3 Pulse-height simulations

Figure. 4.13, 4.14 and 4.15 show the simulated pulse height spectra using detailed spatiotemporal MC simulation, for electron-hole pair creation, transport with recombination only, and transport with recombination and trapping cases and a range of monoenergetic incident energies.

The electron-hole pair creation case samples the number of electron-hole pairs generated from energy deposition events without transport using Equations 4.1 through 4.3. This case represents the maximum (sensitivity or) number of electron-hole pairs generated, and could be potentially collected with perfect transport, i.e., without recombination and trapping. For the transport with recombination only case, many bursts of electron-hole pairs are generated, initialized and transported. The transport takes into account carrier diffusion due to Brownian motion and drift due to the external applied electric field and Coulomb attraction/repulsion due to neighbouring carriers. The probability of trapping is assumed to be zero for the recombination only case. For the transport with recombination and trapping case, both recombination and trapping of electron-hole pairs are taken into

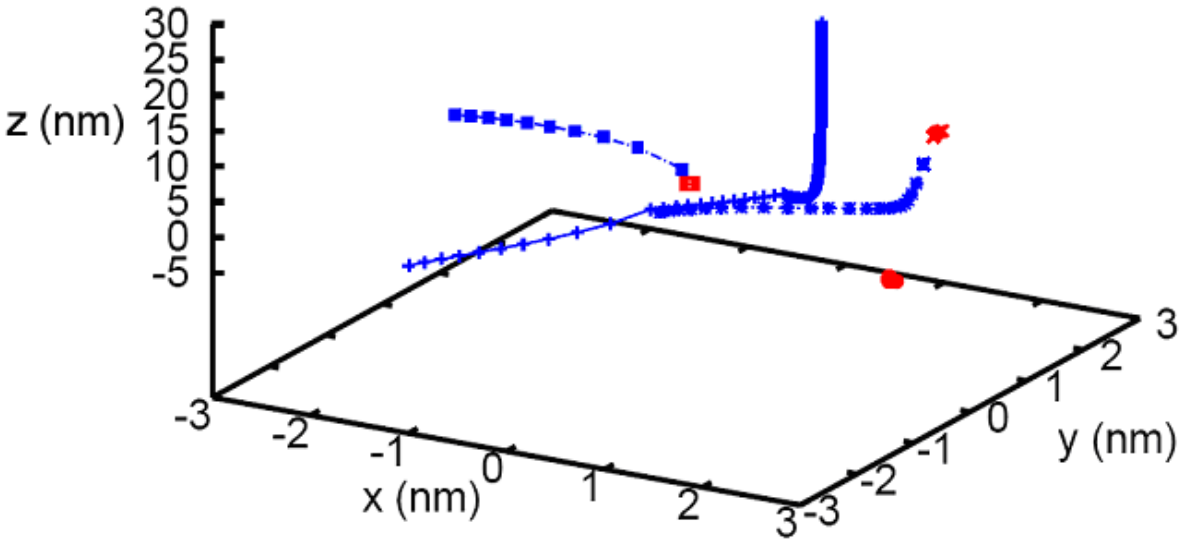

(a)

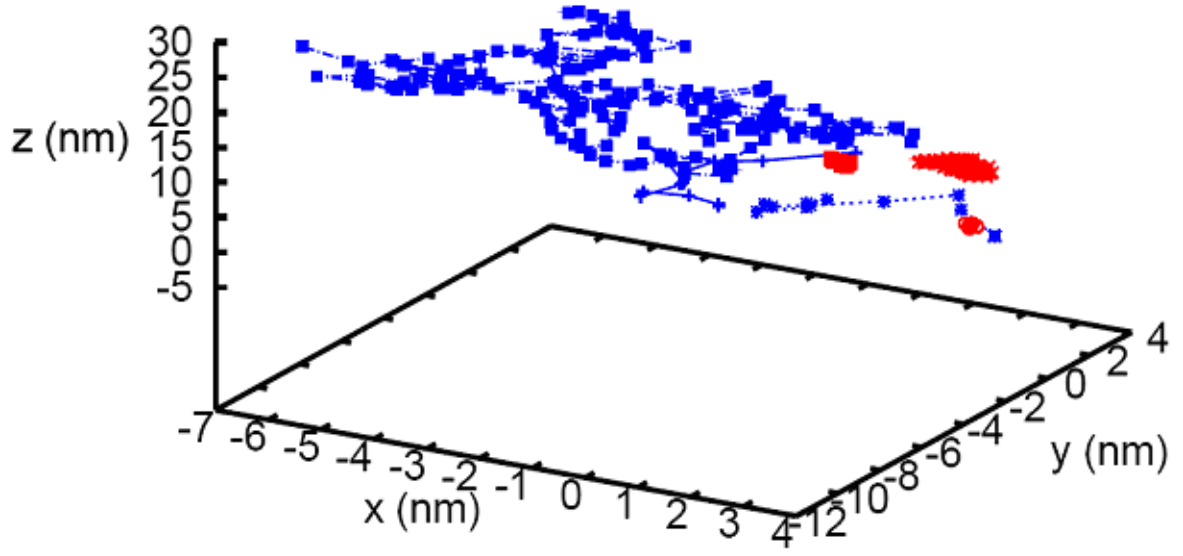

(b)

Figure 4.12: (a) Sample transport simulation track of three electron-hole pairs in electric field taking into account drift. (Electron and hole tracks in red and blue, respectively.) (b) Sample transport simulation track of three electron-hole pairs in electric field taking into account drift and diffusion.

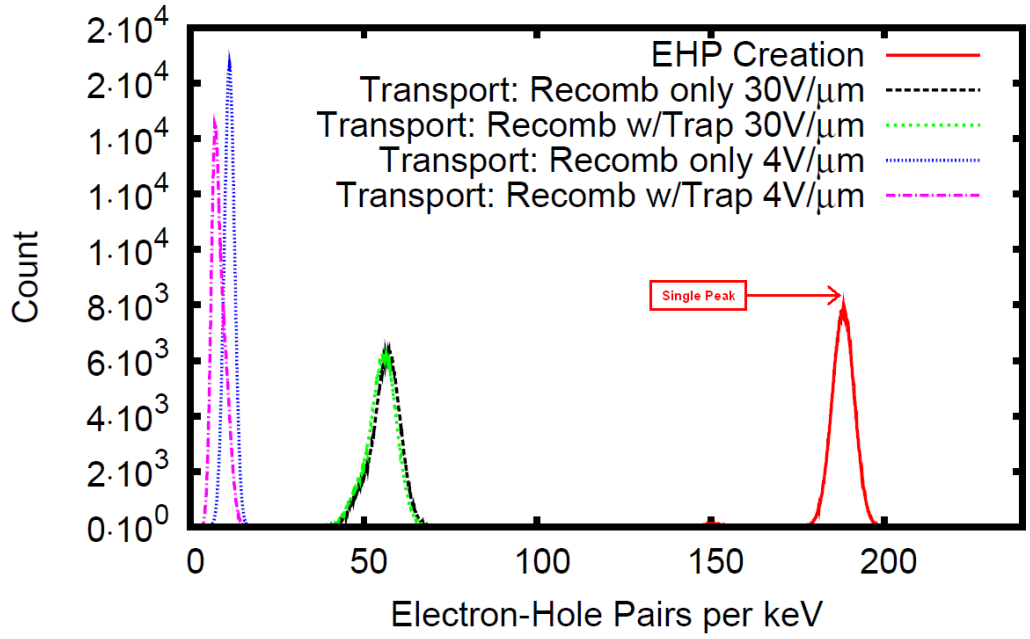

Figure 4.13: Results of the detailed spatiotemporal Monte Carlo simulation. Plots of the pulse height spectra, for no electron-hole pair transport, and transport with 4 and 30 V/μm applied electric field with recombination only and with recombination and trapping for 12.5 keV monoenergetic incident-photon energies.

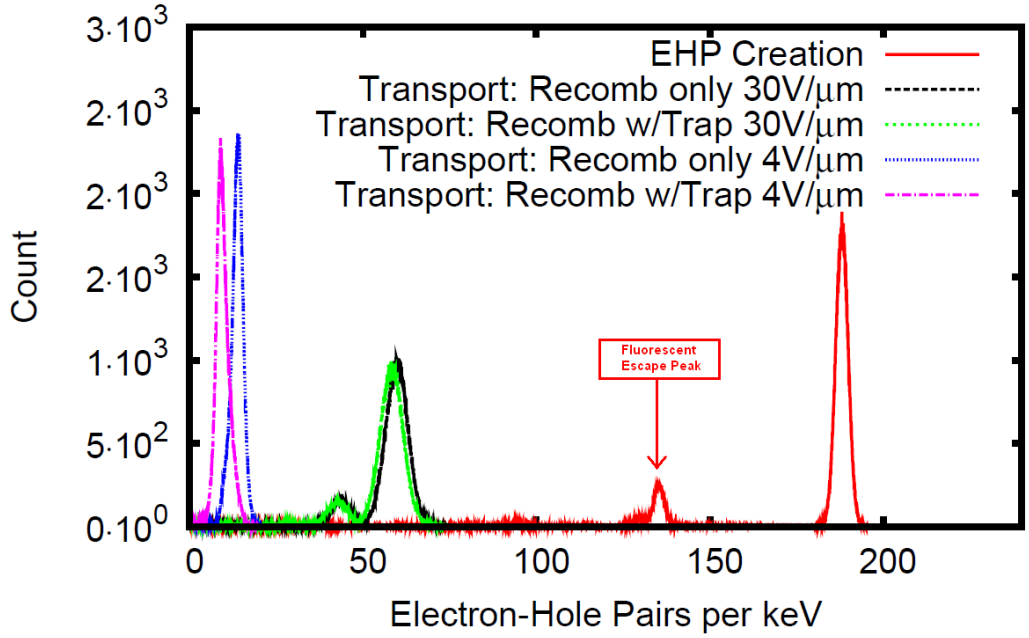

Figure 4.14: Results of the detailed spatiotemporal Monte Carlo simulation. Plots of the pulse height spectra, for no electron-hole pair transport, and transport with 4 and 30 V/μm applied electric field with recombination only and with recombination and trapping for 40 keV monoenergetic incident-photon energies.

account for carriers moving in the detector. The x axis shows the number of electron-hole pairs per keV, i.e., normalized by the incident photon energy. This allows for a simpler comparison between the PHS at different photon energies. For accuracy, the bin size used is 10 electron-hole pairs per keV.

In Fig. 4.13, the incident photon energy is 12.5 keV. There are five distinct spectral peaks corresponding to five different simulation cases: electron-hole pair creation, transport with recombination only at 30 V/μm and 4 V/μm, and transport with recombination and trapping at 30 V/μm and 4 V/μm. The highest spectral peak in the far right corresponds to the electron-hole pair creation case. The PHS consists of a single spectral peak because the incident photon energy is below the K-edge of a-Se. In Fig. 4.14, the incident photon energy is 40 keV, above the K-edge, and an additional lower spectral peak is observed due to generation and escape of fluorescent photons. In Fig. 4.15, the incident photon energy is 140 keV, well above the K-edge, and significant lower energy counts are observed due to Compton scattering.

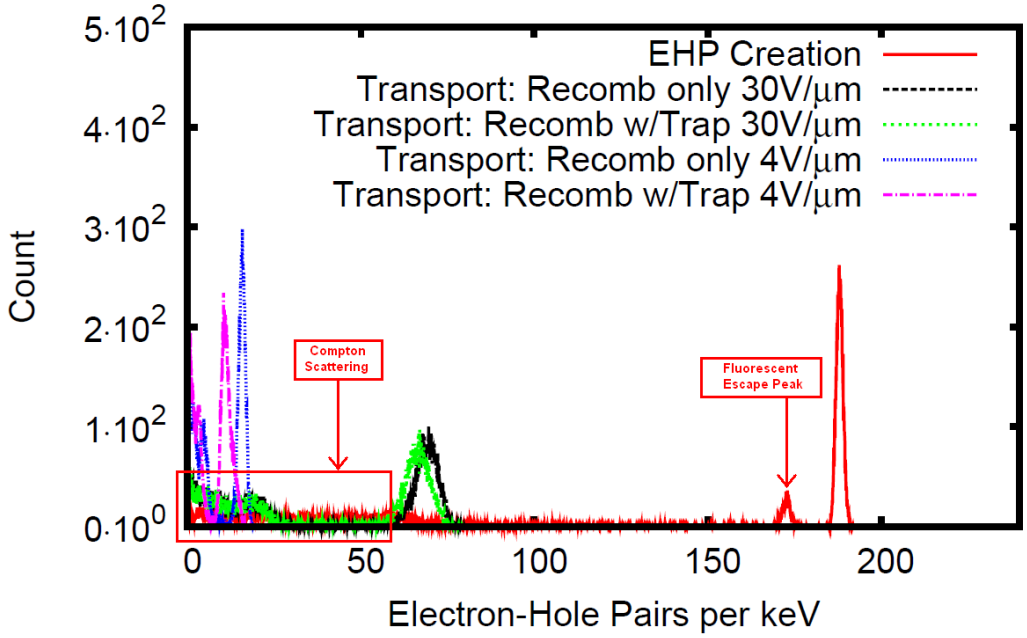

Figure 4.15: Results of the detailed spatiotemporal Monte Carlo simulation. Plots of the pulse height spectra, for no electron-hole pair transport, and transport with 4 and 30 V/μm applied electric field with recombination only and with recombination and trapping for 140 keV monoenergetic incident-photon energies.

When the transport of electron-hole pairs is taken into account considering recombination using Equations 4.6 and 4.8, we observe that the spectral peak is significantly shifted to the left because the number of electron-hole pairs detected is reduced due to recombination. The detection statistics also vary as a function of the applied electric field. For example, the PHS at 30 V/μm versus 4 V/μm transport have different spectral peaks. At high-bias conditions, the carriers travel faster and thus more electron-hole pairs are detected.

When trapping is taken into consideration using Equation 4.9 in conjunction with recombination, the effect of electric field becomes more apparent. For example, at low-bias conditions, for instance 4 V/μm, the simulated PHS shows a significant shift to the left. However, at high-bias conditions, for instance 30 V/μm, the effect of trapping on the number of electron-hole pairs detected is small.

Fig. 4.16 depicts the number of detected electron-hole pairs as a function of electric field and incident photon energy taking into account recombination and trapping. As the

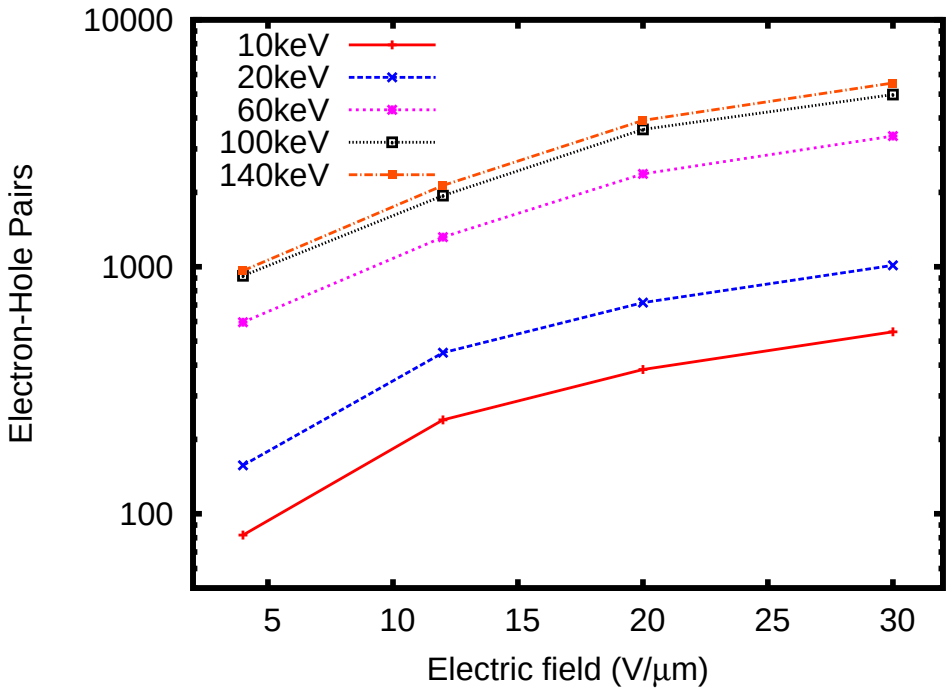

Figure 4.16: Detected EHP as a function of incident photon energy and applied electric field.

electric field increases from 4 to 30 V/μm, the number of detected electron-hole pairs increases. The number of detected electron-hole pairs also increases if the incident photon energy is increased, leading to more energy depositions. Using Equation 4.2, this increase in energy deposition leads to the generation of a larger number of carriers.

Figure 4.17(a) shows the Swank factor calculated from the simulated PHS as a function of incident photon energy. For the electron-hole pair creation case, the Swank factor is close to 1 at energies below the K-edge, and drops sharply at energies slightly higher than the K-edge. The Swank factor slowly recovers as the photon energy increases, up to approximately 40 keV, where it starts to fall again due to an increase in Compton scattering events. The transport with recombination only, and with recombination and trapping cases shows slightly reduced Swank factors due to transport, with similar trends. Significant degradation in the Swank factor is observed for the transport with recombination and trapping case at low field conditions (4 V/μm) due to low carrier mobility and trapping effects.

Figure 4.17(b) shows the DQE at zero spatial frequency calculated from the simu-

lated Swank factor and quantum efficiencies calculated from attenuation coefficient data (as a function of x-ray energy) taken from the Lawrence Berkeley National Laboratory databases[101]. The simulation results in Figure 4.17 use the full distribution of output signal consistent with Equation 3.6 The simulated DQE at zero frequency results take into account the detailed transport of electron-hole pairs, which results in a lower Swank factor and DQE compared to the single photo-peak model.

4.4 Experimental comparison

4.4.1 Gaussian parameters

Fig. 4.18 shows the Gaussian fit parameters used in Equation 3.7 for simulated and experimental[74] PHS at 40, 60 and 140 keV as a function of electric field. The PHS is analytically fitted considering only the highest spectral peak in the distribution, and the Gaussian mean and variance are calculated. This method ignores all other peaks at lower energies (due to K-fluorescence, Compton and noise) and provides a very poor estimate of the PHS distribution. Fig. 4.18(a) show a comparison of the simulated and experimental mean of the PHS distribution as a function of the applied field. As the field increases, the mean number of detected electron-hole pairs and its variance increases. The number of electron-hole pairs also increases as the incident photon energy increases. The experimental data shows higher variance compared to the simulated data. This difference could be attributed to the perfect monoenergetic sources used in simulations in comparison to radioisotpes and multiple filter combinations used to generate near monoenergetic x-ray input spectra in the experiments. In addition, electronic noise and read-out circuits introduce additional variance in the measurements.

4.4.2 Swank factor

The differences in the simulated and experimental Swank noise are depicted in Fig. 4.19(a), the simulated Swank factors are obtained using Equation 3.7. The simulated and experimental Swank factors have approximately 2% difference. Simulated Swank factors are in all cases higher than their experimental counterparts because of lower variance compared to the experimental data. In the experimental setup, longer amplifier shaping times of up to 64 μs are used to accommodate for the low electron mobility in a-Se and additional noise sources due to external high voltage and read-out electronics need to be taken into

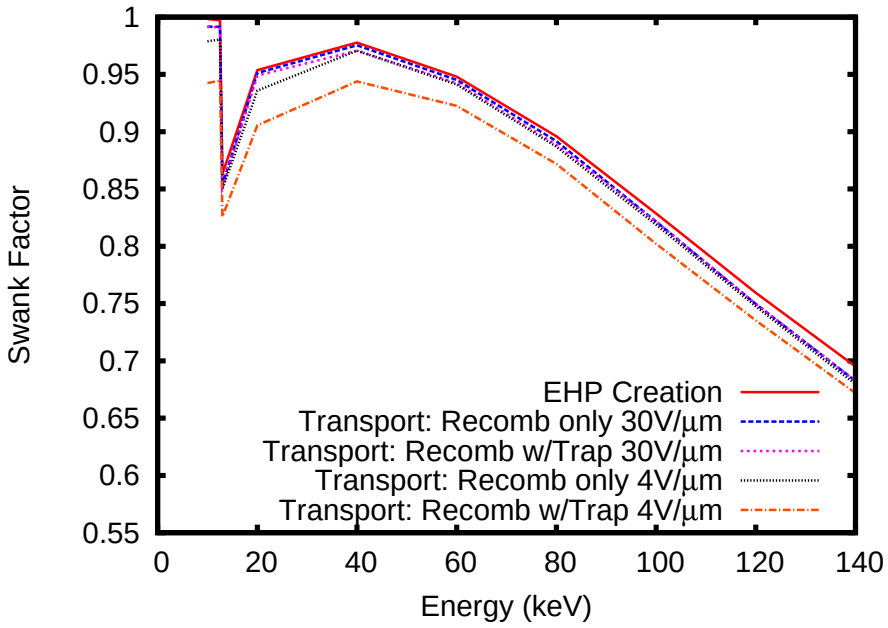

(a)

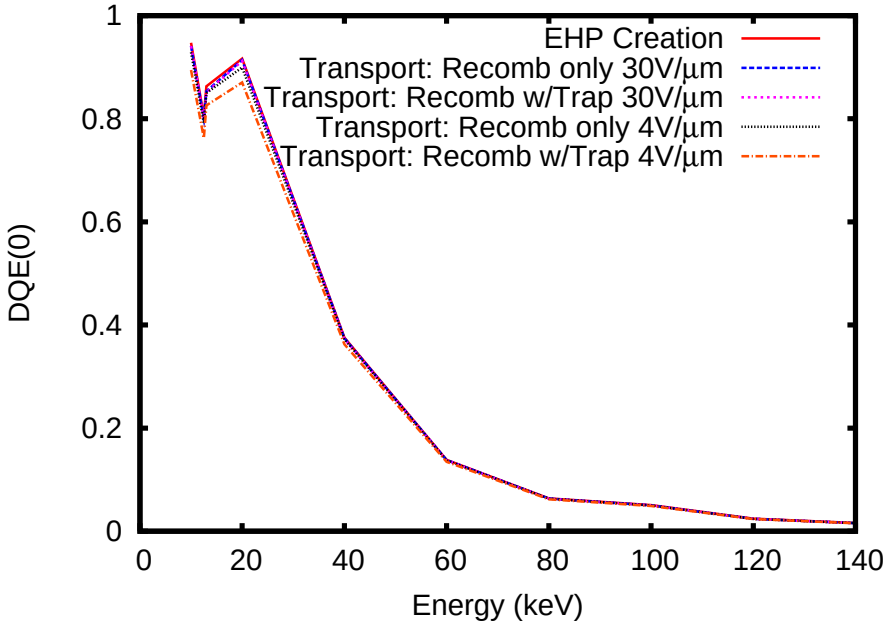

(b)

Figure 4.17: (a) Simulated Swank factor as a function of incident photon energy. (b) Simulated DQE at zero spatial frequency as a function of incident photon energy.

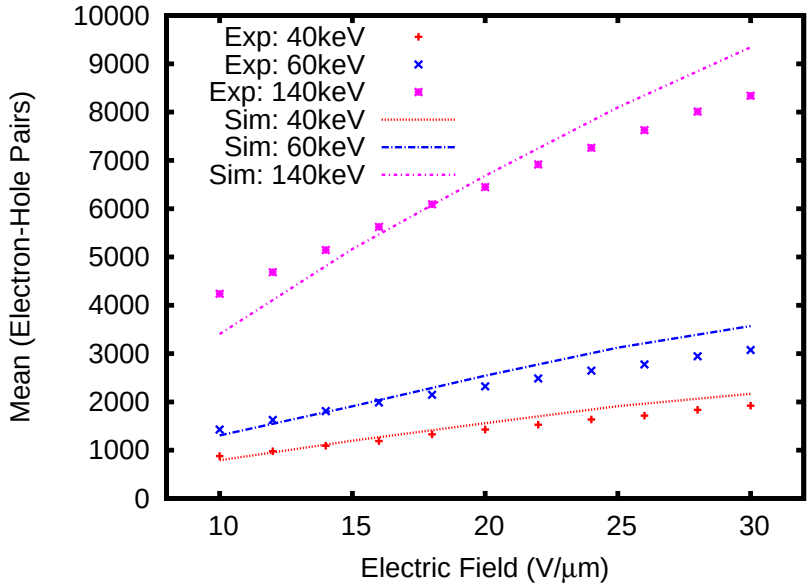

(a)

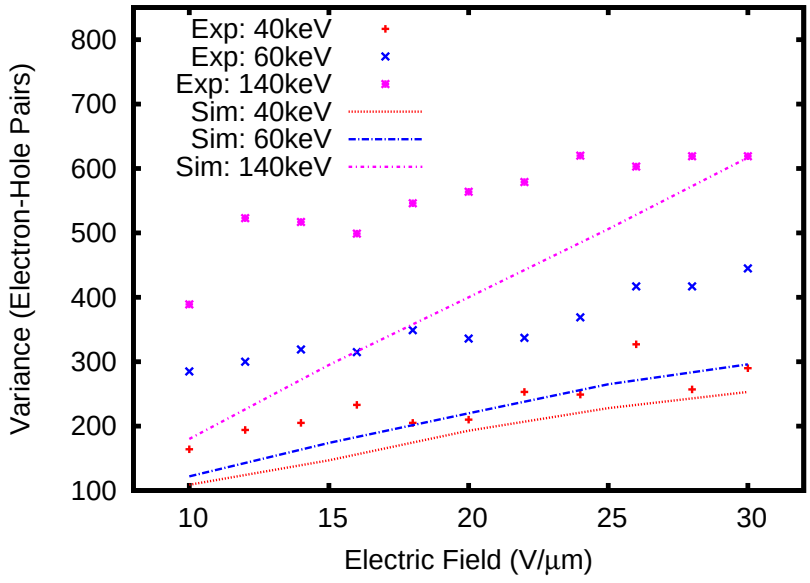

(b)

Figure 4.18: (a) Comparison of simulated and experimental PHS - Gaussian fitted mean of the highest spectral peak as a function of the applied field. (b) Comparison of simulated and experimental PHS - Gaussian fitted variance of the highest spectral peak as a function of applied field.

account. Similar trends are observed between simulated and experimental Swank factors as the x-ray energy increases. Though not shown in the graph, this increasing trend of the Swank factor as a function of electric field (Equation 4.7) has been verified with simulations at 4 V/μm.

Fig. 4.19(b) shows a comparion of measured and simulated Swank factor as a function of incident x-ray energy. The plot shows an interesting comparison between Swank factors calculated from Gaussian fitting (using Equation 3.7) of the highest spectral peak versus taking into account the full PHS distribution using Equation 3.6. Significant differences in the Swank factor results are observed between the two methods. For instance, at 140 keV, the Gaussian fitted Swank is almost 1, while the Swank factor taking into account the entire distribution is less than 0.7. Again, the Gaussian fitting method does not take into account Compton electrons, and K-fluorescent photon generation and escape.

4.4.3 Discussion

The model we utilize in this work consists of a physics-based, Monte Carlo model to simulate the PHS as a function of incident photon energy, and applied electric field. It incorporates the effects of recombination and trapping in electron-hole pair transport.

For the simulation of electron-hole pairs, the current implementation samples the number of carriers generated with the corresponding burst size and thermalization distances. Equation 4.2 is used to sample the number of electron-hole pairs generated, and the burst size and thermalization distance are calculated using Equations 4.4 and 4.1. The subsequent transport takes into account the electron-hole pairs generated, one burst at a time. When the secondary electron energy is high, the mean free path is larger in comparison to the burst and thermalization distances. However, when the secondary electron slows down, its range is reduced, and energy deposition events could happen closer together, potentially causing bursts to overlap with each other. From Equation 4.4, the burst size is also a function of the secondary electron energy and thus a reduction in the kinetic energy also cause a higher concentration of the generated carriers. Ideally, all bursts should be simulated at the same time to include overlapping effects in burst creation process and transport. However, since the run time increases with the number of carriers simulated simultaneously, a simpler implementation may be to simulate multiple bursts taking into consideration the distances between energy deposition events, where bursts generated in close proximity can be simulated together to improve the physical accuracy of the model. Additional adjustments can be made to the Δt in Equation 4.8, to find the optimal simulation time versus accuracy and variance.

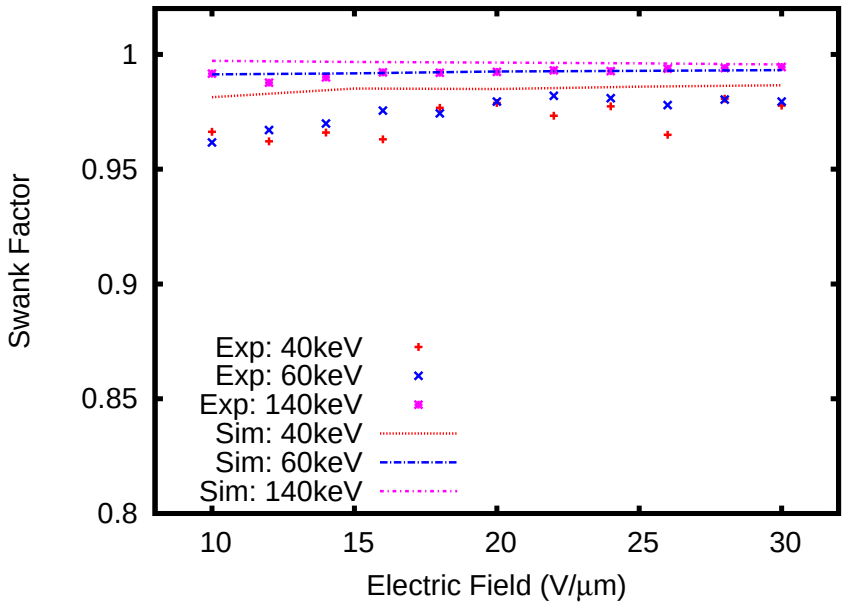

(a)

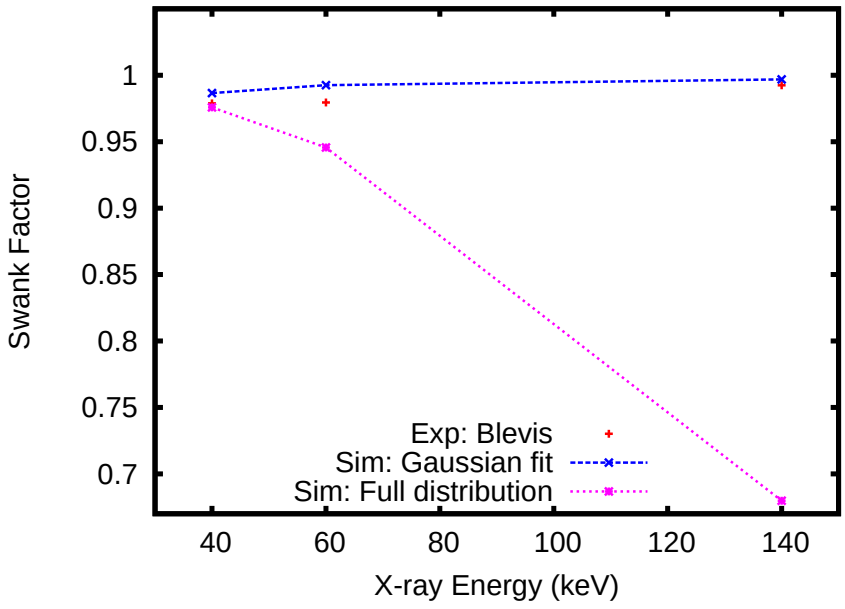

(b)

Figure 4.19: (a) Comparison of measured and simulated Swank factor as a function of the applied field. (b) Comparison of measured and simulated Swank factor as a function of incident-photon energy at 20 V/μm.

Recombination of electron-hole pairs leads to significantly fewer detected carriers, especially with a low external electric field. In our work, recombination is considered to occur when a hole and an electron are within 1 nm of each other, where Coulombic attraction is assumed to be so strong that they cannot escape. However, since there are many electron-hole pairs moving in the burst, several carriers can be found within the recombination radius at one time. In the current implementation, a first-hit search method was used. For each free carrier, the first carrier found to be in the recombination radius is chosen to be the carrier to be recombined. However, an exhaustive method can be used to search for the nearest neighbor for recombination. In principle, this nearest neighbor method is physically more accurate. In previous work[10], we have reported that the mean recombination probability for the first-hit and the nearest neighbor techniques are the same in point bursts, but differs in variance. The nearest neighbor method is also much more time consuming compared to the first-hit model and may require parallelization and additional speed up in order to be feasible in full x-ray signal formation simulations. The recombination probabilities using the nearest neighbor and first-hit methods need to be studied in more detail.

Trapping has a significant effect on electron-hole pair transport, especially in low applied electric field conditions where the carrier mobility is low. The current implementation using Equation 4.9 considers only deep trapping of carriers with a constant carrier lifetime. When carriers are trapped, they are considered lost. More complex trapping models can be added in the future considering shallow traps, carrier releasing from traps, and trap filling effects.

Detector thickness is an important parameter to be considered for detailed transport simulation of electron-hole pairs and for DQE calculations. We show results for a detector thickness of 150 μm. For transport simulations, carrier transit time in the semiconductor material is directly proportional to its thickness. Using equation 4.7, with a constant carrier mobility and an increase in the transit time due to a thicker photoconductor, the probability of the carrier getting trapped increases as well, thus affecting the PHS. Additionaly, since the attenuation of the primary x-ray beam is a function of thickness, the DQE calculations are also affected. Therefore, the PHS and Swank factors for detectors with a range of thickness should be further studied.

As the detector thickness increases, a higher applied voltage is required and the material properties of the the blocking layers between a-Se and charge collecting electrodes play a significant role in reducing the dark current. Dark current can be due to charge injection from the biasing electrodes, and thermal emissions from the bulk material. In the current implementation, only the a-Se material is taken into account for photocurrent simulations, and non-idealities such as dark current models can be explored to improve the model accuracy in the future.

Chapter 5

Simulation studies using clinical spectra

For medical imaging applications, clinical x-ray spectra are used instead of monoenergetic x rays. This section extends the work in Chapter 4 to study the performance of a-Se detectors using different clinical mammography spectra.

5.1 Clinical mammography spectra

The MC code can simulate PHS not only for monoenergetic x-ray photons, but for x-ray spectra as well. The PHS for two known test mammography beam qualities has been simulated taking into account trapping and recombination effects. Figure 5.1 shows the energy spectrum of the two beam qualities used, generated with methods described by Boone et al.[83, 102] Both beam qualities are taken from the Standard Radiation Quality (IEC 61267), including tungsten and molybdenum anodes and a tube voltage of 28 kVp. The molybdenum spectrum (RQA-M 2) includes a molybdenum filter of 32 μm and an additional 2 mm aluminum filter. The tungsten spectrum includes an aluminum filter of 0.5 mm and the same 2 mm aluminum filter.

The simulated PHS for both radiation qualities are shown in Figure 5.2. The x-axis is in number of electron-hole pairs detected, and the two curves represent transport with 4 and 30 V/μm. Even though the molybdenum spectrum is more monoenergetic-like due to the two characteristic peaks, the corresponding Swank factor is worse. This is because the detector material properties, such as the K-edge energy where the Swank factor degrades

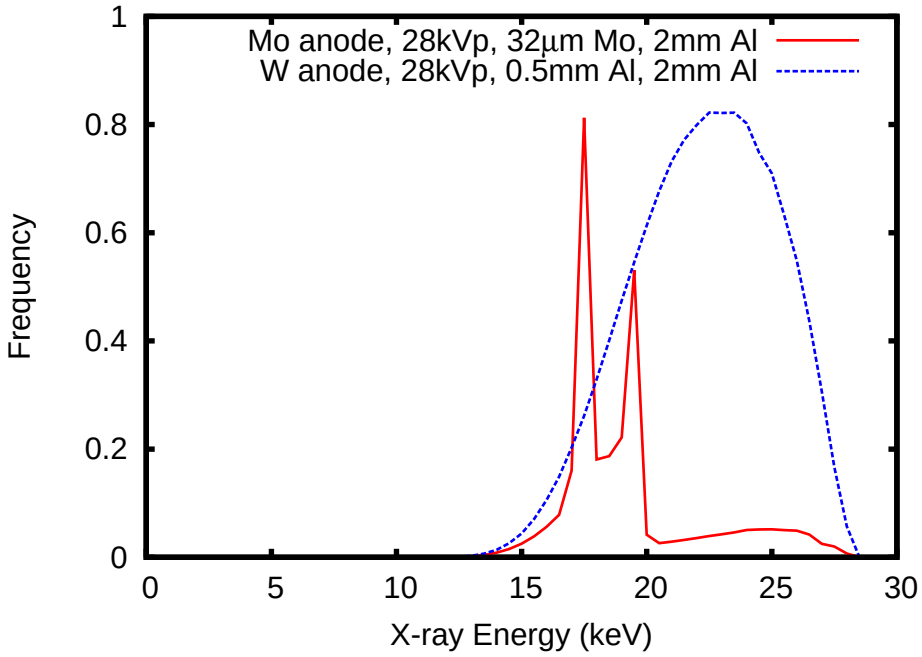

Figure 5.1: Mammography beam qualities used in the Swank factor simulations: Mo/Mo (RQA-M 2) and W/Al from standard radiation quality (IEC 61267). Mo/Mo (RQA-M 2) is a molybdenum anode with 28 kVp tube voltage, 32 μm molybdenum filter and 2 mm Al filter. W/Al is a tungsten anode with 28 kVp tube voltage, 0.5 mm Al filter and 2 mm Al filter.

significantly due to fluorescent x rays, need to also be taken into consideration. For a-Se, the K-edge energy is 12.6 keV and monoenergetic x-ray simulations in Fig 5.2(b) show that the Swank factor degrades significantly just above this energy, and recovers slowly as the energy increases. From the normalized input spectrum in Figure 5.1, the two characteristic peaks in the molybdenum spectrum are 17.5 and 19.5 keV, respectively, while the tungsten spectrum is centered around 23.5 keV. Even though the molybdenum spectrum may be more monoenergetic due to the two characteristic x-ray peaks, the PHS and the Swank factor are degraded. This is because when the spectra is detected by the a-Se detector, the incident photons are lower in energy and more near the K-edge.

Inherently, Swank noise is caused by the variance on the detector signal output due to a number of physical interactions in the semiconductr material. For example, the Poisson sampling of the number of electron-hole pairs generated using Equation 4.2, and the random three-dimensional spatial distribution of carriers using the burst and thermalization

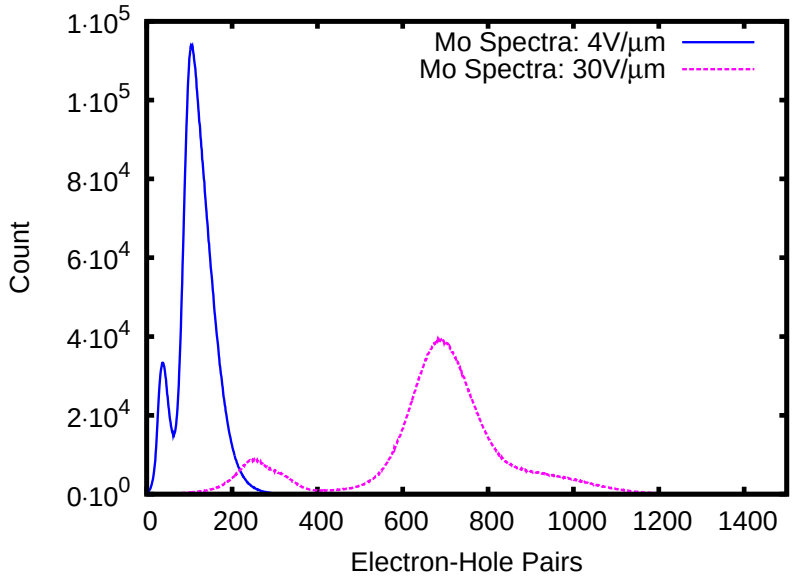

(a)

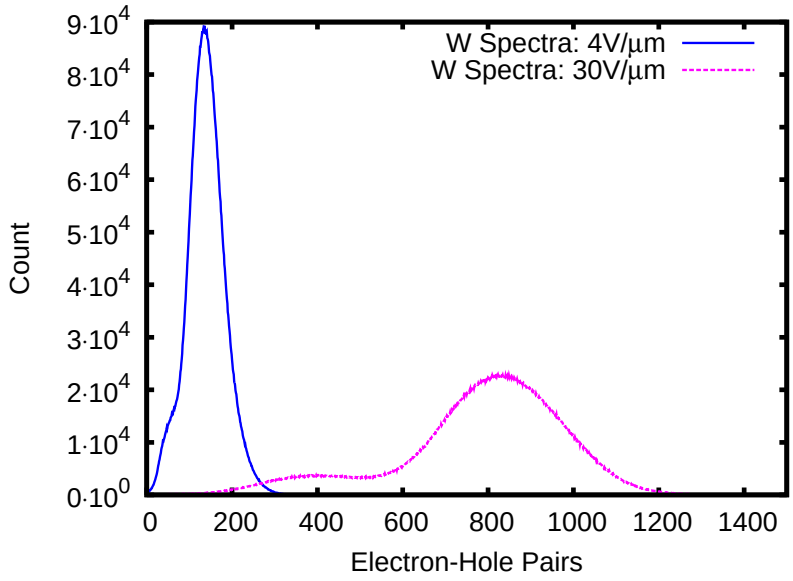

(b)

Figure 5.2: (a) Simulated PHS with molybdenum mammography spectra as a function of electron-hole pair transport for 4 and 30V/μm applied electric field. (b) Simulated PHS with tungsten mammography spectra as a function of electron-hole pair transport for 4 and 30V/μm applied electric field.

Table 5.1: Simulated Swank factor for Mo/Mo (RQA-M2) and W/Al standard radiation qualities with varying transport conditions.

Radiation Quality (IEC 61267)	4V/μm	30V/μm	No EHP Transport
Mo/Mo (RQA-M 2)	0.878	0.922	0.929
W/Al	0.903	0.937	0.945

distances calculated from Equations 4.4 and 4.1 can all lead to variations in the recombination fraction and the signal levels detected. Additionally, carrier trapping in the material modeled by Equation 4.9 introduces another source of variability beside recombination effects. After the carriers reach the collecting electrodes, electronic noise in the readout system can introduce more variations in the signal detected. The affect of electronic noise on the Swank factor and DQE is studied in this section using two methods for calculation of DQE at zero spatial frequency [103]. Figure 5.3(a) shows the quantum efficiency (or absorption efficiency of the incident x rays) of a-Se detectors for three values of thickness as a function of incident photon energy calculated using attenuation coefficient from PENELOPE database[50]. An increase in the quantum efficiency is observed due to the K-shell absorption. The PHS are simulated using ARTEMIS[95] for 6 to 28 keV, and the Swank factor for each energy is calculated and plotted in Figure 5.3(b).

The PHS for both radiation qualities are shown in Figure 5.4 (a) and (b) for molybdenum and tungsten anodes respectively. The simulated PHS inherently includes the energy weighting effects, and the Swank factor can be used directly to calculate the DQE listed in Table 5.1. The x-axis is in number of electron-hole pairs detected, and the curves represent transport with 4 and 30 V/μm bias, in the presence and absence of 50 electrons electronic noise. Electronic noise can be introduced during readout of the electronic signal. The introduction of electronic noise degrades the PHS and the Swank factor. As the electronic noise increases, the simulated PHS is further degraded with a widening of the distribution caused by the stochastic nature of noise.

5.2 Results

The monoenergetic Swank factor and the quantum efficiency shown in Figure 5.3(a) are used to calculate the DQE(0) using Equation 3.1 and the results are tabulated in Table 5.2 with the row heading "DQE(0) no weighting." In this case, the Swank factor at each energy is considered to have no spectral dependence, and the incident x-ray energies are assumed to have no effect on the number of detected electron-hole pairs. The individual

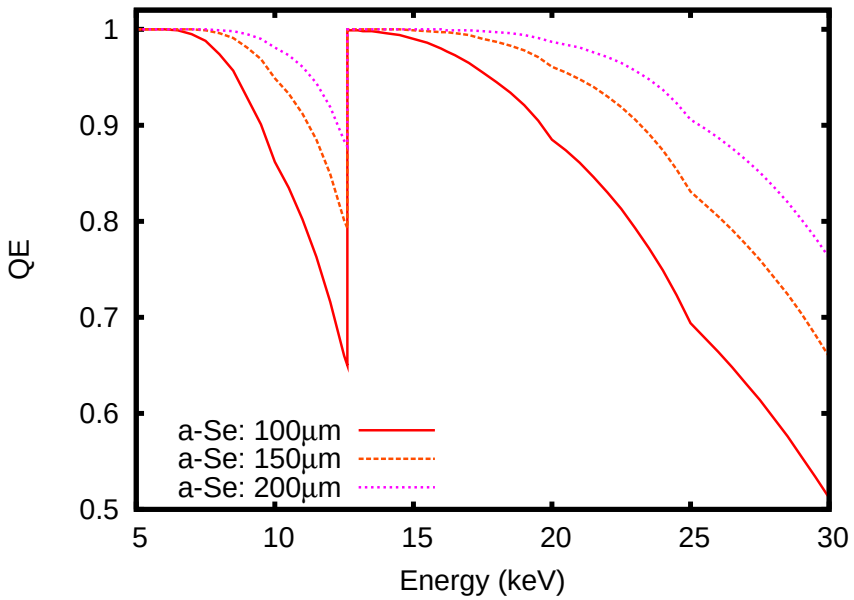

(a)

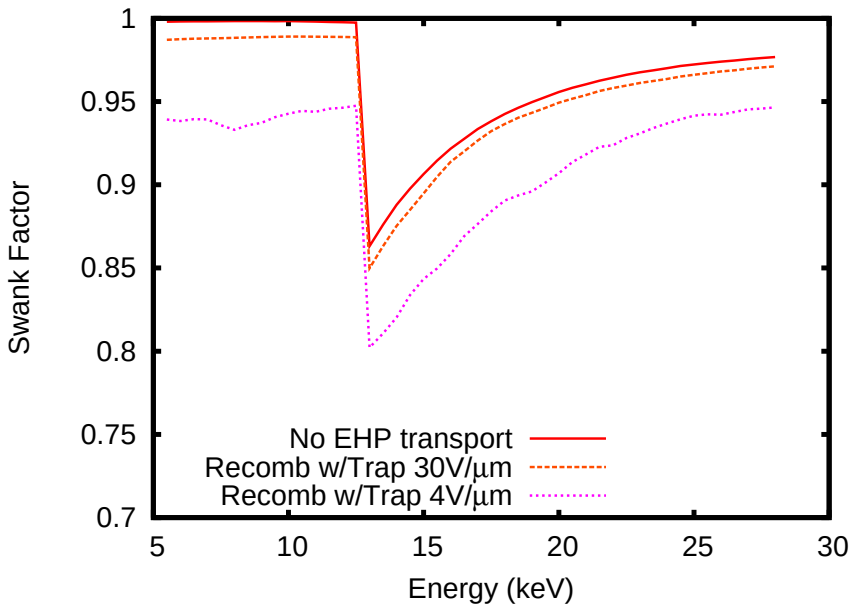

(b)

Figure 5.3: (a) Calculated quantum efficiency for three values of thickness of a-Se detector as a function of incident photon energy. (b) Simulated Swank factor as a function of incident photon energy and electron-hole pair transport conditions.

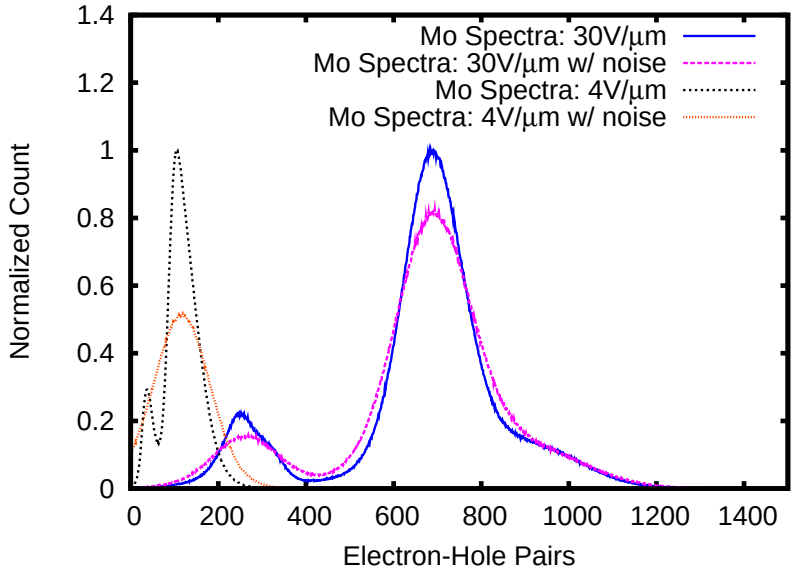

(a)

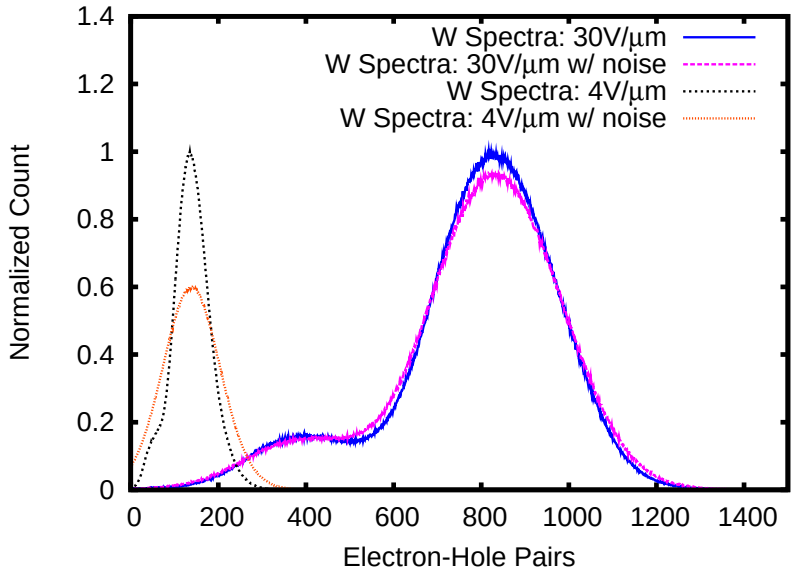

(b)

Figure 5.4: (a) PHS with molybdenum mammography spectra as a function of electron-hole pair transport for 4 and 30 V/μm applied electric field. (b) PHS with tungsten mammography spectra as a function of electron-hole pair transport for 4 and 30 V/μm applied electric field.

products of quantum efficiency (average over the entire spectrum) and the monoenergetic Swank factor are integrated over the entire input spectrum with no weighting applied to yield the DQE results. For noise considerations, a simple model of electronic noise is used for Swank factor and DQE calculations using a Gaussian distribution with a variance of 50 electrons as an initial study.

Table 5.2: Swank factor and DQE(0) for Mo/Mo (RQA-M 2) and W/Al standard radiation qualities with varying transport conditions.

Radiation Quality (IEC 61267)	Description	4V/μm	30V/μm	No EHP Transport
Mo/Mo (RQA-M 2)	$I(E)$ w/ weighting	0.878	0.922	0.929
	$I(E)$ w/ weighting & noise	0.772	0.917	0.929
	$DQE(0)$ no weighting	0.860	0.902	0.908
	$DQE(0)$ w/ weighting	0.843	0.885	0.892
	$DQE(0)$ w/ weighting	0.741	0.770	0.892
W/Al	$I(E)$ w/ weighting	0.903	0.937	0.945
	$I(E)$ w/ weighting & noise	0.816	0.934	0.945
	$DQE(0)$ no weighting	0.834	0.865	0.871
	$DQE(0)$ w/ weighting	0.818	0.849	0.856
	$DQE(0)$ w/ weighting	0.737	0.846	0.856

The Swank factor results with and without energy weighting for the molybdenum and tungsten spectrum are listed in Table 5.2. The simulation results with energy weighting are lower in comparison to the non-weighted results, and show a spectral dependence on the incident x-ray energies in the Swank factor and the DQE. This is because the higher energy x-ray photons create more electron-hole pairs compared to lower energy photons, hence they have a higher weighting in the Swank calculations, and the Swank factor is lower for energies above the k-edge as shown in Figure 4.13, 4.14 and 4.15. A simple noise model is included in the Swank factor and DQE simulations to give an initial estimation of the effect of electronic noise on the results. A noise level of fifty electrons was used as the variance using a Gaussian random variable where the individual pulse height counts are the mean. The PHS with electronic noise exhibits a wider peak in comparison to the no noise results, and this leads to a degradation in the Swank factor and DQE.

5.3 Optimization study

This section contain the details of an optimization study of mammography input spectra for a-Se detectors. In terms of the geometry, the x-ray source is directly above the a-Se detector and outputs a pencil beam perpendicular to the detector surface. The thickness of the a-Se material simulated is 150 μm. Two biasing conditions are simulated, with 4 and 30 V/μm, or 600 and 4500 V over the across detector thickness.

Table 5.3 lists the different mammography incident x-ray spectra used for the optimzation study. Eight mammography spectra are simulated in total. The first half is based on the RQA-M radiation quality, and the other half is based on anode/filter combinations with a constant tube voltage. The plots of these input spectra are included in the Appendix section for reference purposes.

Table 5.3: Radiation quality for optimization study.

Radiation quality	Approx. x-ray tube voltage (kV)	Filer thickness mm Al	Half-value layer (HVL) mm Al
Mo/Mo (RQA-M1)	25	0.032	0.56
Mo/Mo (RQA-M2)	28	0.032	0.60
Mo/Mo (RQA-M3)	30	0.032	0.62
Mo/Mo (RQA-M4)	35	0.032	0.68
Mo/Rh	28	0.025	0.65
Rh/Rh	28	0.025	0.74
W/Mo	28	0.050	0.75
W/Al	28	0.500	0.83

For the RQA-M radiation qualites, the anode and filter material are all made out of molybdenum. A constant filter thickness is used, but different x-ray tube voltages allow for the production the different x-ray spectra. The half-value layer (HVL) results are used to validate the attenuation of the x-ray beam from a layer of aluminum based on half of the initial beam intensity. For the remaining half of the mammography spectra, a constant tube voltage of 28 kVp is used in conjunction with different anode/filter material combinations to produce the output x-rays. Materials used for the anode and filter include a combination from molybdenum, rhodium, tungsten, and aluminum.

The simulated Swank factor results are listed in Table 5.4 below. These results are calculated from the simulated PHS based on the experimental setup described above. The actual simulation results are included in the Appendix section for reference. In general, the

anode/filter combination exhibited higher Swank factor compared to the RQA-M radiation qualities. This is because molybdenum have two characteristic x-ray enegies near the K-edge of a-Se, the degradation in Swank is apparent as shown in previous discussions in Section 4.3. Since the anode is molybdenum, the characteristic x-ray energies are the same for the molybdenum/rhodium case and thus lower Swank factor. For the rhodium and tungsten anode cases, the incident x-ray energy is shifted higher and the incident x-rays have a higher energy than the K-edge of a-Se. Thus, an improvement in Swank factor is observed. The highest Swank factor is for the rhodium/rhodium case, where not only is the incident energy relative far away from the a-Se K-edge, but the spectrum itself is the most monoenergetic, thus the least statistical variation in terms of the output spectrum and Swank factor. The ionized energy required to excite an single electron-hole pair described in Equation 4.3 is used in Equation 4.2 for the Poisson sampling of number of electron-hole pairs. Charge carrier transport in this section include both drift and diffusion components (Equation 4.8) for recombination and deep trapping using Equation 4.9.

Table 5.4: Swank factor results for optimization study.

Radiation Quality	4V/μm	30V/μm
Mo/Mo (RQA-M1)	0.886	0.931
Mo/Mo (RQA-M2)	0.878	0.922
Mo/Mo (RQA-M3)	0.870	0.913
Mo/Mo (RQA-M4)	0.852	0.892
Mo/Rh	0.893	0.933
Rh/Rh	0.903	0.938
W/Mo	0.905	0.942
W/Al	0.903	0.937

In this optimization study, we assume all the incident x-ray beam reachs the a-Se detector surface. However, in reality a portion of the incident x-ray photons are absorbed by the breast tissue during mammography. Since x-ray attenuation is a function of energy, the absorption of photons is not uniform across the incident x-ray spectrum. A higher portion of the low energy x rays are absorbed, and the x-ray beam is "hardened". Since the characteristic x rays produced by the molybdenum anode is of lower energy, they have a higher probability of being absorbed by the breast tissue, thus modifying the actual spectrum that is detected. This study can be improved by simulation of breast phantoms with different thicknesses and compositions to provide a more realistic model of this effect.

In addition, only a single detector thickness with two electric field conditions are considered in this study, to provde an initial range of the Swank factor achievable. Additional

detector thicknesses and more biasing conditions can be simulated to provide more details to the detector performance.

Lastly, Swank factor is used as the performance metric for the purpose of this study. However, other image quality metrics such as detective quantum efficiency may be considered. Also, a phantom study may yield optimal performance parameters for the lowest dose absorption in the breast based on incident x-ray spectra, detector thickness and biasing conditions.

Chapter 6

Recombination algorithms and burst models

The problem to determine the probability of recombination for two opposite charge carrier in applied electric field taking into account diffusion has been solved analytically by Onsager[104]. The resulting recombination fraction is a function of the thermalization distance, applied electric field and temperature. In this work, the probability of recombination for electron-hole pairs (or the recombination fraction) is calculated as the ratio between the number of recombined and generated electron-hole pairs.

The recombination fraction for a single electron-hole pair traveling in electric field taking into account drift and diffusion is shown in Fig. 6.1 for the Monte Carlo simulation and analytical Onsager model[104]. The recombination fraction is a function of the thermalization distance, applied electric field, and temperature. As the thermalization distance and electric field increases, the probability of recombination decreases because the effect of the Coulomb attraction is reduced with larger thermalization distance or electric field. Temperature increases can also affect the recombination fraction, because the diffusion process is dependent on temperature. Increased temperature lead to an increase in the diffusion and random motion of individual carriers, thus a lower recombination fraction. The escape efficiency ($\eta_{escape} = 1 - \eta_{recomb}$) for a single electron-hole pair is described by the the Onsager model using the Smoluchowski-type equation[105, 104, 86]:

$$\eta_{escape} = e^{-a-b}\frac{1}{b}\sum_{l=1}^{\infty}(\frac{b}{a})^{l/2}I_l(2\sqrt{ab}) \ , \tag{6.1}$$

where $a = e^2/(4\pi\varepsilon_r\varepsilon_0 r_0 kT)$, $b = eE_{app}r_0/(kT)$, and $I_l(x)$ are modified Bessel functions of the first kind.

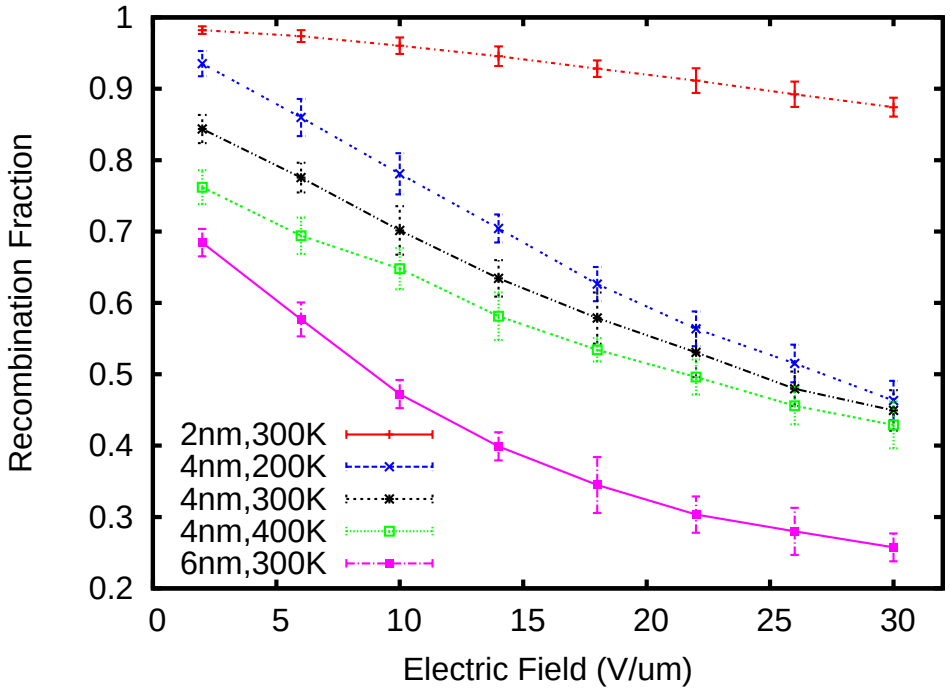

Figure 6.1: Monte Carlo and analytical recombination fraction results as a function of applied electric field for single electron-hole pair transport with initial thermalization distance r_0 of 2, 4 and 6 nm and temperature of 200, 300 and 400 K. The individual points are from Monte Carlo simulations, and the curves are analytical result.

When x rays interact with the semiconductor they deposit energy producing energetic secondary electrons through a variety of mechanisms with energy dependent cross-sections. These energetic electrons lose their energy through a large number of low-energy-transfer events. In turn, the local deposition of energy produces a random distribution of electron-hole pairs called burst. Each burst can have multiple realizations, called clouds, with a random distribution of initial electron-hole pair energies and positions. From Section 3.1, these electron-hole pairs lose their initial kinetic energy in a thermalization process and separated by a finite distance, r_0, defined in Equation 4.1. For the purpose of this analysis, we consider a point burst, i.e., charge carriers initially lying on the surface of a sphere with an effect size (sphere diameter) given by r_{burst}, defined by Equation 4.4. The work in this subsection [10] is centered on the initial processes immediately after burst generation

with regards to the transport and recombination of carriers. Deep trapping is taken into account in the model defined by Equation 4.9, but later processes such charge induction is not considered.

In the simulation code, recombination events are determined at each time step using a recombination algorithm and, for simplicity, ignoring local variations in the field due to the material crystalline structure, i.e., the probability of recombination is modeled as proportional to the distance between recombining carriers. These recombination models are the focus of this subsection. After recombination events are tallied, carrier transport resumes. The mean recombination fraction over many clouds is denoted as the recombination fraction or efficiency (η_{recomb}).

We assume that recombination occurs if carriers are within a recombination distance (d_0) assumed in this work to 1 nm as described in Section 4.2.5. Our first model determines recombined pairs based on minimum distance between the carriers, considering one carrier at a time. We call this the nearest-neighbour model (NN). For a carrier, the distances are calculated for all possible candidates (oppositely charged carriers) and the nearest is marked for recombination leaving the rest of the candidates available for future recombination. A schematic of the model is shown in Figure 6.2(a). Using this model, we investigated the effect of the number electron-hole pairs, applied electric field, and thermalization distance on the recombination efficiency as a function of the surface density (ρ_0) or a cloud is given by $N/[4\pi(d_0/2)^2]$ shown in Figure 6.2(b). The recombination efficiency increases with the large density due to greater availability of carriers for recombination and decreases with increasing electric field which forces holes and electrons to separate toward respective electrodes.

Because the NN model is computationally intensive, we developed an alternative model, the first-hit model (FH). The algorithm consists of looking at the recombination candidate table and selecting the first candidate at a distance less than the recombination distance from the carrier. Once the algorithm finds such a recombining candidate, it identifies the pair as recombined and move on to the next carrier in the list. Figure 6.3 depicts a comparison between the recombination fractions and efficiencies of the two models. Most carriers recombine for the case the thermalization distance and the applied field are low, and the recombination efficiencies for NN and FH are very similar. While for larger thermalization distance and electric field, the recombination efficiencies are uncorrelated, but corresponding recombination efficiencies and standard deviations are similar.

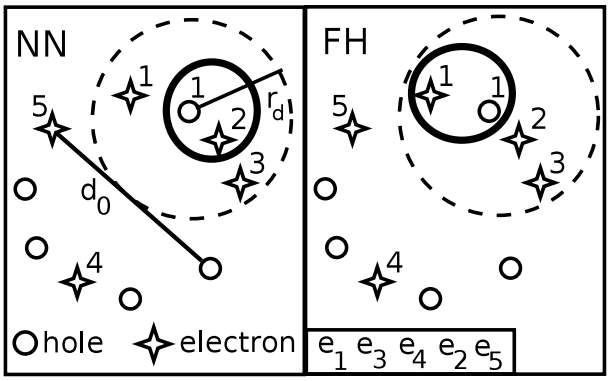

(a)

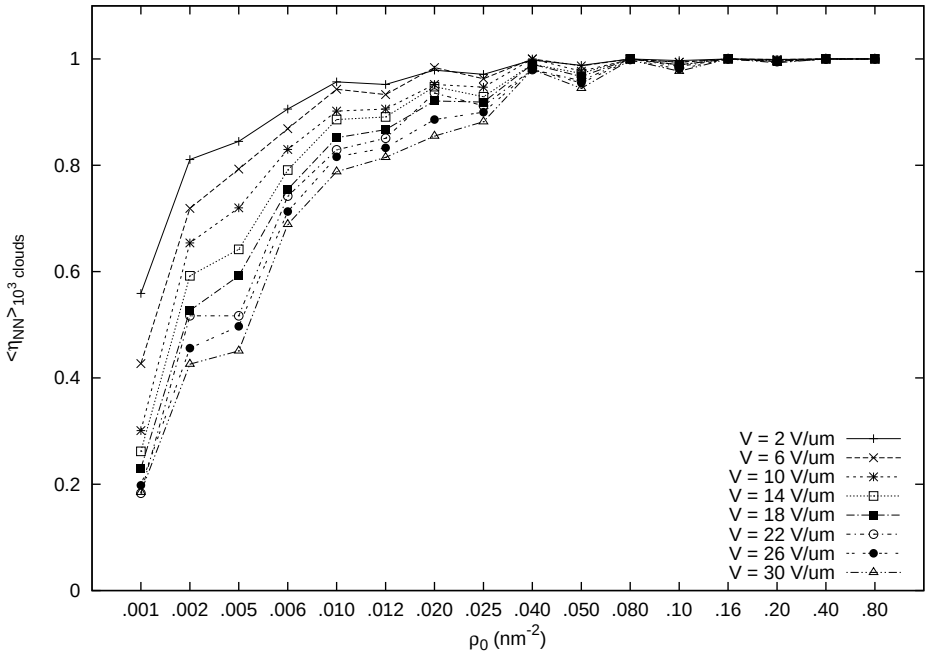

(b)

Figure 6.2: (a) Two-dimensional schematics of recombination models[10]. The dashed line denotes recombination region for hole number one (h_1). Electron table order is shown for the FH model. For NN, h_1 recombines with the nearest electron e_2 while for FH, it recombines with e_1, the first one in the table. (b) Recombination efficiency of the NN model as a function of the burst carrier surface density under different bias conditions (2 to 30 V/μm) for 1000 cloud realizations.

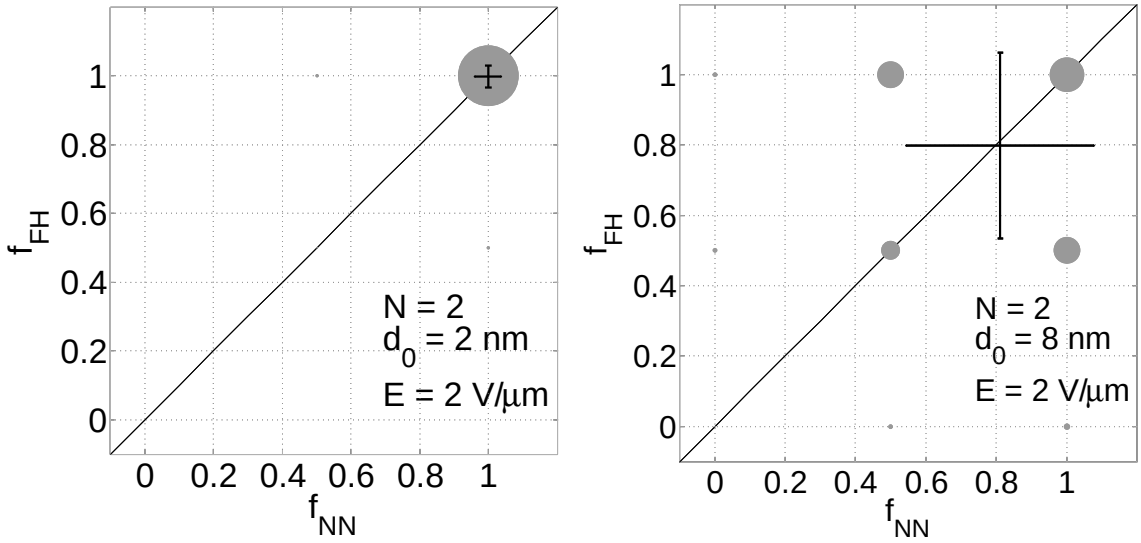

(a)

(b)

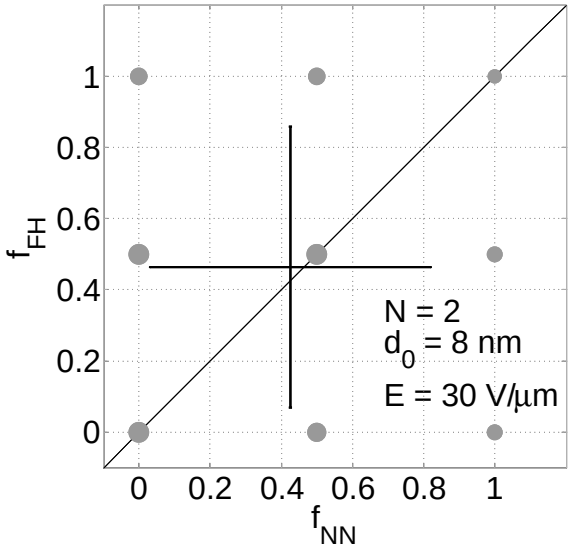

(c)

Figure 6.3: (a) Comparison of recombination results for 1000 cloud realizations[10]. The size of the bubble represents the distribution of f_{FH} and f_{NN} for the 1000 clouds simulated. The recombination efficiency for the two models are shown by the intersection of the black lines with the error bars depicting the standard deviation. For these figures, number of electron-hole pairs, $N = 2$ (a) $d_0 = 2nm$ and $E_{app} = 2V/\mu m$, (b) $d_0 = 8nm$ and $E_{app} = 2V/\mu m$, (c) $d_0 = 8nm$ and $E_{app} = 30V/\mu m$.

6.1 Clinical spectral input

Two algorithms are studied in this work for finding suitable candidates to recombine[106]. When carriers locations and characteristics are stored in an array, the FH algorithm recombines the first pair of electron-hole pairs found to be within the recombination distance, while the NN algorithm searches through the entire array and recombine the pair closest to each other. The NN algorithm is more computationally intensive and provides a more realistic model that gives a chance to allow for electrons and holes within the recombination sphere yet near the edge a chance to escape recombination.

The simulated PHS for both radiation qualities are shown in the Figure 6.4 and 6.5. Figure 6.4 shows the PHS for transport at 4 and 30 V/μm applied electric field with the FH and NN models for Mo spectra, and Figure 6.5 for the W spectra.

Table 6.1 lists the Swank factors and recombination fractions with the two recombination algorithms for the molybdenum and tungsten spectra. The total simulation time is reported for ten million incident x-ray photons. Both the Swank noise and recombination results agree well between the FH and NN algorithm, while the simulation time increases for lower applied bias because electron-hole pairs take more time to separate and therefore, recombination is more likely to occur. Simulation times change by about 25% for FH compared to NN model.

Table 6.1: Simulated Swank factor and recombination fraction for Mo/Mo (RQA-M 2) and W/Al standard radiation qualities with varying transport conditions.

Radiation Quality (IEC 61267)		4V/μm FH	4V/μm NN	30V/μm FH	30V/μm NN
Mo/Mo (RQA-M 2)	$I(E)$	0.878	0.878	0.922	0.922
	f_R	96.5%	96.5%	80.0%	80.1%
	Time (s)	1.18×10^7	1.51×10^7	7.75×10^6	8.66×10^6
W/Al	$I(E)$	0.903	0.904	0.937	0.937
	f_R	96.5%	96.4%	79.6%	80.1%
	Time (s)	1.38×10^7	1.80×10^7	9.29×10^6	1.03×10^7

The simulation model consists of a 150 μm thick a-Se detector with a pencil beam source. Both burst models (surface versus volume) and two recombination algorithms (FH versus NN) are considered in this study. The probability of recombination for electron-hole pairs, recombination efficiency, f_R, is calculated as the ratio between the number of recombined and generated electron-hole pairs.

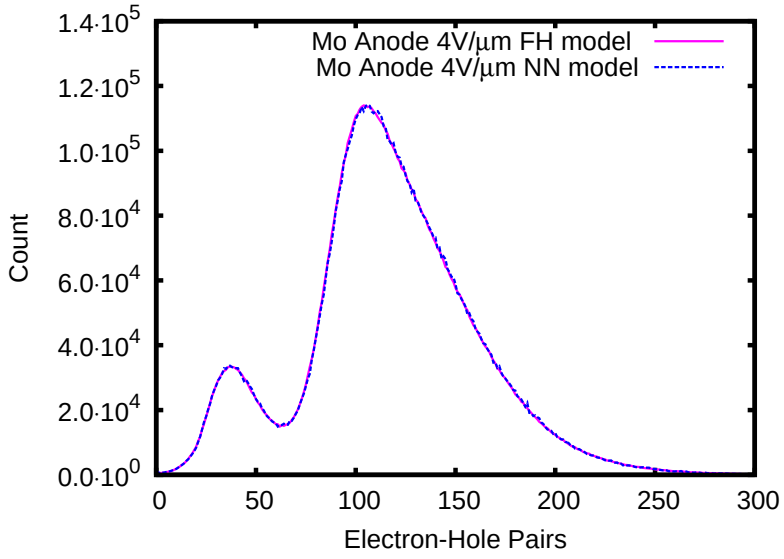

(a)

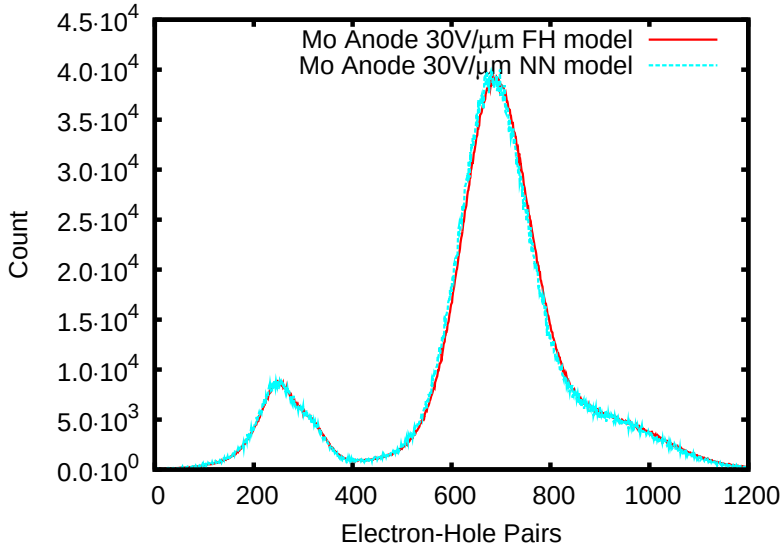

(b)

Figure 6.4: (a) Simulated PHS with molybdenum mammography spectrum as a function of electron-hole pair transport for 4 V/μm applied electric field using FH and NN recombination algorithms. (b) Simulated PHS with molybdenum mammography spectrum as a function of electron-hole pair transport for 30 V/μm applied electric field using FH and NN recombination algorithms.

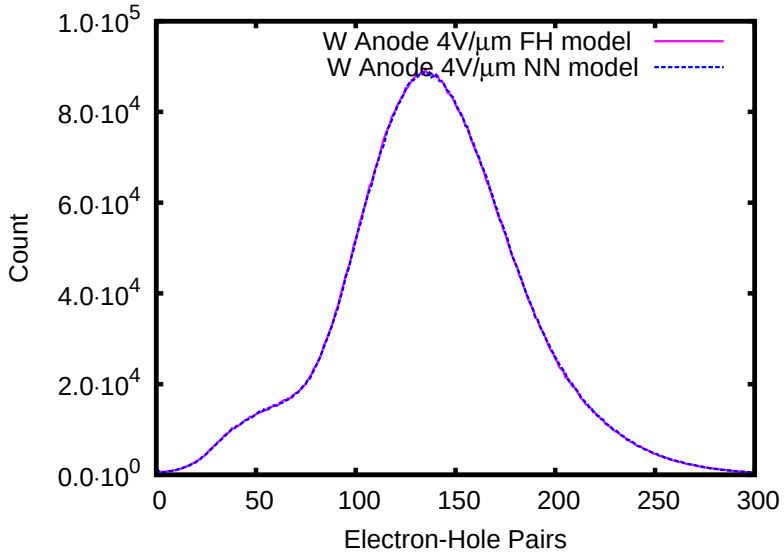

(a)

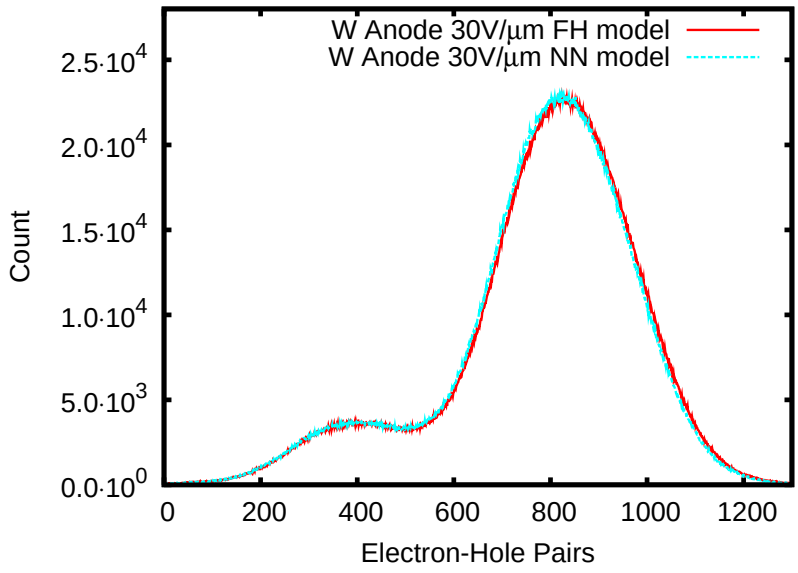

(b)

Figure 6.5: (a) Simulated PHS with tungsten mammography spectrum as a function of electron-hole pair transport for 4 V/μm applied electric field using FH and NN recombination algorithms. (b) Simulated PHS with molybdenum mammography spectrum as a function of electron-hole pair transport for 30 V/μm applied electric field using FH and NN recombination algorithms.

6.2 Burst models

The concept of a burst defined by Equation 4.4 is introduced in conjunction with the thermalization of carriers, as an extension to our previous work on recombination models based only on r_0 [84], in order to provide a three-dimensional distribution model for electron-hole pair generation. Two burst models using these parameters are examined for the generation of electron-hole pairs [107]. For the spherical surface area (SSA) model, the sites of initialization for an individual electron-hole pair is sampled isotropically on the burst surface, then the electron-hole pair is separated by the thermalization distance, r_0, defined by Equation 4.1. For the spherical uniform volume (SUV) model, the sites of initialization for individual electron-hole pairs are sampled uniformly in 3D within the spherical burst volume as shown in Figure 6.6.

The pulse-height spectra for 10, 13, 40 and 140 keV with carrier transport at 4 and 30 V/μm applied electric field for the calculation of Swank noise and recombination fraction are shown in Fig. 6.7. For 13 keV monoenergetic x rays, a sharp drop in Swank noise is observed due to the escape of fluorescent x-ray photons generated at energies above the K-edge energy (12.6keV) of a-Se. From Fig. 6.7(b), the Swank noise increases as the incident photon energy increases from the Se K-edge (12.6 keV) to approximately 40 keV. Above this energy, for example 140 keV, the Compton effect dominates and low energy deposition events degrades the detector performance. From 6.7(a), the carrier recombination fraction in general decrease with incident x-ray energy, due to higher number and concentration of eletron-hole pairs created from the larger energy deposition in the detector. A slight increase in recombination fraction is observed for the 13 keV case, due to reabsorption of fluorescent x-ray photons generating small bursts of charges relatively far away from the initial site of interaction.

From Fig. 6.7, the choice of FH or NN recombination model does not affect the Swank and recombination simulation for realistic diagnostic x-ray energy range. The SSA model exhibits a larger difference in Swank noise between the 4 and 30 V/μm biasing conditions, largely due to closely packed carriers within the burst surface increasing the probability of recombination. The SSA model distributes carriers much closely packed compared to the SUV model, where an increase in the applied electric field can greatly decrease the recombination efficiency while increasing the Swank noise.

This work improves on the previous charge generation model[10]. Realistic incident x-ray energies in the diagnostic range are used to include the stochastic nature of x-ray particle transport. For simulation of x rays with a point burst model, where the r_{burst} defined by Equation 4.4 is set to zero, charge carrier generated are much more probable

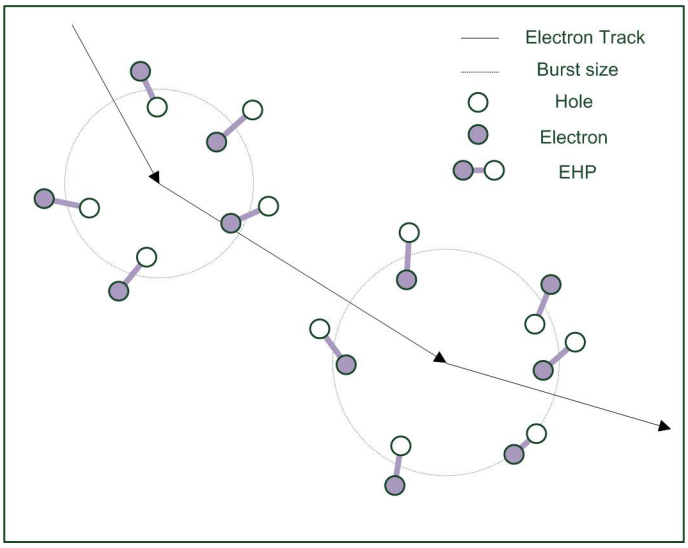

(a)

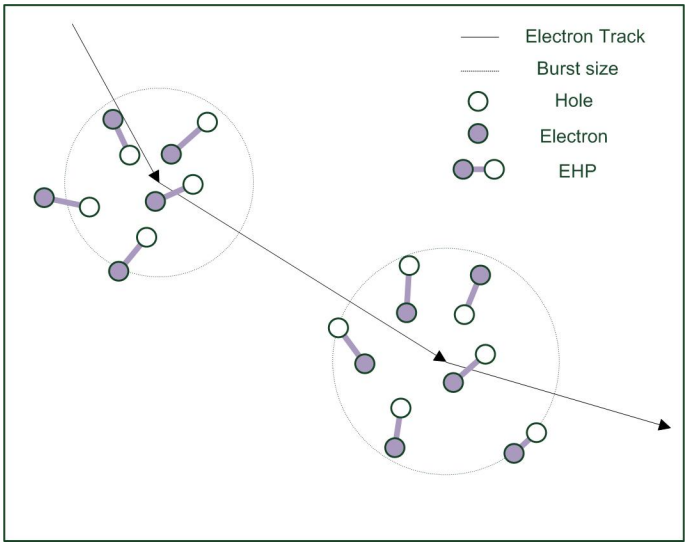

(b)

Figure 6.6: (a) Illustration of the surface burst model with electron-hole pairs initialized spherically on the surface area (SSA). (b) Illustration of the volume burst model with electron-hole pairs initialized uniformly in the burst volume (SUV).

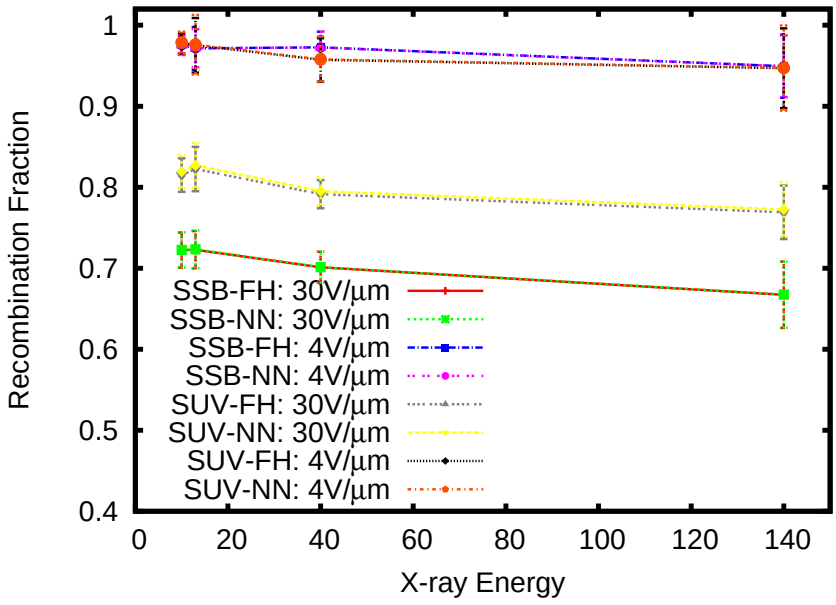

(a)

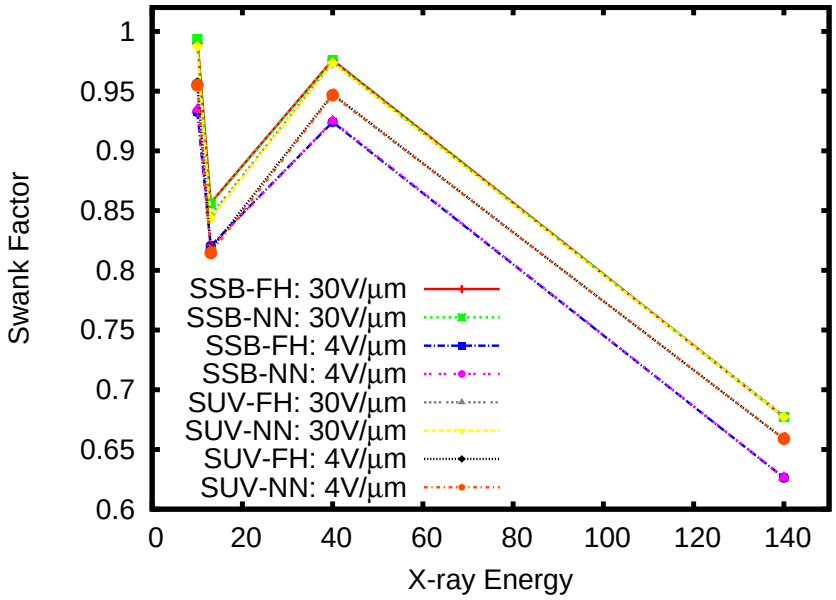

(b)

Figure 6.7: (a) Simulated recombination fraction as a function of incident photon energy for the SSA and SUV models. (b) Simulated Swank noise as a function of incident photon energy for the SSA and SUV models.

to recombination due to higher concentration of carriers not realistic for the a-Se detector. For example the recombination fraction without considering the burst model, for 10 keV photons is in the range of 0.95 to 0.99 for 30 and 4 V/μm applied bias, respectively.

The recombination fraction is greatly affected by carrier mobility as shown in Equation 4.7. In semiconductor materials, the mobility of individual carriers may vary greatly depending on the fabrication process, material properties and imperfections. In addition, different carrier types in the same material can exhibit varying mobilities and the distance traveled by each carrier, caculated from Equation 4.8 can be different. For example, in a-Se, the speed of holes is found to be up to 40 times faster than electrons[28]. This difference in carrier mobility, with trapping and detrapping of carriers, can lead to artifacts including lag and ghosting. Since an x-ray photon can create many electrons and holes, two effective mobilities are used to model the two types of carriers in a-Se. Experimentally, the effective mobility of a carrier can be determined using time-of-flight measurements, where a short pulse of strongly absorbed radiation[58] or a high-power laser is used to create carriers on the semiconductor top surface and the signal detection and transit times are averaged. Several electron and hole mobilities have been used previously for a-Se[86, 76, 84, 19], and a range of carrier mobility parameters can be used to explore the consistency of simulation results. In our model, the variability in carrier mobility can also be taken into account by sampling from a range of carrier mobilities.

A voltage source is often used with semiconductor x-ray detectors to provide the applied bias required for carrier separation. In a-Se, the typical biasing condition is 10 V/μm, so for a mammography detector with a thickness of 200 μm, a voltage source of 2 kV is needed. For thicker detectors, even higher voltages are used, thus cooling and temperature variation effects become important. Since the carrier mobility is a function of temperature, the effect of temperature on the Swank noise, burst and recombination models can be studied. In our model, a constant temperature of 300 K is used. The temperature variance for different pixel and thickness can be implemented in the future to model this dependence.

Chapter 7

Spatial resolution

Detectability of microcalcifications and small lesions in mammography has driven the development of high spatial resolution imagers with small pixel pitch[108, 109]. However, effects such as charge sharing and readout noise lead to the fundamental detector resolution limits[110, 111, 110, 112]. In this work, we study the detector spatial resolution of prototype a-Se flat-panel imagers through experimental measurements and Monte Carlo simulations[113].

The detective quantum efficiency (DQE) is an important detector performance metric, and a measure of the combined effects of signal and noise performance of an imaging system, expressed as a function of x-ray energy and spatial frequency. DQE can be expressed in terms of the signal-to-noise ratios (SNR) at input and output shown in the following equations[110, 114]:

$$SNR_{in}^2(k) = \overline{q} \ , \tag{7.1}$$

$$SNR_{out}^2(k) = \frac{\overline{q}^2 \overline{G}^2 MTF^2(k)}{NPS(k)} \ , \tag{7.2}$$

$$DQE(k) = \frac{SNR_{out}^2(k)}{SNR_{in}^2(k)} = \frac{\overline{q}^2 \overline{G}^2 MTF^2(k)}{NPS(k)} = \frac{MTF^2(k)}{NNPS(k)} = \frac{NEQ(k)}{\overline{q}} \ , \tag{7.3}$$

where $\overline{q}$ is the mean number of incident x-ray quanta per unit area, $\overline{G}$ is the mean detector gain relating $\overline{q}$ to the average zero-mean pixel value. MTF(k) is the modulation transfer function , and NPS is the image noise power spectrum, and the NNPS is normalized noise power spectra. The initial application of DQE in medical imaging was for x-ray film-screen

systems[115, 116], and image quality (in terms of the signal-to-noise ratio) can be expressed in terms of the noise-equivalent quanta (NEQ). The NEQ describes the minimum number of x-ray quanta required to produce a specific SNR.

Figure 7.1 shows the cross-sectional view of the prototype a-Se flat-panel detector (FPD) used. The FPD is positively biased, with a polymer layer inserted between the a-Se photoconductive layer and the electron-transporting layer. The polymer is coated uniformly from a solution mixture of the insulating polymer and C_{60} and an aromatic solvent. A hole-transporting layer, the a-Se layer, the electron-transporting layer, and the top gold electrode were formed by vacuum vapor deposition. Only the C_{60}-doped polymer layer was formed by wet process[117].

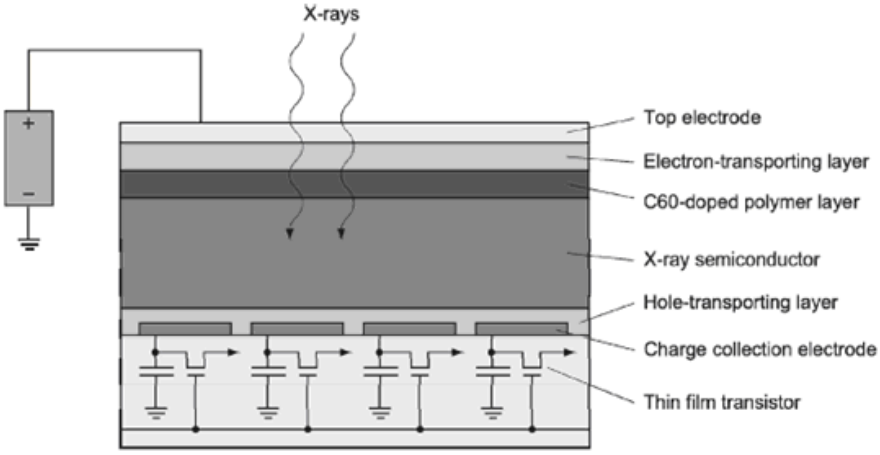

Figure 7.1: Cross-sectional view of layered structure for an a-Se-based x-ray detector with C_{60}-doped polymer layer. This detector consists of the following components: a top electrode with a positive voltage bias, an inorganic electron-transporting layer, a C_{60}-doped polymer layer, a thick a-Se layer for photoelectric conversion of x-ray photons, an inorganic hole-transporting layer, an a-Si TFT substrate for readout.

Table 7.1: Characteristics of the prototype flat-panel detector.

Detector material	a-Se, 240 and 1000 μm
Pixel pitch	150 μm
Array size	2880x2880
Imaging area	43x43cm^2

Table 7.1 outlines the characteristic of the prototype FPDs. Two a-Se detectors with

different thicknesses, 240 and 1000 μm are studied. Beside the difference in thickness, the detectors have the identical imaging area and pixel size. The active imaging area is 43x43 cm^2, and the pixel pitch is 150 μm. This detector configuration lead to an array size of 2880 by 2880 pixels. The thinner 240 μm detector is intended for mammography applications and the thicker 1000 μm for general radiography. Both prototype detectors also shared the layered structure shown in Figure 7.1 with the C_{60} polymer. This polymer layer is intended to act as capsulation for a-Se to prevent crystallization and improve detector performance. In conventional a-Se detectors, crystallization in the amorphous layer can occur from non-uniformities and arcing due the high applied bias leading to loss in resolution and performance. The crystallization process is further accelerated from an increase in temperature. The C_{60} polymer layer have been shown to prevent crystallization in a-Se films, and thus used in the prototype detectors for this study. Additional information on the C_{60} polymer layer are included in the Appendix section.

7.1 Experimental measurement

Experimental procedures outlined in the International Electrotechnical Commission standards documents, IEC-61267[102] and IEC-62220-1[11] were followed for the experimental measurements. The IEC-61267[102] describes the RQA beam qualities used in the study. The radiation qualities have a range of parameters depending on the x-ray tube voltage, and additional aluminum filtration listed in Table 7.2. The RQA radiation qualities are used to standardize the x-ray input used for measurement of modulation transfer function and noise power spectrum. Different x-ray tube energies can be used to represent a range of applications, while the half-value layer (HVL) data can be used to verify changes in the x-ray beam intensity at specific filter thicknesses.

Table 7.2: Radiation quality for the determination of detective quantum efficiency and corresponding parameters.

Radiation quality	Approx. x-ray tube voltage (kV)	Half-value layer (HVL) mm Al	Additional filtration mm Al
RQA3	50	4.0	10.0
RQA5	70	7.1	21.0
RQA7	90	9.1	30.0
RQA9	120	11.5	40.0

Figure 7.2 shows the generated RQA radiation beam qualities based on parameters from Table 7.2. The maximum x-ray energy correspond to the x-ray tube voltage for all

RQA qualities. RQA3 has the lowest tube voltage with a maximum x-ray energy is 50 keV, and RQA9 has the highest voltage and x-rays with maximum energy of 120 keV. For tube voltage greater than 60 keV, additional characteristic peaks are observed in the input x-ray spectrum near 59 and 68 keV, corresponding to the fluorescent energies of the tungsten anode.

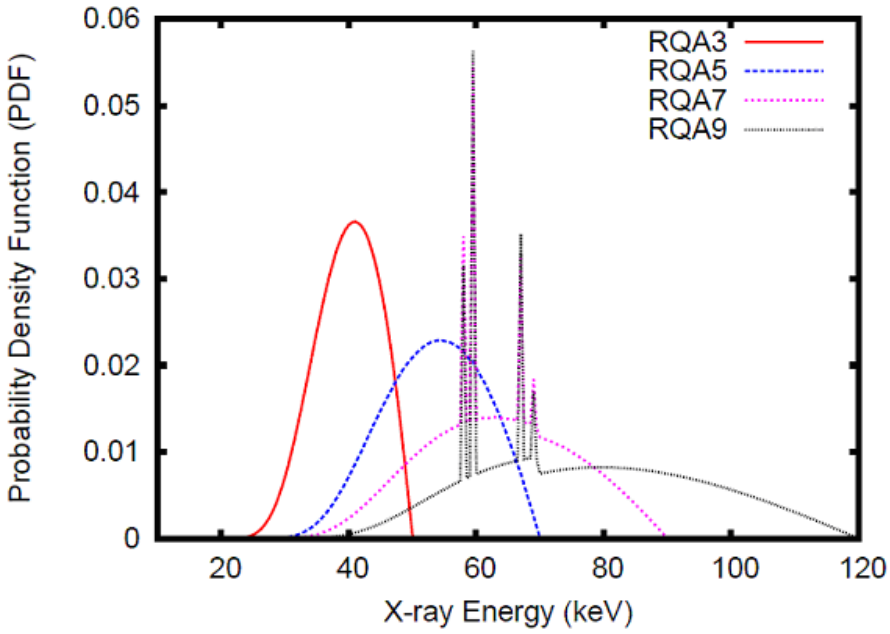

Figure 7.2: RQA beam qualities used in the image quality measurements.

The IEC-62220-1[11] outlines the experimental setup and procedures for measurement of MTF and NPS. Figure 7.3, shows the experimental setup used for MTF measurements. X rays are shot from the tube anode passing through collimation (B1) and impinges onto the detector surface. Added filters are used in combination with different tube voltages to achieve the different RQA beam qualities. Two additional diaphragms (B2 and B3) can be used to further collimate the beam. The test device used in this study is an edge phantom made from tungsten placed above the prototype a-Se detector for MTF measurements. The image produced by the edge phantom can be used to generate an edge spread function (ESF). The MTF can be calculated by taking the Fourier transform of the derivative of the ESF[11].

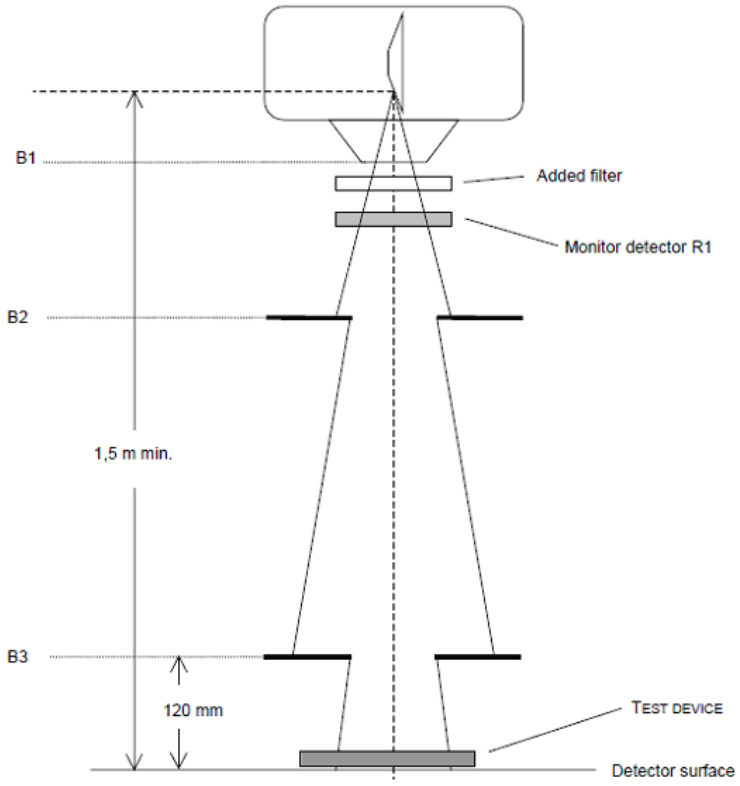

Figure 7.3: Geometry of exposing the digital x-ray imaging device in order to determine the modulation transfer function. The tube anode must be at least 1.5 meters away from the detector surface. B1, B2 and B3 represent the materials used to collimate the x-ray beam. The test device (edge phantom) is placed above the detector surface[11].

7.1.1 Modulation transfer function

Figure 7.4 and 7.5 show the measured MTF for the 1000 μm detector plotted as a function of spatial frequency. In general, the MTF is a function of applied bias and spatial frequency. As the spatial frequency increases, MTF decreases because the task to resolve smaller objects becomes more and more difficult. In general, the MTF is also a function of the detector applied bias. An increase in applied electric field improve the carrier transport statistics and results in a higher measured MTF.

From Figure 7.4 and 7.5, the MTF is highest for the 10 V/μm case. Compared to the high detector bias case, MTF is significantly degraded for high spatial frequencies espe-

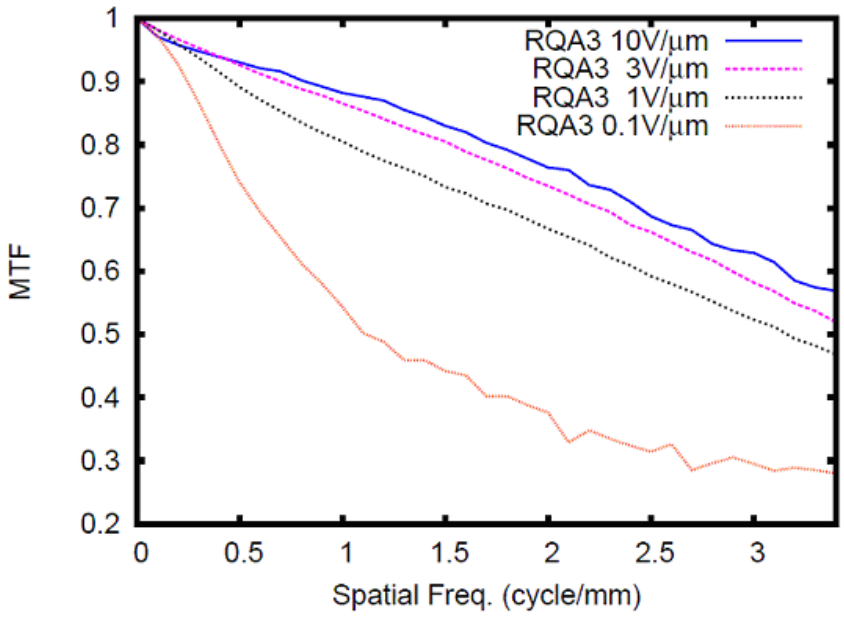

(a)

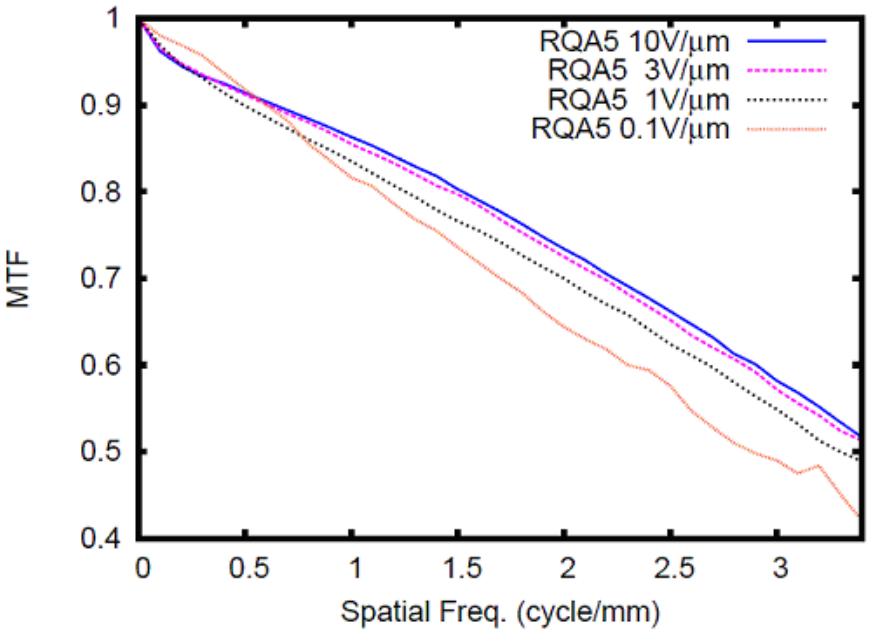

(b)

Figure 7.4: (a) Measured MTF for 1000 μm a-Se detector as a function of applied electric field and spatial frequency with RQA3. The applied electric field is 0.1, 1, 3 and 10 V/μm. (b) For RQA5.

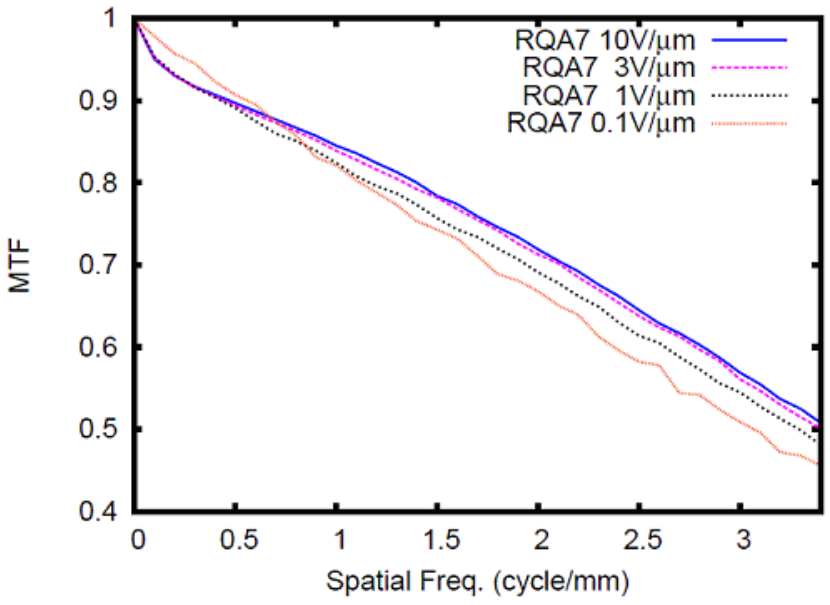

(a)

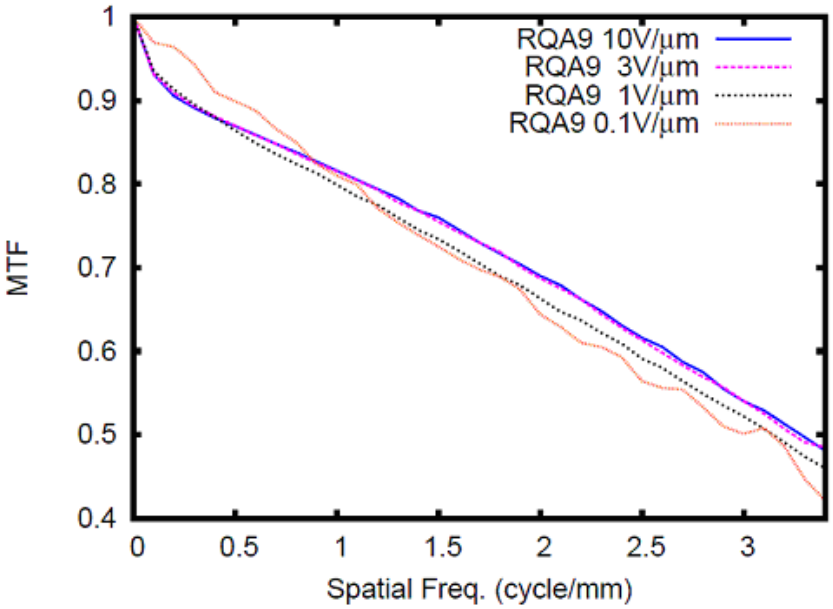

(b)

Figure 7.5: (a) Measured MTF for 1000 μm a-Se detector as a function of applied electric field and spatial frequency with RQA7. The applied electric field is 0.1, 1, 3 and 10 V/μm. (b) For RQA9.

cially when the electric field is reduced to 0.1 V/μm. This degradation in performance is most prominent for the RQA3 beam quality as shown Figure 7.4(a). The reason for this decrease in MTF can be due to the high absorption efficiency and low energy of the incident photons. Figure 7.2 shows that RQA3 has the lowest energy distribution of incident photons compared to other radiation qualities. Since the detector thickness is constant, lower photon energy result in a highest absorption probability. When the applied electric field is reduced, the number of electron-hole pairs that recombine or get trapped increases, causing a reduction in the detector sensitivity. Since RQA3 with the lowest energy distribution should have relatively the highest performance and absorption probability, this loss in sensitivity is most prominent. As the x-ray energy distribution increases for RQA5, RQA7 and RQA9, shown in Figure 7.4(b) and Figure 7.5, a small difference in MTF is observed. Additionally, spatial degradation can be caused by generation and re-absorption of characteristic x rays, spreading due to Compton scattering and high-energy secondary electron transport. As the x-ray energy increases, these effects increase as well, reducing the effect of drift and diffusion of electron-hole pairs under the applied external electric field.

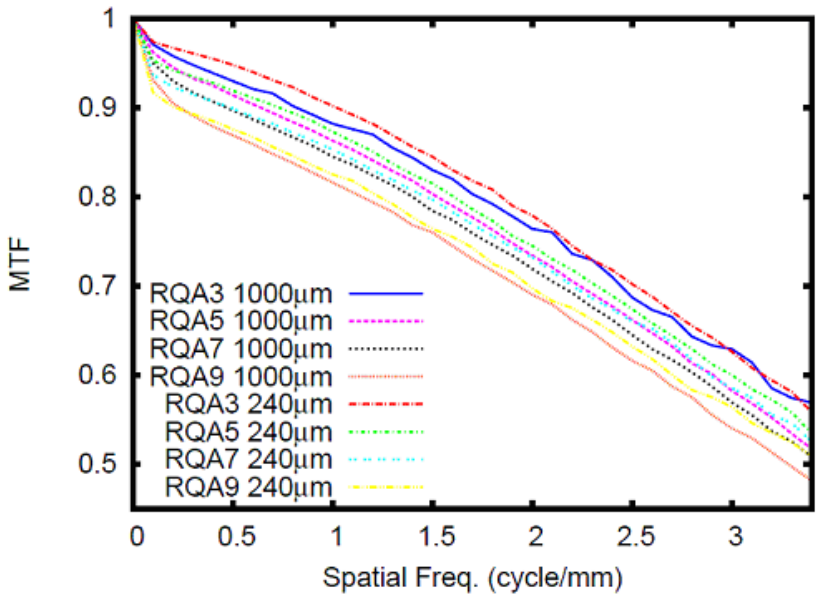

Figure 7.6: Comparison of the MTF for 240 and 1000 μm thick a-Se detectors at 10 V/μm.

Figure 7.6 shows the inter-comparison of MTF performance for a 240 and 1000 μm a-Se detector at 10 V/μm applied bias. In general, the MTF performance for the 240 μm

detector is better than the 1000 μm detector. This is because for the thinner 240 μm thick detector, the distance of each carrier must travel is reduced, compared to the thicker 1000 μm case. Thus the spatial degradation due the electron-hole pair transport is reduced, resulting in a higher MTF. The MTF also depend on the x-ray photon energy. When the x-ray energy increase, the spatial resolution decreases resulting in a decrease in the MTF.

7.1.2 Normalized noise power spectra

The noise power spectrum (NPS) is measured for the same radiation qualities without the test object. The normalized NPS is calculated by dividing the output image of the detector exposed area into square areas called regions-of-interest (ROIs). According to the IEC guidelines[11], each ROI consist of 256 by 256 pixels in size, and can overlap by 128 pixels in both, the horizontal and vertical direction shown in Figure 7.7. From the figure, the value of n is 256.

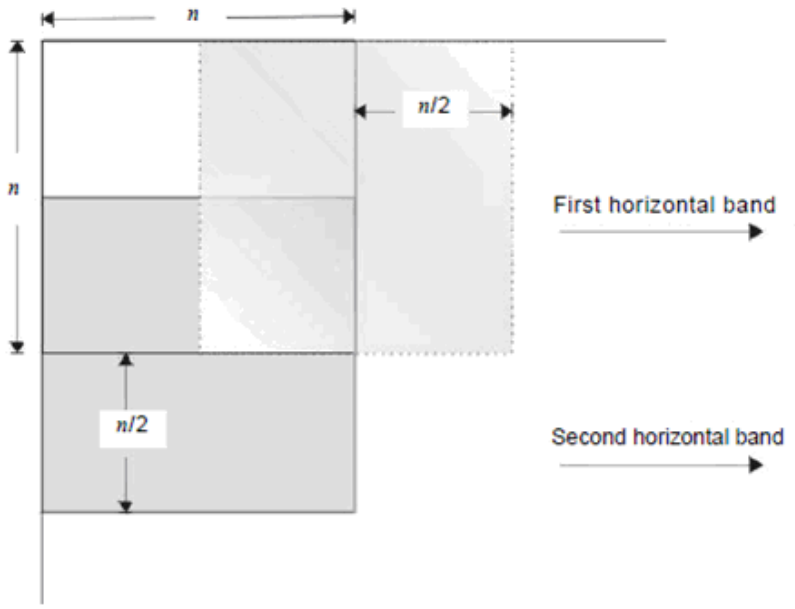

Figure 7.7: Geometric arrangement of the region-of-interest (ROI) used in NPS measurements[11].

The NNPS is a dimensionless quantity calculated from normalizing NPS with Equation 7.3. The NNPS plots for the 1000 μm thick a-Se detector are shown in Figure 7.8 and 7.9.

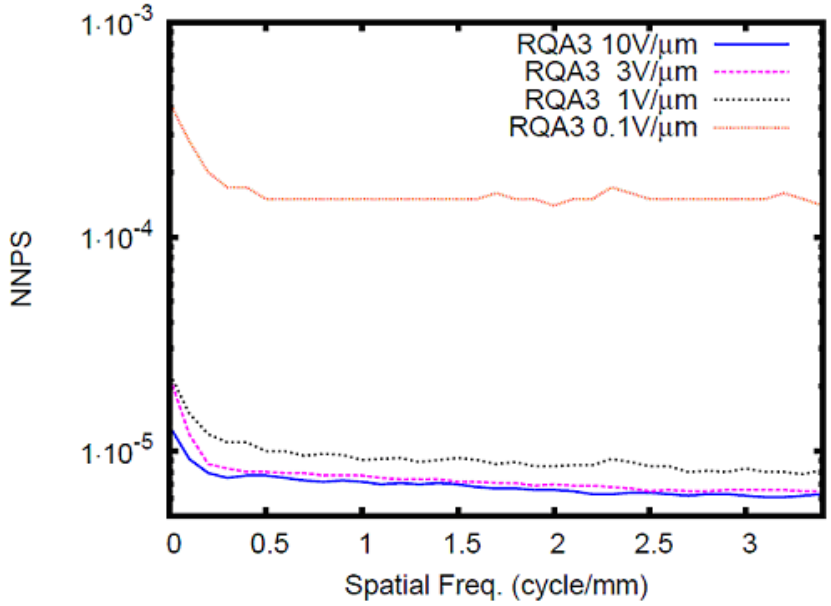

(a)

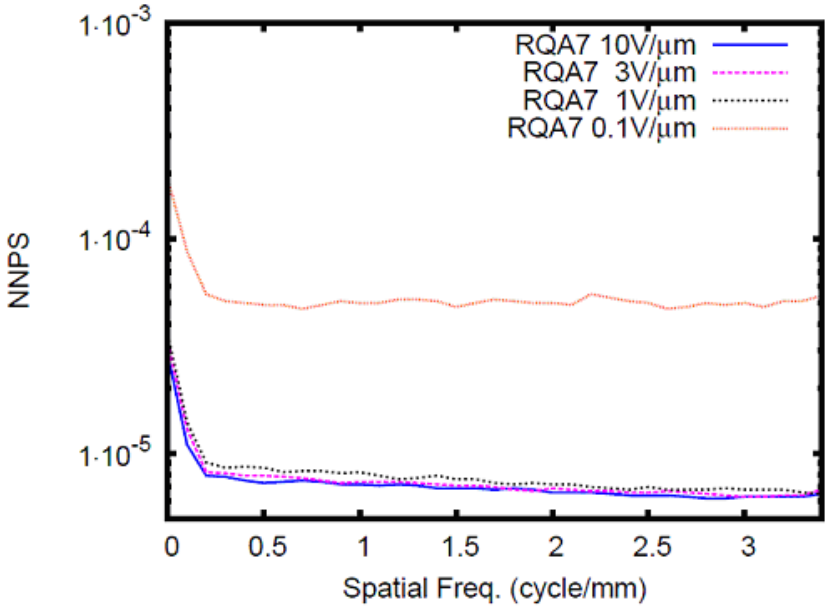

(b)

Figure 7.8: (a) Measured NNPS for 1000 μm a-Se detector as a function of applied electric field and spatial frequency with RQA3. The applied electric field is 0.1, 1, 3 and 10 V/μm. (b) For RQA5.

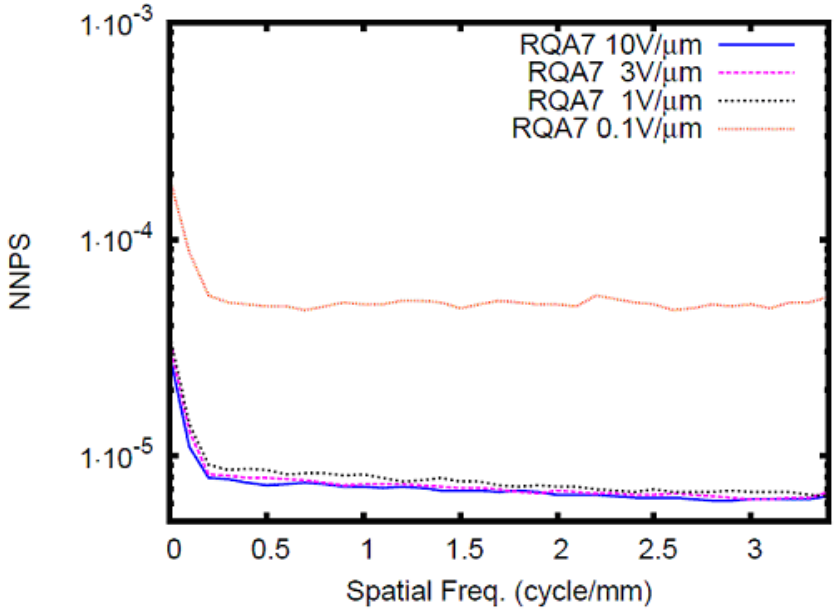

(a)

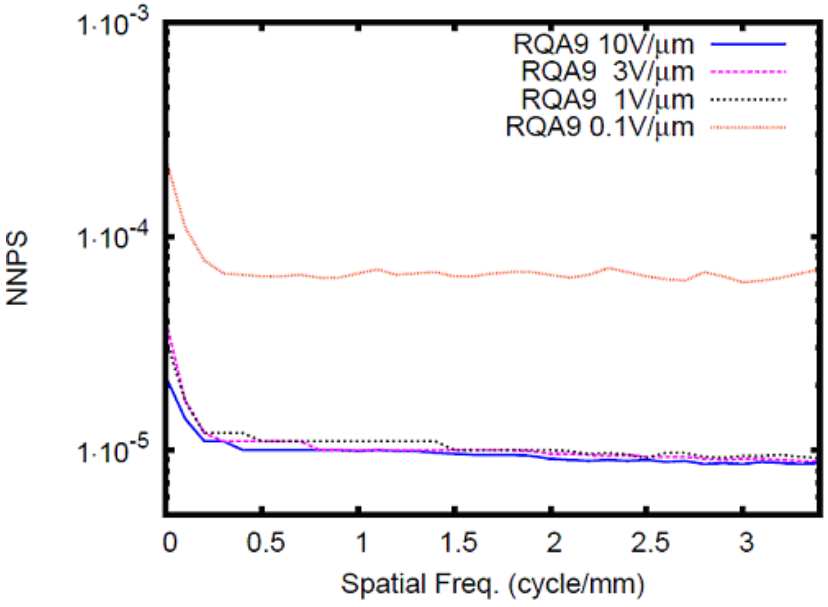

(b)

Figure 7.9: (a) Measured NNPS for 1000 μm a-Se detector as a function of applied electric field and spatial frequency with RQA7. The applied electric field is 0.1, 1, 3 and 10 V/μm. (b) For RQA9.

From these plots, NNPS is a function of electric field and spatial frequency. The NNPS is especially high for a low applied bias compared to higher applied electric field conditions. When the electric field increases, the signal transport in a-Se is improved and more carrier are detected. This improvement in sensitivity may be one of the reasons for the reduction in NNPS as the electric field increases. The NNPS is fairly consistent for spatial frequency between 0.5 to 3 lp/mm.

Figure 7.10 shows the inter-comparison of MTF performance for a 240 and 1000 μm a-Se detector at 10 V/μm. When the applied field is constant, the NNPS is shown to depend on the detector thickness and incident x-ray energy. In general, the thicker 1000 μm detector have lower NNPS compared to the thinner 240 μm detector. Also, as the x-ray energy increased, the NNPS levels increased. This increase in the NNPS as a function of x-ray energy can be due to the degradation in the spatial resolution due to Compton scattering, especially for RQA9.

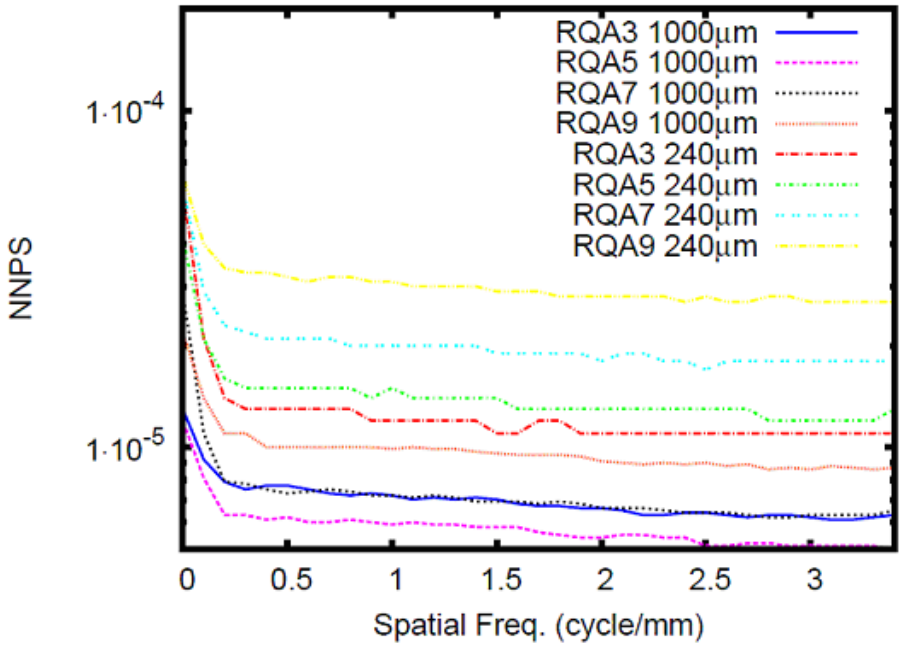

Figure 7.10: Comparison of NNPS for 240 and 1000 μm thick a-Se detectors.

7.1.3 Detective quantum efficiency

The DQE results are calculated from measured MTF and NNPS using the mean number of incident x-ray quanta per unit area, given in Table 7.3. This value is calculated both for per roentgen (R) and SI unit in gray (Gy).

Table 7.3: Parameters used for calculation of DQE.

Radiation quality	SNR_{in}^2 $1/(mm^2 \mu Gy)$	SNR_{in}^2 $1/(mm^2 \mu R)$
RQA3	21759	190870
RQA5	30174	264686
RQA7	32362	283879
RQA9	31007	272607

Figure 7.11 and 7.12 show the DQE results for the 1000 μm detector for a range of applied electric field. The measured DQE is a function of spatial frequency and applied electric field. For a low applied bias of 0.1 V/μm, the DQE is the lowest compared to the 10 V/μm case. A detector with low applied bias would have a comparatively low sensitivty in the detected signal levels. In turn, the low sensitivity would cause a reduction in MTF at high spatial frequency, and higher noise values. Thus, a higher electric would both yield a higher MTF and a lower NNPS, from Equation 7.2 resulting in a higher DQE measurement.

Figure 7.13 shows the inter-comparison of the DQE performance for a 240 and 1000 μm a-Se detector at 10 V/μm, where the DQE is shown to depend both on the incident x-ray energy and the detector thickness. When the detector thickness is reduced, the absorption probability of incident x-rays decreases, causing a reducing in the DQE. This is why the thicker 1000 μm detector has higher DQE than the thinner 240 μm detector. When the incident x-ray energy is increased, charge clouds created by the incident x-rays increase as well, leading to a decrease in the spatial resolution. Thus, the DQE decreases as the energy of the incident x-ray spectrum increases.

In summary, the MTF, NNPS and DQE are measured for two prototype a-Se detectors with thickness of 240 and 1000 μm. These measurements show that the spatial resolution characteristics of a-Se detectors are dependent on the electric field, thickness and spatial frequency.

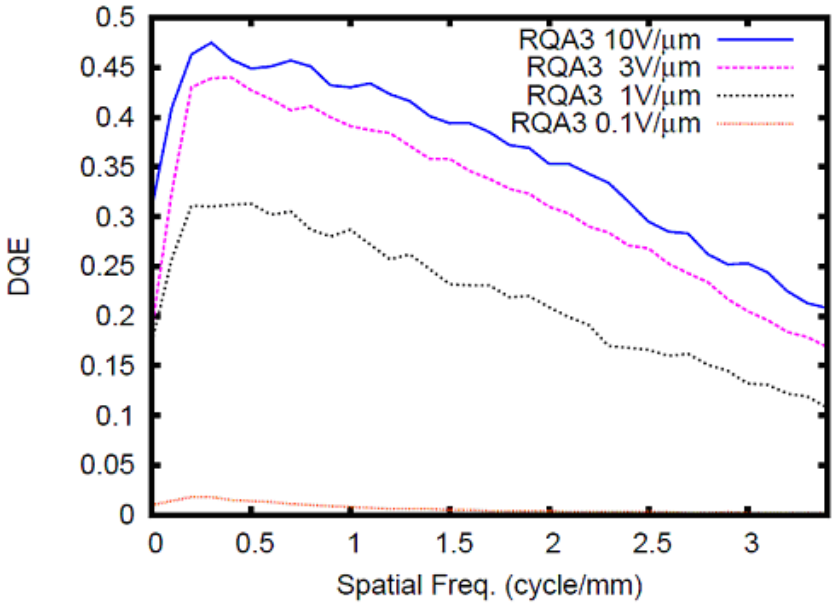

(a)

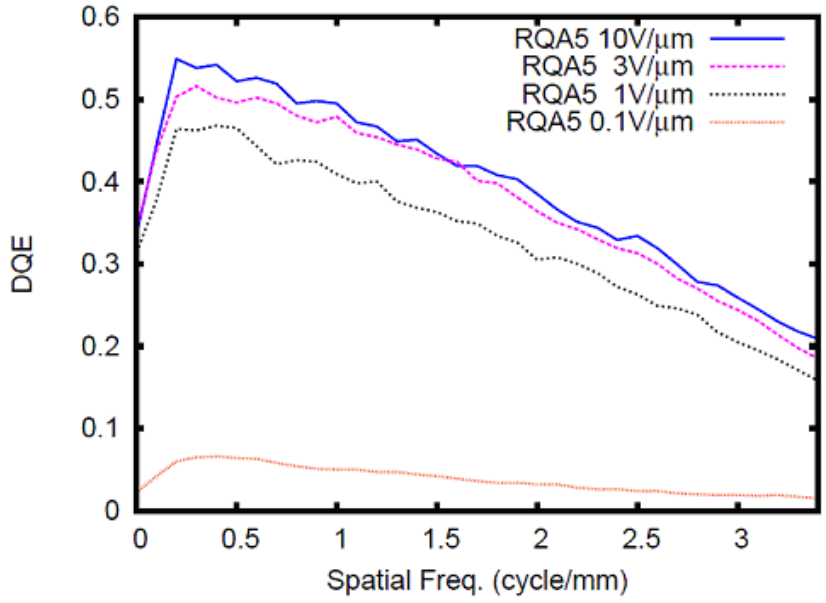

(b)

Figure 7.11: (a) Measured DQE for 1000 μm a-Se detector as a function of applied electric field and spatial frequency with RQA3. The applied electric field is 0.1, 1, 3 and 10 V/μm. (b) For RQA5.

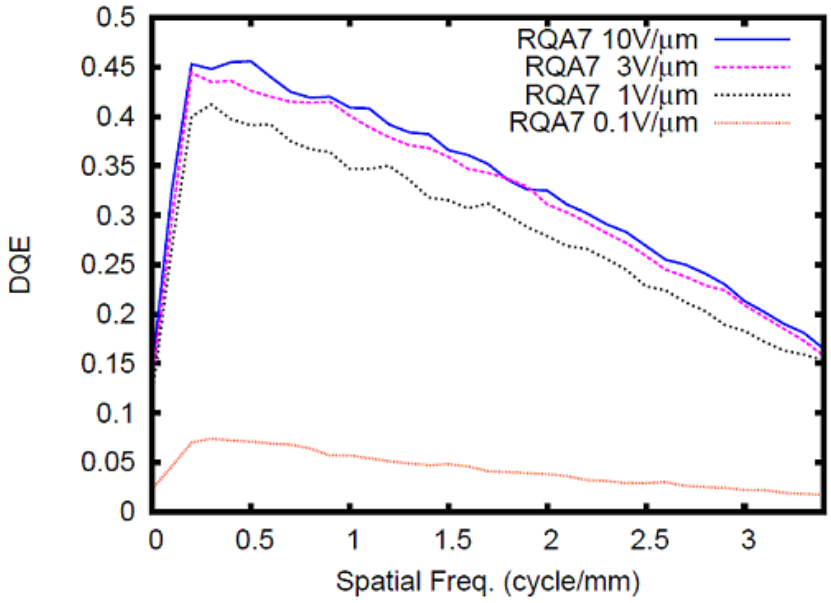

(a)

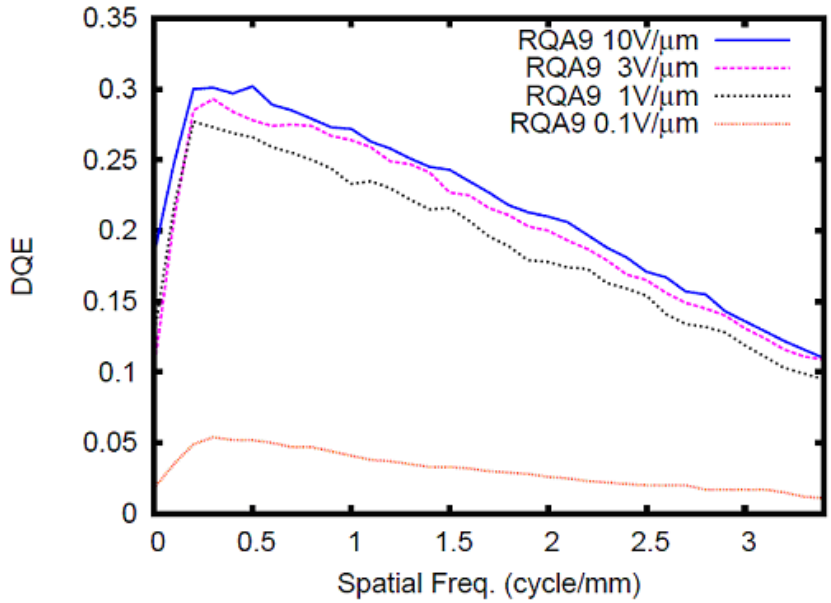

(b)

Figure 7.12: (a) Measured DQE for 1000 μm a-Se detector as a function of applied electric field and spatial frequency with RQA7. The applied electric field is 0.1, 1, 3 and 10 V/μm. (b) For RQA9.

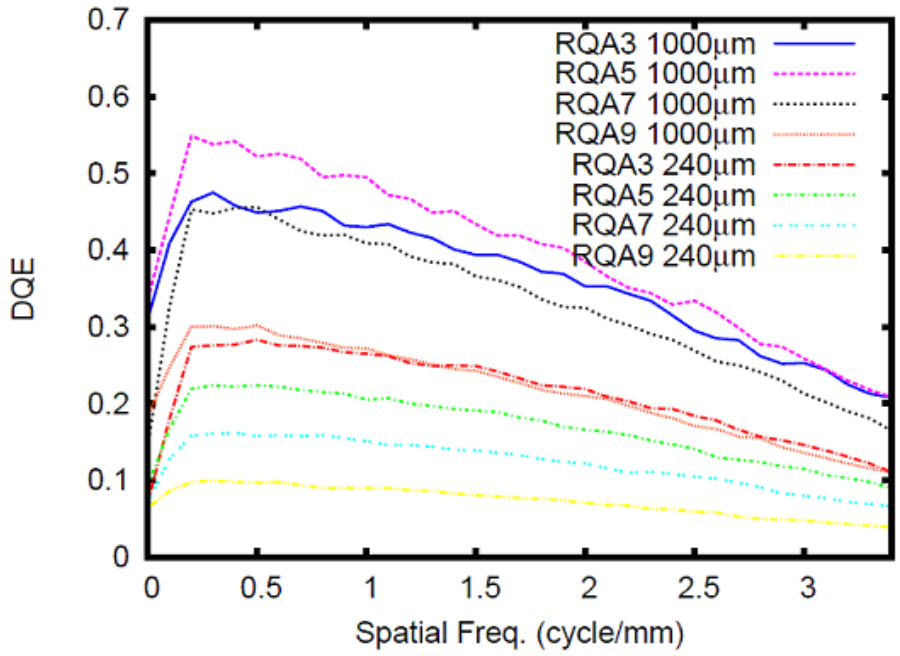

Figure 7.13: Comparison of DQE for 240 and 1000 μm thick a-Se detectors.

7.2 Modeling spatial resolution

7.2.1 Point response function and monoenergetic input

The spatial domain simply refers to the two spatial dimensions of an image, for example the x and y directions. When the detector is stimulated with a single point input, the image produced by the detector is called a point spread function (PSF) or a point response function (PRF). The main focus in Chapter 4 was the amount of charge signal output of a-Se detectors. The ARTEMIS code was extended to allow for spatial output that generates images to x-ray inputs. These extensions still utilize the basic physics models for the transport of electron-hole pairs. Where the number of electron-hole pairs are sampled with a Poisson random variable using Equation 4.2, and the three-dimension distribution of carriers are initialized from burst and thermalization distances calculated from Equations 4.4 and 4.1. The transport of electron-hole pairs takes into account drift and diffusion via Equation 4.8, and trapping is modeled with Equation 4.9. The extension allows for binning of the locations where the electron-hole pairs are collected in the electrodes for a two-dimensional mapping of the detector response. Figure 7.14 shows the point response

function of a 1000 μm thick a-Se detector at 10 V/μm applied electric field, with 10, 13, 30 and 100 keV monoenergetic x-rays, respectively. Over a million histories of incident photons (pencil beam) are simulated. For the 10 keV case in Figure 7.14(a), the point response is the smallest due to the incident energy being the lowest. A significantly distributed point response is observed for the 13 keV case in Figure 7.14(b) due to the generation and reabsorption of fluorescent x-ray photons. The largest point response is observed for 100 keV case in Figure 7.14(d) due to Compton scattering of the incident photons.

7.2.2 Point response function and spectral input

The simulated point response functions using the RQA beam qualities are shown in Figure 7.15 and 7.16. Figure 7.15(a) through (d) show the point response for RQA3, 5, 7 and 9, respectively. Upon initial inspection, the point responses exhibit similar spreading due to the wide range of x-ray spectra used in all the beam qualities. This is not consistent with the PRF results from the monoenergetic x-ray input. In Figure 7.14, the PRF is shown to depend on the incident x-ray energy. For energies above the K-edge of selenium, the PRF is widened due to reabsorption of fluorescent x-rays, and for energies with a high probability of Compton scattering, the PRF is further widened. However, differences in the point response are observed when zooming in on only a smaller range of center pixels are considered shown in Figure 7.16. The spreading in the PRF is the smallest for RQA3 and largest for RQA9. The loss of spatial resolution for higher energies photons can be attributed to the larger range of high-energy electrons in the semiconductor material due to the increase of kinetic energy. As the kinetic energy of the electron increases, the spreading due to the random walk and the burst size calculated from Equation 4.4 are also increased. This combined effect lead to the generation of many electron-hole pairs, and the diffusion of these carriers described in Equation 4.8 in turn cause further spreading in the detected signal.

7.2.3 Detector MTF

The detector MTF can be calculated by taking the Fourier transform of the PRFs. Figure 7.17(a) shows the MTF for 1000 μm thick a-Se detector with incident photon energy of 10, 13, 30 and 100 keV. The MTF is highest for the 10 keV case, because of the low incident energy leading to minimal lateral energy spreading and the energy is below the a-Se K-edge of 12.6 keV. For energies above the K-edge, for example 13 keV, a sharp drop in the MTF is observed. This is due to the reabsorption of characteristic x-rays produced above

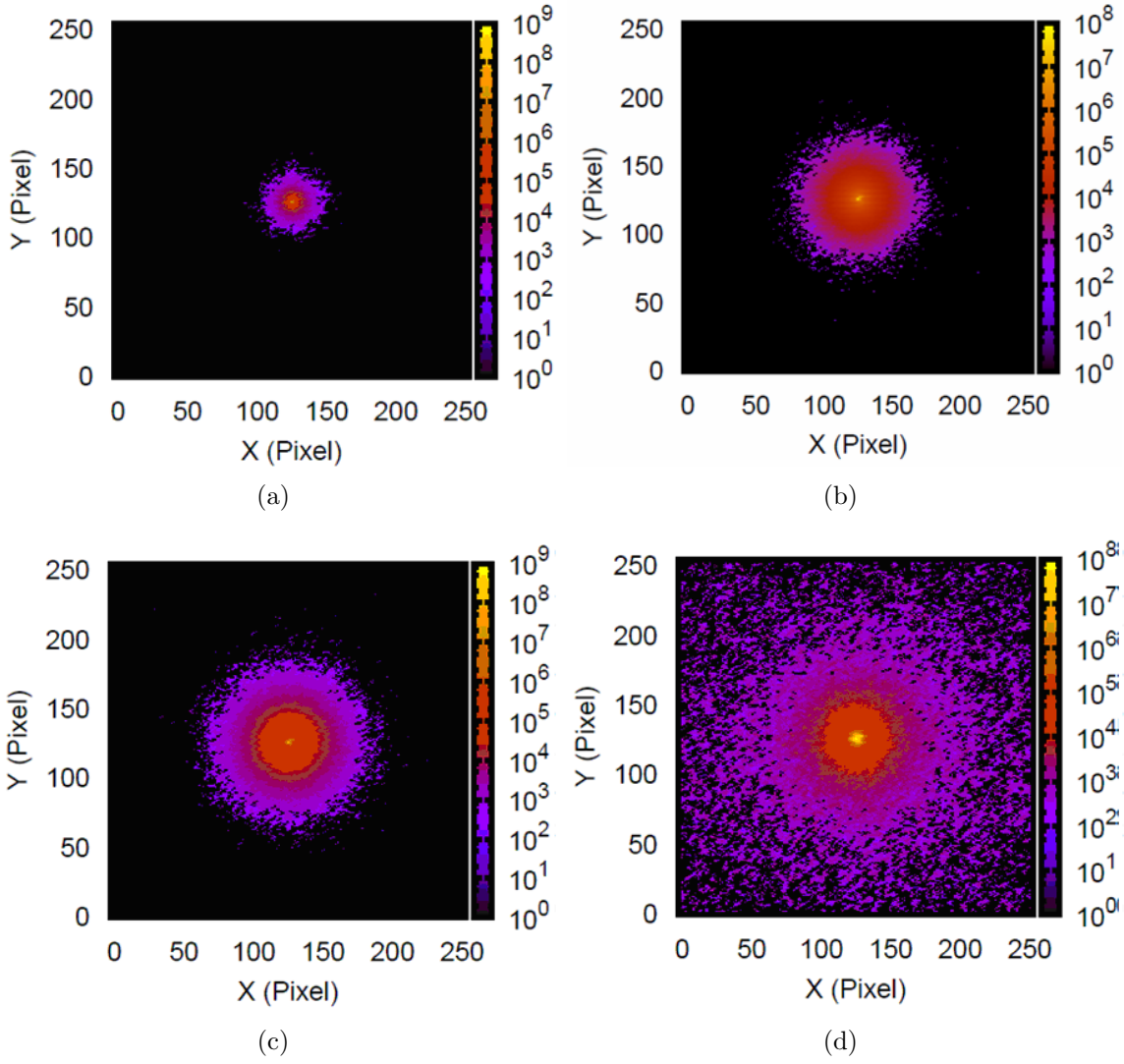

Figure 7.14: (a) Simulated point response function for 10 keV monoenergetic photons. (The scale is normalized with log10 of number of detected electron-hole pairs). (b) Simulated point response function for 13 keV monoenergetic photons. (c) Simulated point response function for 30 keV monoenergetic photons. (d) Simulated point response function for 100 keV monoenergetic photons.

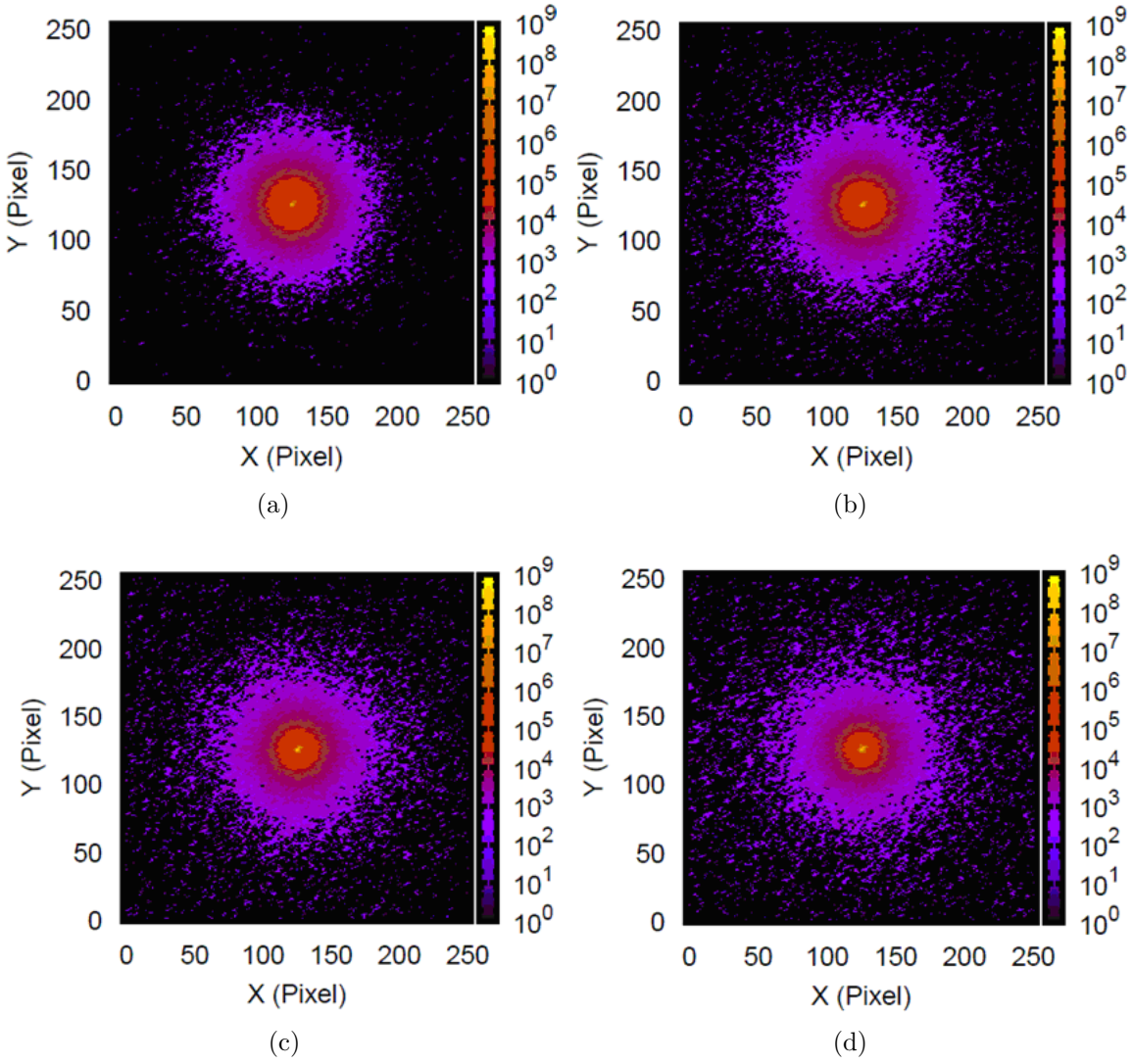

Figure 7.15: (a) Simulated point response function for RQA3. (b) For RQA5. (c) For RQA7. (d) For RQA9.

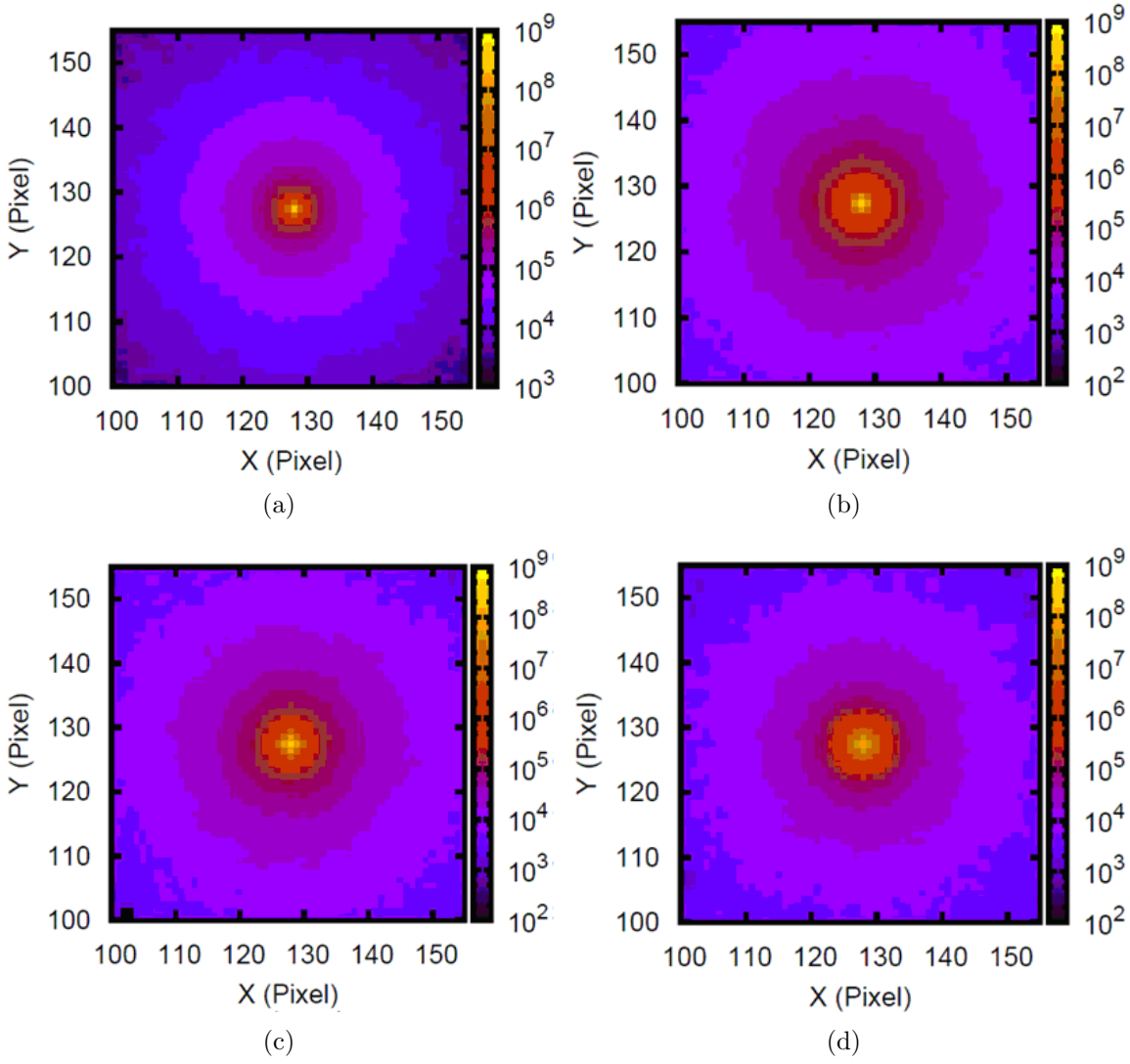

Figure 7.16: (a) Close up of the simulated point response function for RQA3. (b) For RQA5. (c) For RQA7. (d) For RQA9.

the 12.6 keV K-edge. As incident energy increases, more energy is deposited locally by electrons and the MTF is considerably improved. However, the MTF degrades eventually at energies above 100 kev due to Compton scattering.

Figure 7.17(b) shows the MTF for RQA beam qualities, where the MTF for clinical spectra is also shown to depend on the spatial frequency and incident x-ray energy. At low spatial frequencies, the MTF for different RQAs are very similar and not affected significantly by the x-ray energy. However, as the spatial frequency increases, in order to resolve much smaller objects, the energy differences in the RQA radiation qualities become more significant. At 40 lp/mm, MTF is the highest for RQA3 with the lowest energy spectrum and lowest for RQA9 with the highest energy spectrum.

7.2.4 Experimental comparison

The pre-sampled MTF can be calculated from the detector MTF taking into account the aperture effects. Figure 7.18(a) shows the detector MTF for a 1000 μm thick detector, with a range of pixel pitchs from 50 to 200 μm and a comparison of experimental and simulated MTF results. At 150 μm, the Monte Carlo simulations and experimental measurements as a function of spatial frequency can be compared directly. In Figure 7.18(b), some differences in the simulations and measurements are observed and can be due to several reasons. First, some differences in the setup exist for simulation and measurement. Since ideal pencil beams can be implemented in the model, the Monte Carlo point response are simulated, and the resulting MTF is calculated from taking the Fourier transform of the PRF. For experimental measurements, pin holes can be used to collimate the incident x-ray beams in order to get a near-ideal pencil beam. However, the finite pin hole size, and scattering of the pin hole material makes this setup non-perfect. The IEC document recommend the edge test phantom to be used for MTF measurements. The test phantom can be made from an edge material, in this case tungsten to obtain the line spread function (LSF). The scattering of x-rays in the physical tungsten edge phantom can lead to a reduction in the MTF measurement compared to ideal values. Compared to the PSF case, in order to simulate the LSF of a tungsten edge via Monte Carlo simulations require a much higher amount of incident x-rays. The x-ray number also depend on the size of the region-of-interest considered for the LSF calculations and may vary. One physical effect the model is missing is the carbon plating from the detector enclosure. Incident x-rays may be attenuated and scattering the carbon plate causing further reductions in the MTF from theoretical results.

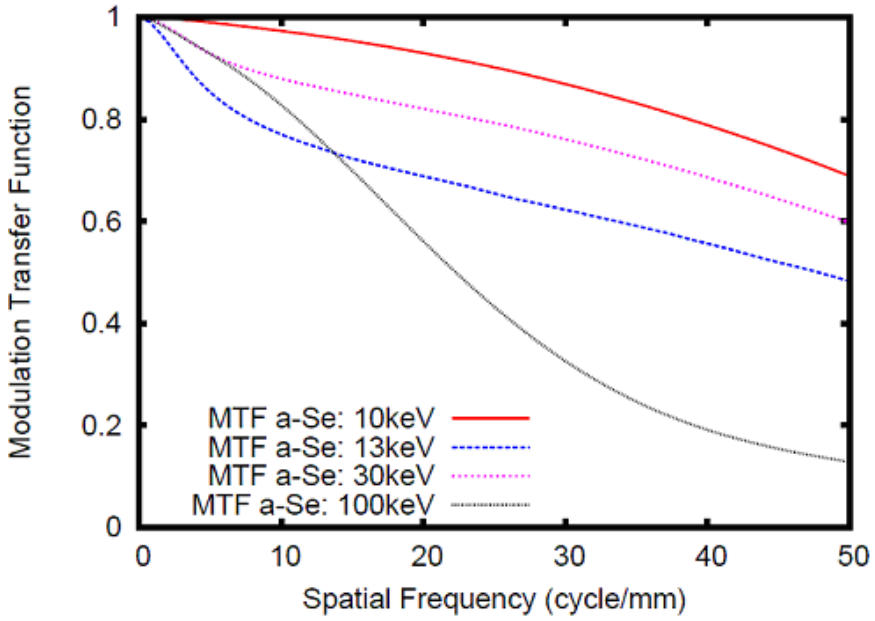

(a)

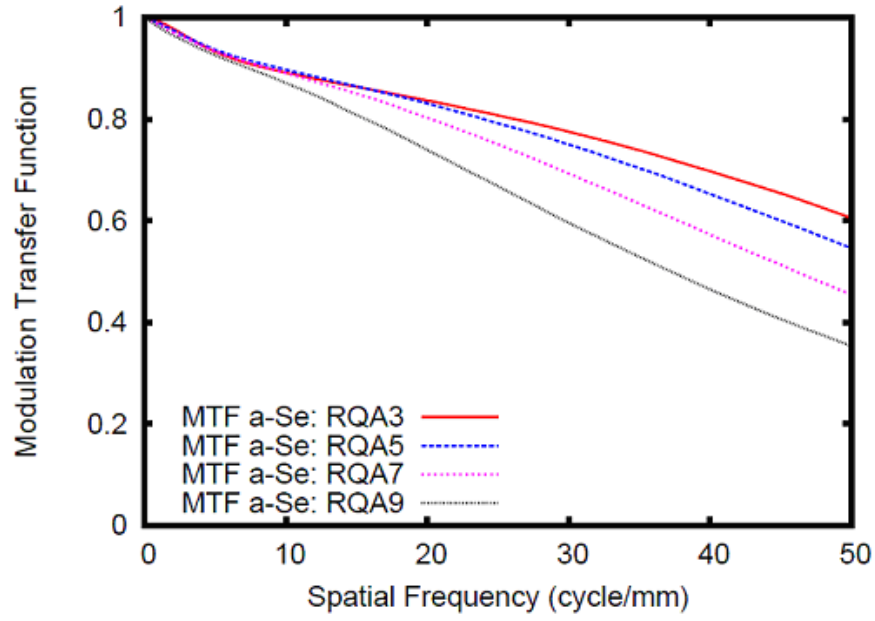

(b)

Figure 7.17: (a) Simulated detector MTF for monoenergetic x-rays. (b) Simulated detector MTF for RQA beam qualities.

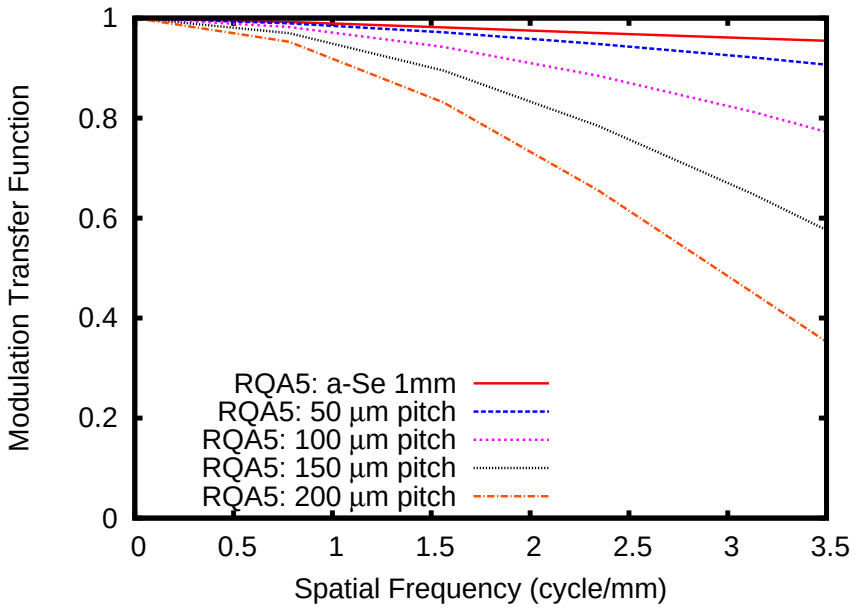

(a)

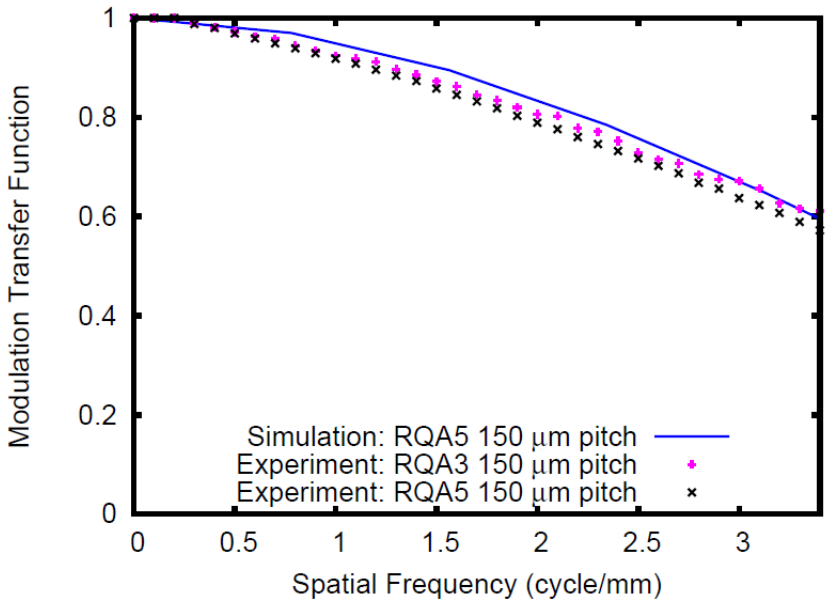

(b)

Figure 7.18: (a) Pre-sampled simulated MTF taking into account the effect of aperture due to pixel pitch for 50 to 200 μm. (b) Comparison of simulated MTF to experimental results.

Chapter 8

Conclusions and contributions

This thesis describes the development of ARTEMIS, a novel transport code for complete Monte Carlo tracking of x rays, energetic electrons and electron-hole pairs to characterize the signal statistics and image quality in a-Se direct x-ray detectors. The use of Monte Carlo methods to model transport of charged carriers in semiconductor x-ray imaging detectors is investigated in Chapter 3, in order to develop a simulation code for modeling the complete signal formation process. This include examining previous work and design a simulation code that leverage on existing Monte Carlo packages for simulation of fundamental x-ray interactions, and maximize the testability and portability of the charge transport model with a modular implementation. The theoretical and implementation details are covered in Chapter 4, along with PHS simulation results and comparison to measurements. Simulation studies impossible with experimental methods are explored in Chapter 5, including the energy weighting, and electronic noise effects on Swank factor and DQE. Chapter 6 contains the study of the effect of different recombination and burst models on simulation results. The performance of a prototype a-Se FPD is evaluated in Chapter 7, in terms of image quality metrics of MTF and DQE. ARTEMIS is used to generate point response images for simulation of pre-sampled MTF and compared with experimental results.

The a-Se detector PHS have been simulated with different transport conditions for a range of mono-energetic incident x-ray energies and mammography radiation beam qualities. Two methods for calculating Swank factors from simulated PHS are shown, one using the entire PHS distribution, and the other using the photo-peak. The latter ignores contributions from Compton scattering and K-fluorescence. Comparisons differ by approximately 2% between experimental measurements and simulations. The a-Se x-ray detector PHS responses simulated in this work include three-dimensional spatial and temporal transport of electron-hole pairs. These PHS were used to calculate the Swank factor and compared to

experimental measurements. The Swank factor was shown to be a function of x-ray energy and applied electric field. Trapping and recombination models are all shown to affect the Swank factor.

Simulated recombination fractions for a single electron-hole pair show good agreement with Onsager model for a wide range of electric field, thermalization distance and temperature. The recombination fraction and Swank noise exhibit a dependence on the burst model for generation of many electron-hole pairs from a single x ray. The Swank noise decreased for the SSA compared to the SUV model at 4 V/μm, while the recombination fraction decreased for SSA compared to the SUV model at 30 V/μm. The NN and FH recombination results were comparable. Results obtained with the ARTEMIS Monte Carlo transport model incorporating drift and diffusion are validated with the Onsager model for a single electron-hole pair as a function of electric field, thermalization distance and temperature. For x-ray interactions, we demonstrated that the choice of burst model can affect the simulation results for the generation of many electron-hole pairs. The SSA model is more sensitive to the effect of electric field compared to the SUV model and that the NN and FH recombination algorithms did not significantly affect simulation results.

Experimental MTF and DQE were measured for a-Se detectors using RQA radiation qualities as a function of thickness and electric field. The ARTEMIS code was used to simulated the MTFs for monoenergetic photons and RQA radiation qualities. Experimental MTF were measured with an edge phantom and calculated from the ESF. Simulated MTF are calculated from the PSF, and Fourier transform from the LSF. The experimental and simulated MTF for RQA5 were compared to validate the MC model.

The ARTEMIS model developed in this work can be improved in several areas to take into account more realistic effects. The recombination fraction was shown to be greatly affected by carrier mobility, and the variability in carrier mobility can also be taken into account by sampling from a range of carrier mobilities. The transport model include a variety of effects such as electric field, thermalization distance and temperature for a single electron-hole pair. The effect of temperature for multiple electron-hole pair transport can be explored in the future. In this work, only detectors with thickness 150 and 1000 μm were simulated, and the effect of detector performance on thickness can be studied as a function of complex trapping models. Finally, experimental PHS measurements with specific monoenergetic x rays energies can be used to further improve the validity of the model.

The original contributions of the research presented in this thesis to the area of medical imaging are summarized below:

1. The developed Monte Carlo simulation code, ARTEMIS, is a comprehensive model

that takes into account the complete image formation process in semiconductor x-ray imaging detectors. No other comprehensive model exists today.

2. This work furthers the understanding in the area of the physics of the x-ray detection process. ARTEMIS will be made open-source and available to the public. This simulation code can be used by engineers for design verification, device optimization, and provides insight into the fundamental limitations of imaging systems for mammography, fluoroscopy, and generally for broad applications of large area digital imaging essential to advanced medical imaging; and allow medical physicists and radiologists to gain a better understanding of the detector technologies and its potential for new imaging modalities.

3. Direct comparison to experimental results and validation of the Monte Carlo simulation models, as pulse height spectra simulation take into account all of the electron-hole pairs created in the signal formation process, which include the total energy deposited per primary x-ray photon.

4. Evaluation of a prototype a-Se x-ray flat-panel detector in terms of image quality measurements of the MTF, NNPS, and DQE, allowing for the study of the detector spatial resolution characteristics.

5. Extension of the ARTEMIS model to allow for image outputs, and simulation of point response functions for MTF calculations and comparison to experimental measurements.

6. Simulation studies with clinical x-ray spectra for a-Se detectors for modeling Swank factor and DQE taking into account the effect of energy weighting and electronic noise characteristics.

7. Simulation studies of the effect of various recombination and burst models on simulation results of detector performance.

List of publications:

- Book chapter and refereed journals

    i. **Y. Fang**, K.S. Karim and A. Badano, "Monte Carlo modeling of x-ray detectors for medical imaging," Semiconductor Radiation Detection System, edited by Krzysztof Iniewski (Submitted book chapter).

ii. **Y. Fang**, A. Badal, N. Allec, K.S. Karim, A. Badano, "Spatiotemporal Monte Carlo transport methods in x-ray semiconductor detectors: Application to pulse-height spectroscopy in a-Se." Medical Physics 39, 308, 2012.

iii. **Y. Fang**, K.S. Karim and A. Badano, "Burst and recombination models for spatiotemporal Monte Carlo transport of interacting carriers in a-Se semiconductor x-ray detectors," (Submitted to Medical Physics)

iv. **Y. Fang**, T. Itou, F. Nariyuki, Y. Hosoi, K.S. Karim and A. Badano, "Spatial resolution characteristics of a-Se imaging detectors using spatiotemporal Monte Carlo transport methods," (To be submitted to Medical Physics)

v. D. Sharma, **Y. Fang**, F. Zafar, K.S. Karim, A. Badano, "Recombination models for spatio-temporal Monte Carlo transport of interacting carriers in semiconductors," Applied Physics Letter 98, 242111, 2011.

vi. A. Badano, M. Freed, **Y. Fang**, "Oblique incidence effects in direct x-ray detectors: A first-order approximation using a physics-based analytical model," Medical Physics 38, 2095, 2011.

vii. D. Sharma, A. Badal, **Y. Fang**, A. Badano, "Hybridmantis: A Novel Method for Faster Monte Carlo Simulation of X-Ray Imaging Detectors," Medical Physics 38, 3834, 2011.

viii. C. Feng, K. Wang, **Y. Fang**, N. Allec, B. George, K. Safa, K.S. Karim, "Direct conversion x-ray detector using lateral amorphous selenium structure," IEEE Sensors 11, 505, 2011.

ix. K. Wang, C. Feng, N. Allec, **Y. Fang**, B. George, K. Safa, K.S. Karim, "Amorphous-Selenium-Based Three-Terminal X-ray Detector With a Gate," IEEE Electron Device Letter 32, 782, 2011.

- Conference proceedings and abstracts

i. **Y. Fang**, A. Badal, A. Badano, and K.S. Karim, "Spatial resolution characteristics of a-Se imaging detectors using spatiotemporal Monte Carlo methods with detailed transport of x rays, electrons and electron-hole pairs under applied bias," Proc. SPIE. 8668, 86683R, 2013.

ii. D. Sharma, H. Dong, **Y. Fang**, A. Badano, "A comparative compendium of publicly available software packages for Monte Carlo simulation of radiation imaging detectors," Proc. SPIE. 8668, 866858, 2013.

iii. **Y. Fang**, D. Sharma, A. Badal, K.S. Karim and A. Badano, "Monte Carlo simulations of a-Se x-ray detectors for breast imaging: Effect of nearest-neighbor recombination algorithm on Swank noise," Proc. IWDM. 575, 2012.

iv. **Y. Fang**, E. O'Bryan, S. Abbaszadeh, H.S. Majid, R.J. Jennings, C. Marini-Bettolo, N. Allec, K.S. Karim and A. Badano, "Pulse-height spectroscopy of amorphous selenium semiconductor detectors for x-ray imaging applications," IEEE Symposium on Radiation Measurement and Applications 2012 (Poster Presentation, Abstract ID: 1290).

v. **Y. Fang**, A. Badal, K.S. Karim, A. Badano, "Spatio-temporal Monte Carlo modeling of a-Se detectors for breast imaging: energy-weighted Swank noise and detective quantum efficiency," Proc. SPIE. 8313, 83135S, 2012. (**Honorable Mention Medical Imaging Poster Award**).

vi. K.W. Shin, K. Wang, N. Allec, **Y. Fang** and K.S. Karim, "Novel silicon x-ray detector with TFT readout," Proc. SPIE. 8313, 83135R, 2012.

vii. **Y. Fang**, A. Badal, N. Allec, K.S. Karim, A. Badano, "Detection statistics in amorphous selenium using Monte Carlo simulation of x-ray, electron, and electron-hole pair transport," RSNA: Radiological Society of North America Annual Meeting 2010, (Oral Presentation, Submission ID: 9005879)

viii. **Y. Fang**, A. Badal, N. Allec, K.S. Karim, A. Badano, "Monte Carlo simulation of Amorphous Selenium Imaging Detectors," Proc. SPIE. 7622, 762214-1, 2010.

ix. **Y. Fang**, N. Allec, K.S. Karim, "Monte Carlo simulation of amorphous selenium digital x-ray detectors: spatial dependence of energy absorption," Proc. CSCBCE, 103, 2010. (**Best Poster Award for Biomedical Engineering**)

x. **Y. Fang**, L. Guo, N. Allec, K.S. Karim, "Modulation transfer function of amorphous selenium digital x-ray detectors," Proc. CSCBCE, 81, 2010.

xi. A.H. Goldan, **Y. Fang**, K.S. Karim, O. Tousignant, H. Mani, L. Laperriere, "Amorphous selenium detector utilizing a Frisch grid for photon-counting imaging applications," Proc. SPIE 7258, 725816-1, 2009.

APPENDICES

Appendix A

PHS simulations

This section contains the results of the detailed spatiotemporal Monte Carlo simulations. Plots of the mono-energetic PHS simulation results, for no electron-hole pair transport, and transport with 4 and 30 V/μm applied electric field with recombination only and with recombination and trapping from 10 to 120 keV. Chapter 4 contains the PHS for 12.5, 40 and 140 keV photon energies to demonstrate the effect of K-edge and Compton scattering on the simulation results. However, in the following plots, more details can be captured. Such as the shift in the fluorescent escape peak as a function of energy, and the gradual increase in the PHS degradations due to low energy Compton energy depositions.

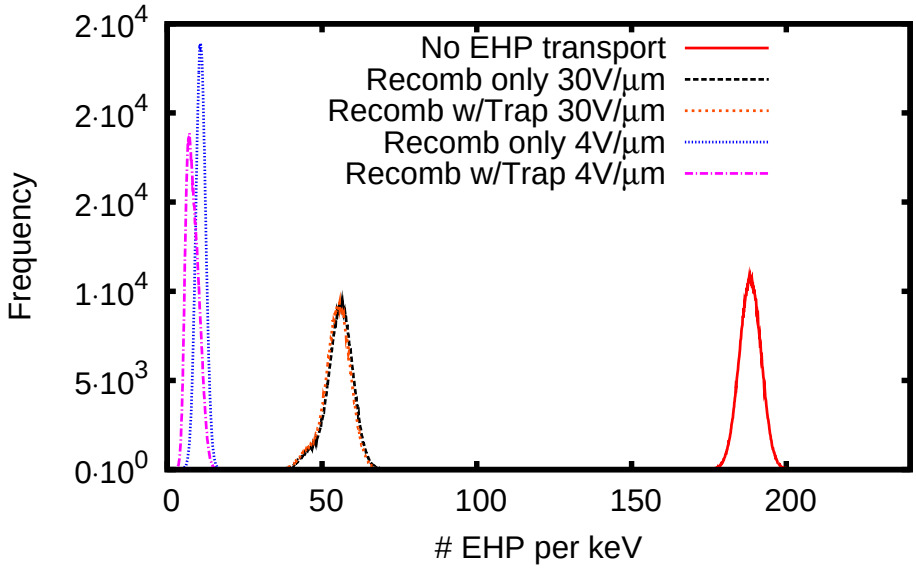

(a)

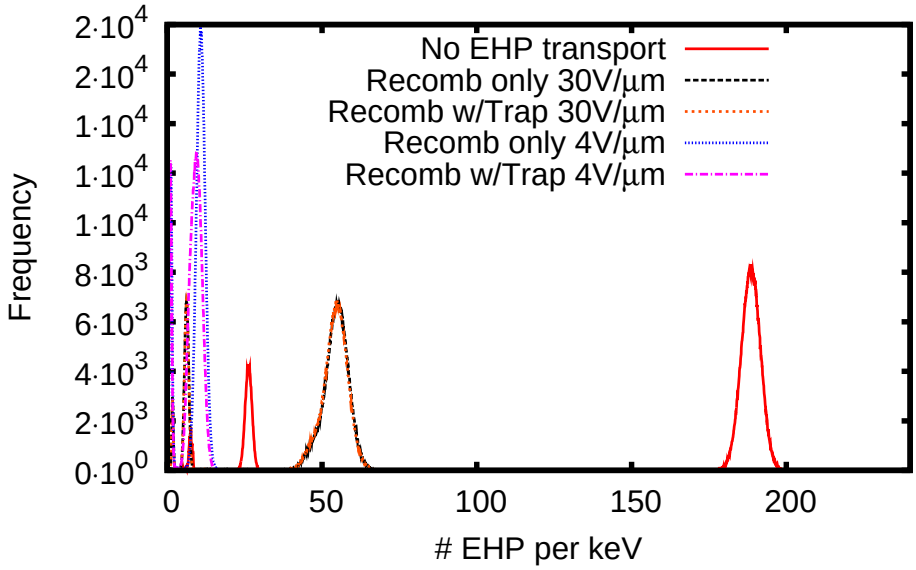

(b)

Figure A.1: (a) Results of the detailed spatiotemporal Monte Carlo simulation. Plots of the pulse-height spectra, for no electron-hole pair transport, and transport with 4 and 30 V/μm applied electric field with recombination only and with recombination and trapping for 10keV mono-energetic x-ray photon. (b) Simulated PHS for 13 keV mono-energetic photons.

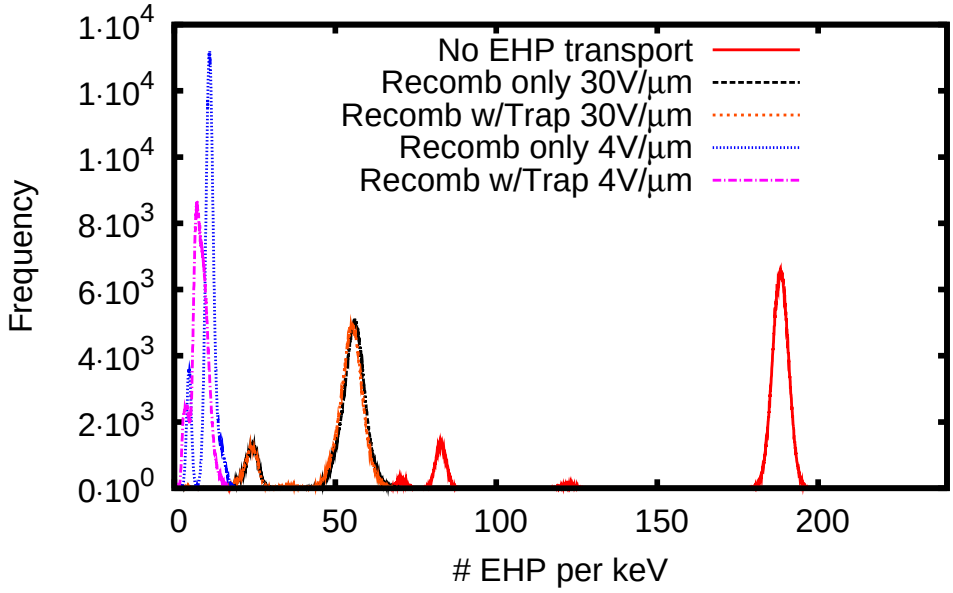

(a)

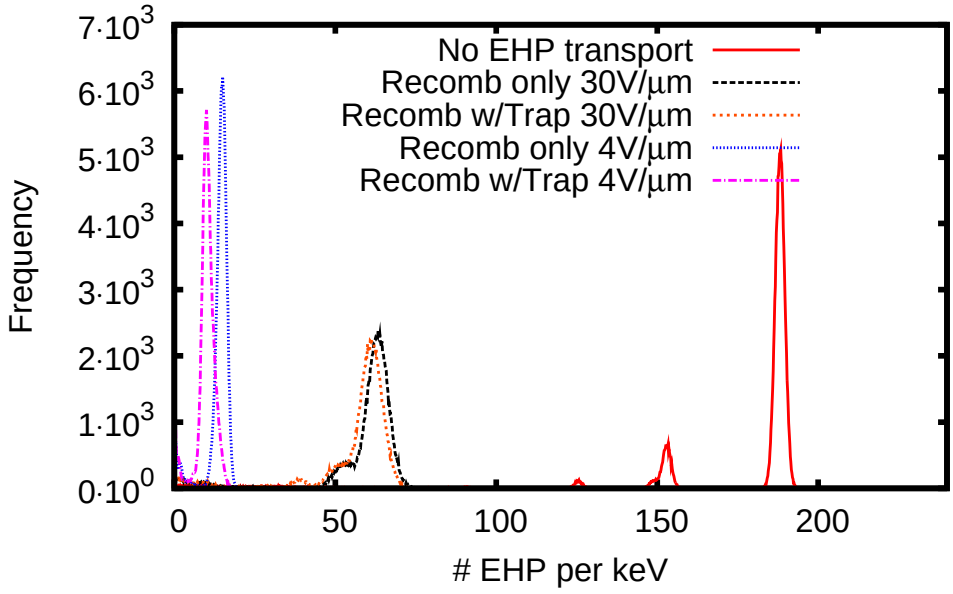

(b)

Figure A.2: (a) Simulated PHS for 20 keV mono-energetic photons. (b) Simulated PHS for 60 keV mono-energetic photons.

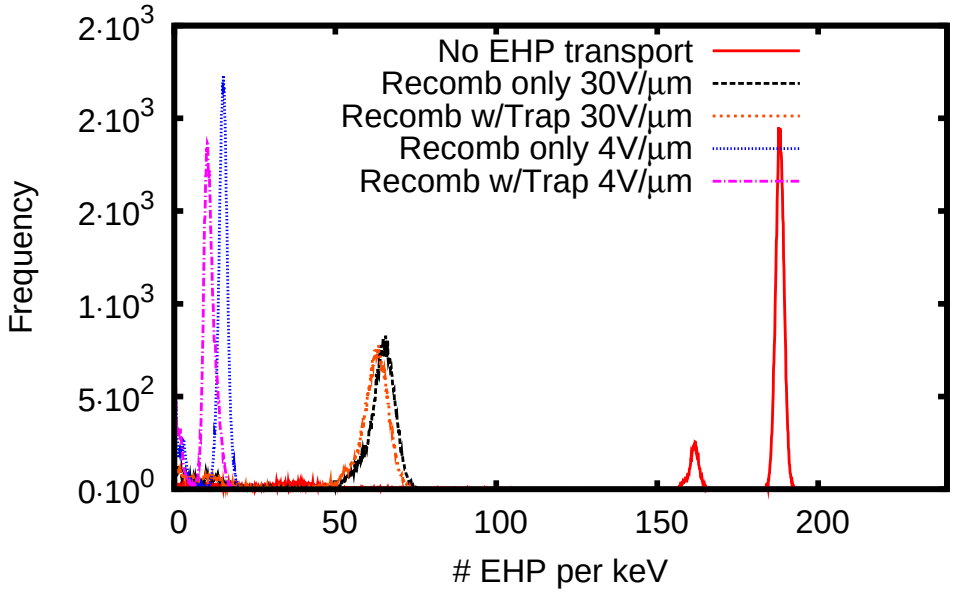

(a)

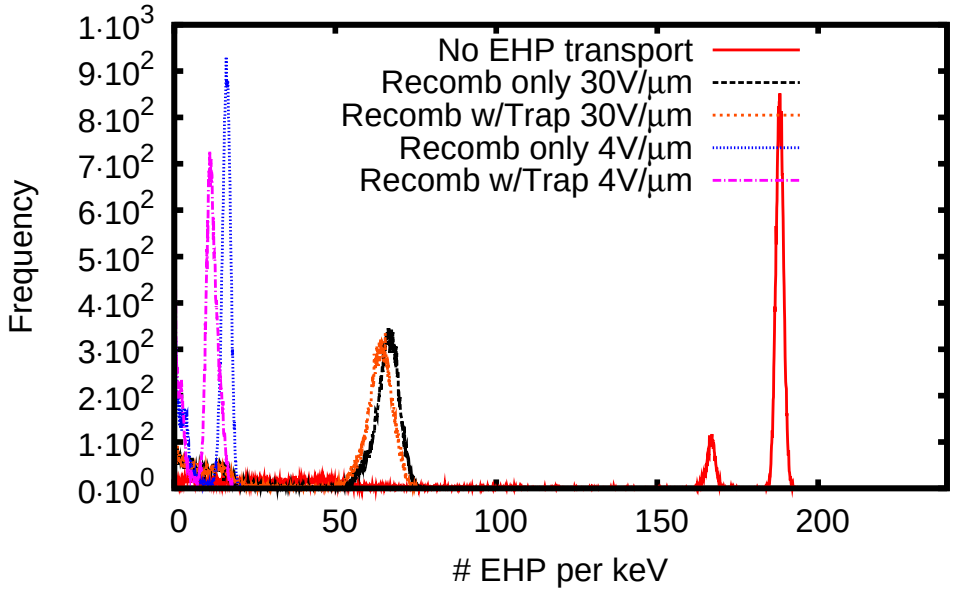

(b)

Figure A.3: (a) Simulated PHS for 80 keV mono-energetic photons. (b) Simulated PHS for 100 keV mono-energetic photons.

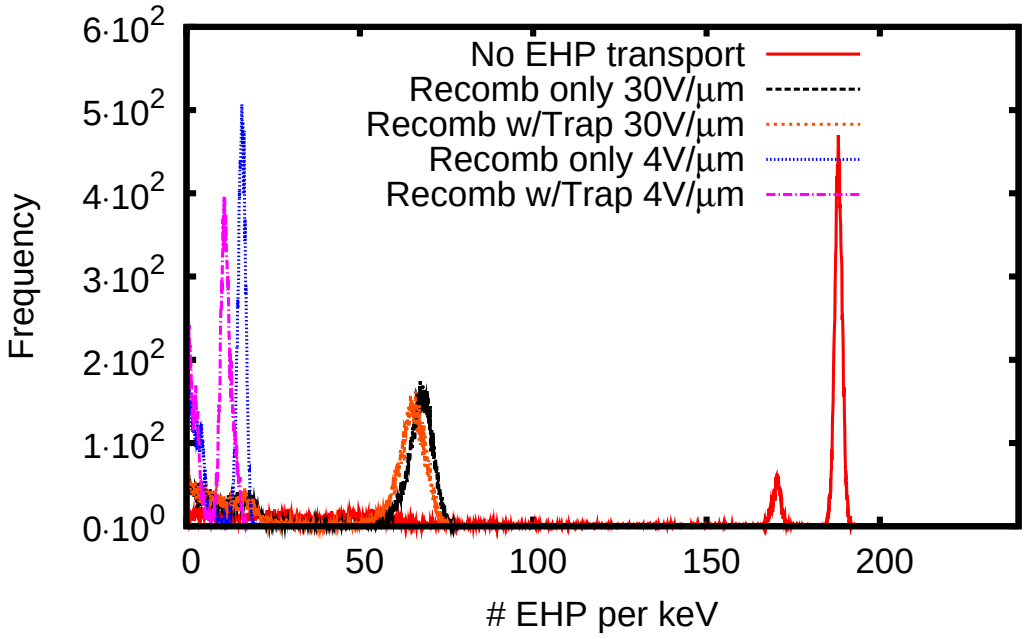

Figure A.4: Simulated PHS for 120 keV mono-energetic photons

Appendix B

Optimization study

This section include the optimization study plots including the input x-ray spectra used, and the PHS simulation results. The input x-ray spectra are shown in Figure B.1. The plot contain the RQA-M radiation qualities based on the anode and filter combination of molybdenum with additiona aluminum filters, with a range of tube voltages from 25 to 35 kVp shown in Figure B.1(a). As the tube voltage increases, the maximum energy of x rays produced increases. Two characteristic x-ray lines are observed for all cases inherent to the material properties of molybdenum. Figure B.1(b) include the input spectra with constant tube voltage of 28 kVp, and different anode and filter combinations: molybdenum/rhodium, rhodium/rhodium, tungsten/molybdenum and tungsten/aluminum. Since the anode and filter materials are different, the resultant spectra have a much different shape compared to Figure B.1(a).

The remaining figures in this section are the simulated PHS used to calculated the optimial swank factor based on the eight input x-ray spectra for a 150 μm thick a-Se detector.

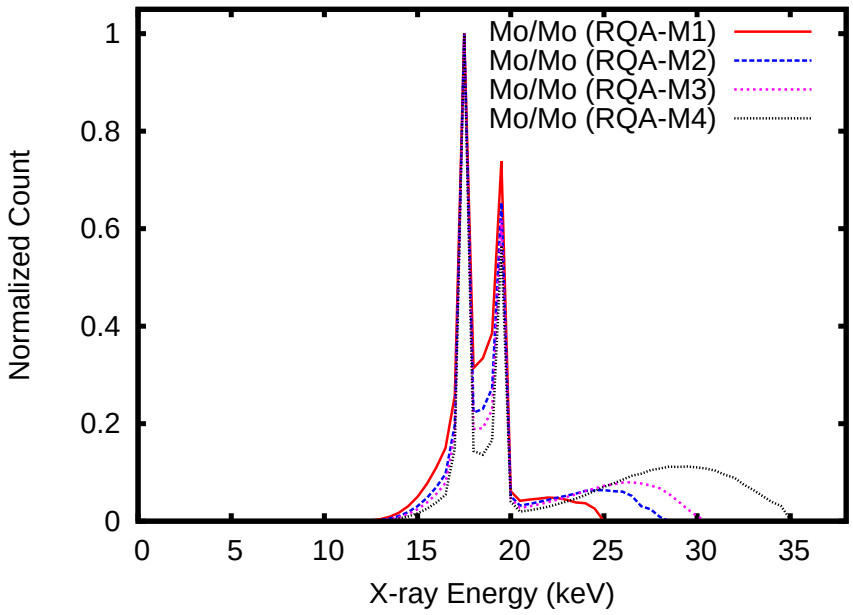

(a)

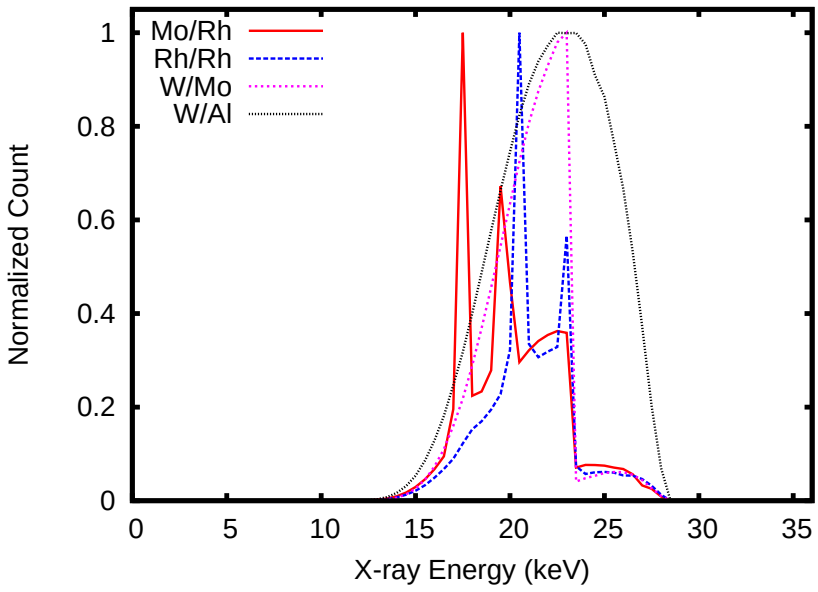

(b)

Figure B.1: (a) The simulated input x-ray spectra based on RQA radiation qualities. (b) The simulated input x-ray spectra with anode and filter combinations: Mo/Rh, Rh/Rh, W/Mo, and W/Al.

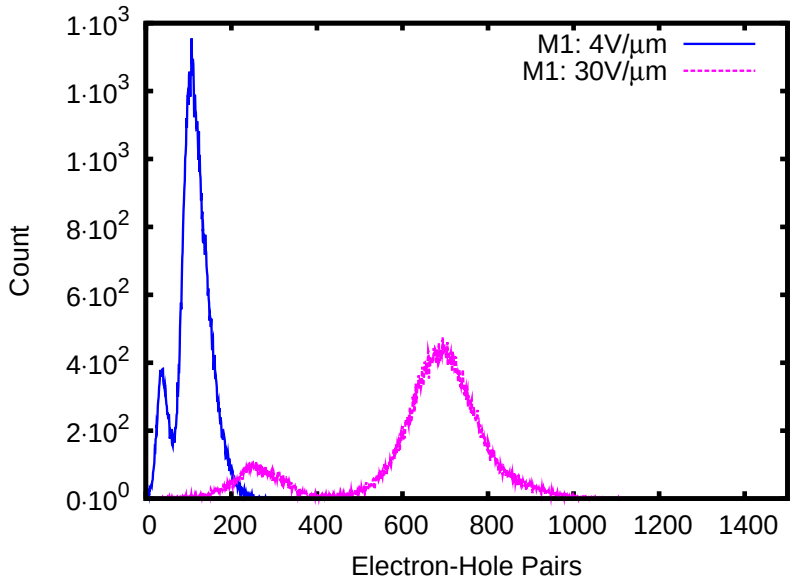

(a)

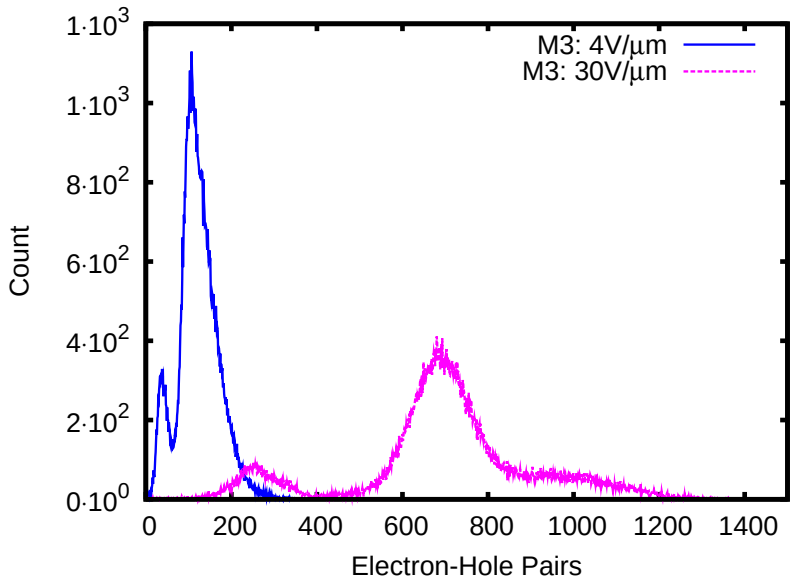

(b)

Figure B.2: (a) Simulated PHS with RQA-M1 molybdenum mammography spectra as a function of electron-hole pair transport for 4 and 30V/μm applied electric field. (b) Simulated PHS with RQA-M3 molybdenum mammography spectra as a function of electron-hole pair transport for 4 and 30V/μm applied electric field.

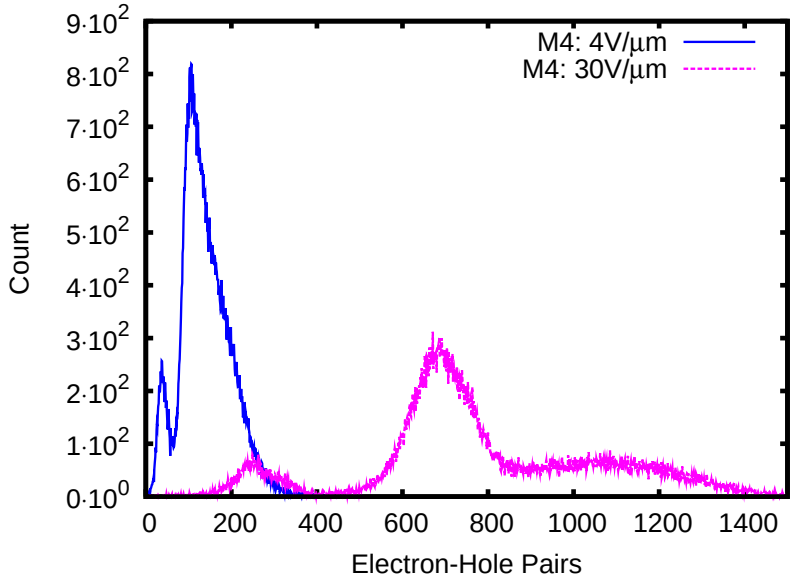

(a)

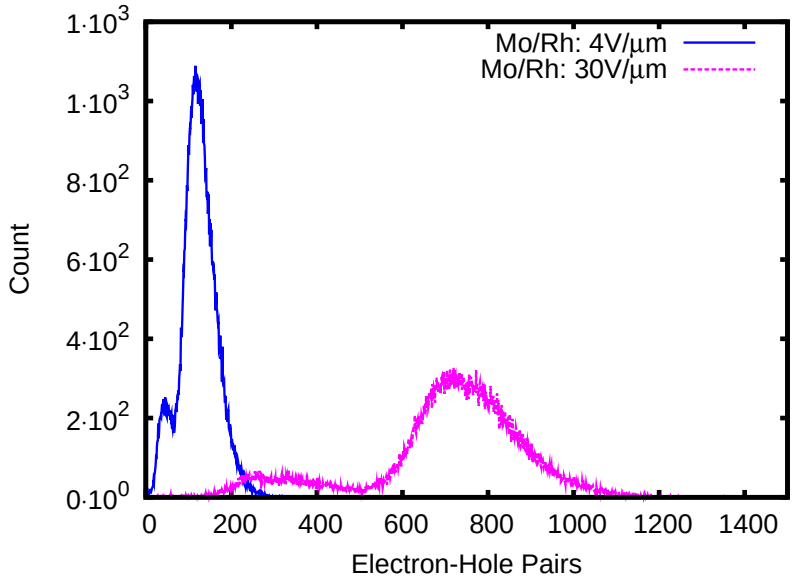

(b)

Figure B.3: (a) Simulated PHS with 4 molybdenum mammography spectra as a function of electron-hole pair transport for 4 and 30V/μm applied electric field. (b) Simulated PHS with molybdenum anode and rhodium filter mammography spectra as a function of electron-hole pair transport for 4 and 30V/μm applied electric field.

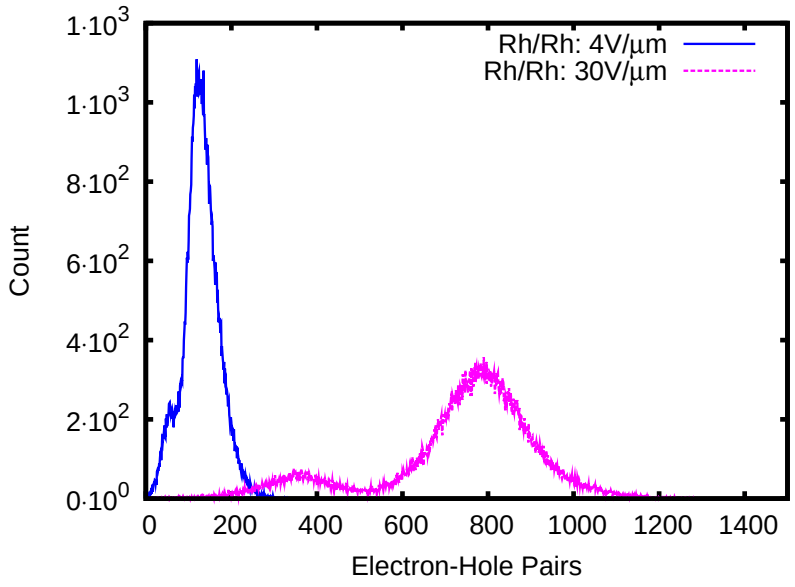

(a)

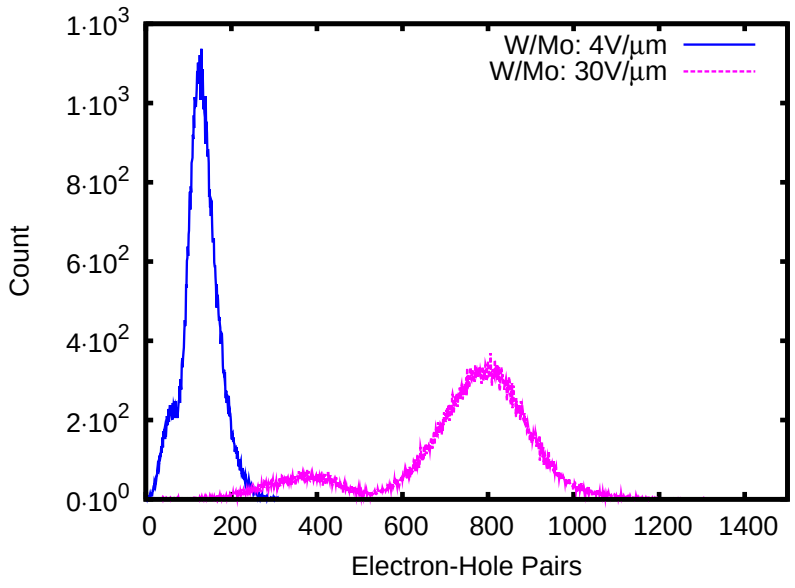

(b)

Figure B.4: (a) Simulated PHS with rhodium anode and filter mammography spectra as a function of electron-hole pair transport for 4 and 30V/μm applied electric field. (b) Simulated PHS with tungsten anode and molybdenum filter mammography spectra as a function of electron-hole pair transport for 4 and 30V/μm applied electric field.

Appendix C

Flat-panel a-Se detector structure

Figure C.1 below contain the layered structure of the a-Se FPD[117] used for the image quality measurements in Chapter 7. The detector has a layered structure, with electrodes, transport layers and the a-Se photoconductor in the middle. A transparent layer of indium tin oxide (ITO) is used for the bottom electrode and gold is used for the top contacting electrode. Hole and electron transport layers are used to prevent carrier injection and leakage. A special C_{60} doped insulating layer is between the a-Se and electron transport layer that provide additional protection to the photoconductor.

The insulating polymer layer is shown to significantly improve the stability of the detector layer to temperature and high voltage effects. Where the C_{60} act as a capsulation layer and also prevent crystallization of the a-Se from heating[117]:

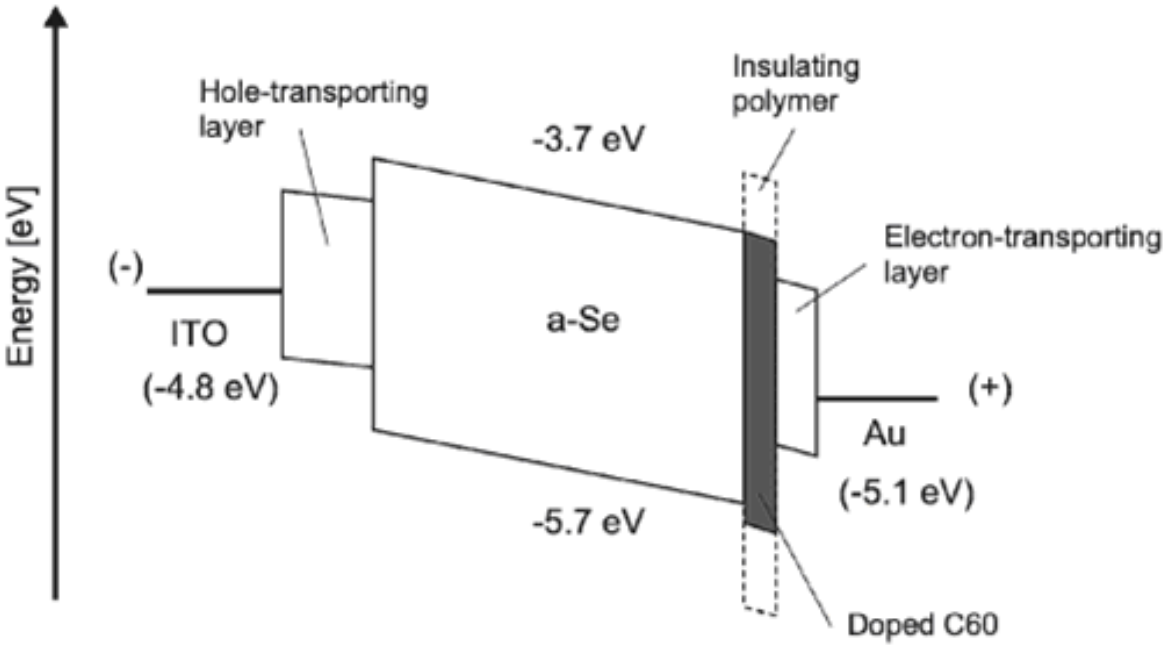

Figure C.1: The energy level diagram of the a-Se detector with C_{60}.

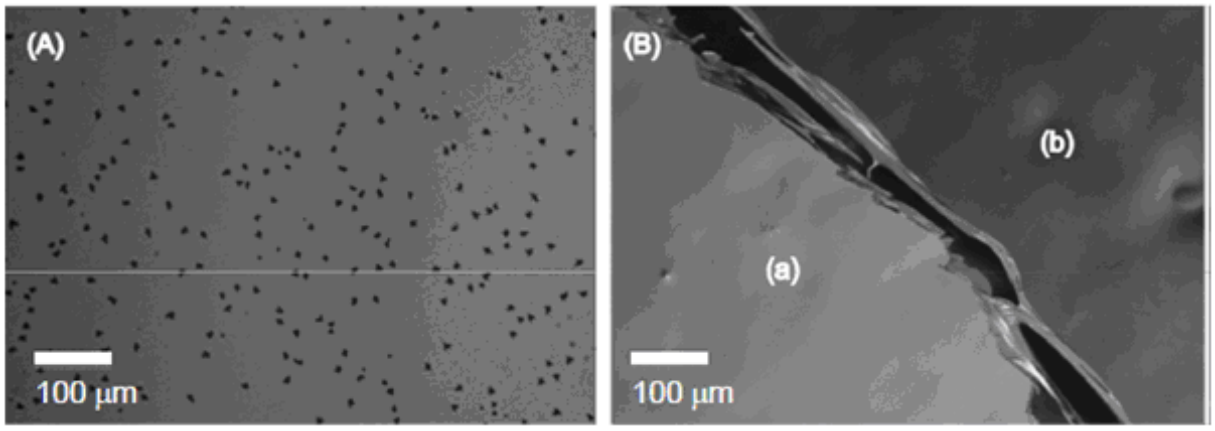

Figure C.2: (a) Crystallized dots on the selenium surface sample due to heating. (b) Selenium sample with C_{60} exhibit no crystallization after heating.

Appendix D

ARTEMIS on Google code

ARTEMIS (pArticle transport, Recombination, and Trapping in sEMiconductor Imaging Simulation) is a Monte Carlo package for modeling direct x-ray detectors for the tracking of x rays, energetic electrons and electron-hole pairs with presence of applied electric field[95].

ARTEMIS uses PENELOPE for the x-ray/electron transport and a custom code for transport of electron-hole pairs. PENELOPE is written in FORTRAN, while the electron-hole pair transport code is written in C. The electron-hole pair transport source code is called as subroutines from the PENELOPE ionizing radiation transport code.

ARTEMIS is being developed at the U.S. Food and Drug Administration, Center for Devices and Radiological Health, Office of Science and Engineering Laboratories, Division of Imaging and Applied Mathematics. The source code, documentation and example files are available at www.google.com/p/artemis .

References

[1] "The x-ray tube," http://whs.wsd.wednet.edu/faculty/busse/mathhomepage/. xi, 5

[2] M. Yunus, "Monte Carlo modeling of the sensitivity of X-ray photoconductors," Master's thesis, Dept. of Electrical Engineering, University of Saskatchewan, 2005. xii, 11, 12, 15

[3] K. Mandal, "Amorphous selenium based detectors for medical imaging applications," *Proc. SPIE*, vol. 6319, p. 6319N, 2006. xii, 17, 18

[4] Q. Jiang, A.W. Brinkman, B.J. Cantwell, J.T.Mullins, F. Dierre, A. Basu, P. Veeramani and P. Sellin, "Growth of Thick Epitaxial CdTe films by Close Space Sublimation," *J. Electronic Materials*, vol. 38, p. 1548, 2003. xii, xiii, 19, 20, 21

[5] S. Alamri, "The growth of CdTe thin film by close space sublimation system," *Phys. Stat. Sol.*, vol. 200, p. 352, 2003. xiii, 19, 22

[6] H. Nagayoshi and K. Suzuki, "Growth of thick CdTe films by close-space-sublimation technique," *IEEE Trans. Nuclear Science*, vol. 7, p. 4411, 2004. xiii, 19, 23

[7] M. Simon, R.A. Ford, A.R. Franklin, S.P. Grabowski, B. Menser, G. Much, A. Nascetti, M. Overdick, M.J. Powel and D.U. Wiechert, "PbO as direct conversion x-ray detector material," *Proc. SPIE*, vol. 5368, p. 188, 2004. xiii, 23, 26

[8] M. Simon, R.A. Ford, A.R. Franklin, S.P. Grabowski, B. Menser, G. Much, A. Nascetti, M. Overdick, M.J. Powel and D.U. Wiechert, "Analysis of Lead Oxide (PbO) Layers for Direct Conversion X-Ray Detection," *IEEE Trans. Nuclear Science*, vol. 52, p. 2035, 2005. xiii, 23, 26

[9] H.H. Barrett, J.D. Eskin and H.B. Barber, "Charge transport in arrays of semiconductor gamma-ray detectors," *Phys. Rev. Lett.*, vol. 75, pp. 156–159, 1995. xiii, 33, 34

[10] D. Sharma, Y. Fang, F. Zafar, K. S. Karim and A. Badano, "Recombination models for spatio-temporal Monte Carlo transport of interacting carriers in semiconductors," *App. Phys. Let.*, vol. 98, p. 242111, 2011. xvii, 48, 71, 83, 85, 86, 90

[11] "Medical electrical equipment - Characteristics of digital x-ray imaging devices - Part1: Determination of the detective quantum efficiency," Tech. Rep. International Standard IEC 622220, 2007. xviii, 96, 97, 98, 102

[12] G. Knoll, *Radiation Detection and Measurement*, pp. 365–366. Wiley Interscience, John Wiley and Sons, Inc., 2010. 1

[13] R. Schulz-Wendtland, K.P. Hermann, E. Wenkel, B. Adamietz, M. Lell, K. Anders and M. Uder, "First experiments for the detection of simulated mammographic lesions. Digital full field mammography with a new detector with a double plate of pure selenium," *Radiologe*, vol. 51, pp. 130–134, 2011. 1

[14] A.L. Goertzen, V. Nagarkar and R.A. Street, "A comparison of x-ray detectors for mouse CT imaging," *Phys. Med. Bio.*, vol. 49, pp. 5251–5265, 2004. 1

[15] M. Bissonnette, M. Hansroul, E. Masson and S. Savard, "Digital breast tomosynthesis using an amorphous selenium flat panel detector," *Proc. SPIE*, vol. 5745, pp. 529–540, 2005. 1, 11

[16] E. Fredenberg, M. Hemmendorff, B. Cederstrom, M. Aslund and M. Danielsson, "Contract enhanced spectral mammography with a photon-counting detector," *Med. Phys.*, vol. 37, pp. 2017–2029, 2010. 1

[17] A. Badano and J. Sempau, "MANTIS: combined x-ray, electron and optical Monte Carlo simulation of indirect radiation imaging system," *Phys. Med. Biol.*, vol. 51, pp. 1545–1561, 2006. 1

[18] M. Benoit and L.A. Hamel, "Simulation of charge collection process in semiconductor CdZnTe γ-ray detectors," *Nucl. Inst. Meth. Phys. Res. A*, vol. 606, pp. 508–516, 2009. 1

[19] M. Yunus, M.Z. Kabir and S.O. Kasap, "Sensitivity reduction mechanisms in amorphous selenium photoconductive x-ray image detectors," *Appl. Phys. Lett.*, vol. 85, pp. 6430–6432, 2004. 1, 31, 51, 93

[20] M. Lachaine and B.G. Fallone, "Calculation of inelastic cross-section for the interaction of electron with amorphous selenium," *J. Phys. D.*, vol. 33, pp. 551–555, 2000. 1, 16

[21] E. Fourkal, M. Lachaine and B.G. Fallone, "Signal formation in amorphous-Se-based x-ray detectors," *Phys. Rev. B.*, vol. 63, pp. 195–204, 2001. 1, 48

[22] Z. Shakoor, "Monte Carlo Simulation of Charge Transport in Amorphous Selenium Photoconductors," Master's thesis, Dept. of Electrical Engineering, University of Saskatchewan, 2006. 1

[23] "The Nobel Prize in Physics 1901, Wilhelm Conrad Rontgen for the discovery of x rays," http://www.nobelprize.org/nobel$_p rizes/physics/laureates/1901/.4$

[24] J. Als-Nielsen and D. McMorrow, *Elements of Modern X-ray physics*. John Wiley & Sons, 2011. 4

[25] J. T. Bushberg, J. A. Seibert, E. M. Leidholdt Jr. and J. M. Boone, *The Essential Physics of Medical Imaging, Second Edition*. Pippincott Williams & Wilkins, Philadelphia, 2002. 7

[26] M. Kabir, *Modeling of X-ray photoconductors for X-ray image detectors*. PhD thesis, Dept. of Electrical Engineering, University of Saskatchewan, 2005. 7, 13

[27] E. E. Christensen, T. S. Curry III and J. E. Dowdey, *Basic interactions between X-rays and Matter: An Introduction to the Physics of Diagnostic Radiology, Second Edition*. Lea & Febiger, Philadelphia, 1978. 8

[28] J.A. Rowlands and J. Yorkston, *Flat panel detectors for digital radiography in Handbook of Medical Imaging Vol.1*. SPIE Press, Washington, 2000. 10, 17, 93

[29] B.D. Gallas, J.S. Boswell, A. Badano, R.M. Gagne and K.J. Myers, "An energy- and depth-dependent model for x-ray imaging," *Med. Phys.*, vol. 31, p. 3132, 2004. 12

[30] A. Badano, M. Freed and Y. Fang, "Oblique incidence effects in direct x-ray detectors: A first-order approximation using a physics-based analytical model," *Med. Phys.*, vol. 38, p. 2095, 2011. 12

[31] A. Badano, I.S. Kyprianou and J. Sempau, "Anisotropic imaging performance in indirect x-ray imaging detectors," *Med. Phys.*, vol. 33, pp. 2698–2713, 2006. 12

[32] S.O. Kasap and J.A. Rowlands, ""Direct-conversion flat-panel X-ray image detectors," *IEE Proc. CDS*, vol. 149, p. 85, 2002. 13, 19

[33] E. Samei and M. J. Flynn, "An experimental comparison of detector performance for direct and indirect digital radiography systems," *Med. Phys.*, vol. 30, p. 608, 2003. 14

[34] R. Murty, "Effective atomic numbers of heterogeneous materials," *Nature*, vol. 207, p. 389, 1965. 15

[35] E.J. Yun, H.W. Lee, J.S. Lee and S.H. Nam, "Characteristics of Amorphous Selenium Detectors for Monoenergetic X-ray Determined by Monte Carlo Simulation," *IEEE Trans. Nuclear Science*, vol. 1, p. 444, 2002. 16

[36] S. Kasap, *Photoreceptors: the selenium alloys, in Handbook of Imaging Materials.* Marcel Dekker, New York, 1991. 17, 18

[37] J.D. Plummer, M. Deal and P.B. Friffin, *Silicon VLSI technology: fundamentals, practice and modeling.* Prentice Hall, 2000. 18

[38] S. Tokuda, H. Kishihara, S. Adachi and T. Sato, "Preparation and characterization of polycrystalline CdZnTe films for large-area, high sensitivity X-ray detectors," *J. Mat. Sci.: Mat. Electron*, vol. 15, p. 1, 2004. 19

[39] M. Schieber, A. Zuck, H. Gilboa and G. Zentai, "Reviewing Polycrystalline Mercuric Iodide X-ray Detectors," *IEEE Trans. Nuclear Science*, vol. 53, p. 2385, 2008. 21

[40] M. Schieber, H. Hermon, A. Zuck, A. Vilensky, L. Melekhov, R. Shatunovsky, E. Meerson, Y. Saado, M. Lukach, E. Pinkhasy, S.E. Ready and R.A. Street, "Thick films of X-ray polycrystalline mercuric iodide detectors," *J. Crystal Growth*, vol. 225, p. 118, 2001. 21

[41] "Dxray, inc., custom digital x-ray imaging solutions, technology gallery," http://www.dxray.com/wp-content/uploads/2010/06/tpic4.png. 21

[42] "Interon as," Digitally focusing X-rays", http://www.interon.no/?page$_i d = 18.21$

[43] G. Zentai, L. Partain, R. Pavlyuchkova, C. Proano, Y. G. Virshup, L. Melekhov, A. Zuck, B.N. Breen, O. Dagan, A. Vilensky, M. Schieber, H. Gilboa, P. Bennet, K. Shan, Y. Dmitiev, J. Thomas, M. Yaffe and D. Hunter, "Mercuric iodide and lead iodide x-ray detectors for radiography and fluoroscopic medical imaging," *Proc. SPIE*, vol. 207, p. 77, 2003. 21

[44] G. Zentai, L. Partain, R. Pavlyuchkova, C. Proano, B.N. Breen, A. Taieb, O. Dagan, M. Schieber, H. Gilboa and J. Thomas, "Mercuric iodide medical imagers for low exposure radiography and fluoroscopy," *Proc. SPIE*, vol. 5368, p. 200, 2004. 21

[45] B.D. Yanoff, Z.P. Wu, K. Tao, Y. Sun, J. Xiao, L. Zheng, W. Peng and J. Li, "Particle-in-binder x-ray sensitive coating using polyimide binder," *US Patent*, vol. 7507145, 2009. 21, 22

[46] R.A. Street, S.E. Ready, K. Van Schuylenbergh, J. Ho, J.B. Boyec, P. Nylen, K. Shah, L. Melekov and H. Hermon, "Comparison of PbI2 and HgI2 for direct detection active matrix x-ray image sensors," *J. App. Phys.*, vol. 91, p. 3345, 2002. 21

[47] Y. Fang, A. Badal, N. Allec, K. S. Karim and A. Badano, "Monte Carlo simulation of amorphous selenium imaging detectors," *Proc. SPIE 7622*, pp. 762214–1–762214–9, 2010. 27

[48] M.J. Berger and S.M. Seltzer, *Monte Carlo Transport of Electrons and Photons*. New York: Plenum, 1988. 29

[49] J.A. Halbleib, R.P. Kensek, T.A. Mehlhorn, G.D. Valdez, S.M. Seltzer and M.J. Berger, "ITS version 3.0: the integrated TIGER series of coupled electron/photon Monte Carlo transport codes," Tech. Rep. SAND91-1634, 1992. 29

[50] F. Salvat, J.M. Fernàndez-Varea and J. Sempau, "PENELOPE-2006: A code system for Monte Carlo Simulation of Electron and Photon Transport," tech. rep., 2006. 29, 54, 75

[51] I. Kawrakow and D.W.O. Rogers, "The EGSnrc code system: Monte Carlo simulation of electron and photon transport," Tech. Rep. PIRS-701, 2001. 29

[52] "MCNP - A General Monte Carlo N-Particle Transport Code, Version 5," Tech. Rep. LAUR-03-1987, X-5 Monte Carlo Team, 2003. 29

[53] S. Agostinelli and et al., "Geant4 - a simulation toolkit," *Nucl. Inst. Meth. Phys. Res. A*, p. 506, 2003. 29

[54] A. Ferrari, P.R. Sala, A. Fassuo and J. Ranft, "FLUKA: a multi-particle transport code (Program version 2005)," Tech. Rep. CERN-2005-10, INFN/TC-05/11, SLAC-R-773, 2005. 29

[55] Y. Fang, N. Allec and K. S. Karim, "Monte Carlo simulation of amorphous selenium digital x-ray detectors: spatial dependence of energy absorption," *Proc. CSCBCE*, vol. 5, p. 103, 2010. 31

[56] C. Feng, K. Wang, Y. Fang, N. Allec, B. George, K. Safa and K.S. Karim, "Direct conversion x-ray detector using lateral amorphous selenium structure," *IEEE Sensors* , vol. 11, p. 505, 2011. 31

[57] K. Wang, C. Feng, N. Allec, Y. Fang, B. George, K. Safa and K.S. Karim, "Amorphous-Selenium-Based Three-Terminal X-ray Detector With a Gate," *IEEE Electron Device Letter*, vol. 32, p. 782, 2011. 31

[58] K. Koughia, Z. Shakoor, S.O. Kasap and J.M. Marshall, "Density of localized electronic states in a-Se from electron time-of-flight photocurrent measurement," *J. Appl. Phys.*, vol. 97, pp. 033706–1–033706–11, 2005. 31, 93

[59] C. Moisan, D. Vooza and M. Loope, "Simulating the performance of an LSO based position encoding detector for PET," *IEEE Trans. Nuclear Science*, vol. 44, pp. 2450–2458, 1997. 32

[60] D. Vooza, C. Moisan and and S. Pasquet, "An improved model for the energy resolution of multicrystal encoding detector for PET," *IEEE Trans. Nuclear Science*, vol. 44, pp. 179–183, 1997. 32

[61] J.C. Blakesley and R. Speller, "Modeling the imaging performance of prototype organic x-ray imagers," *Med. Phys.*, vol. 35, pp. 225–239, 2008. 33

[62] T. Radcliffe, G. Barnea, B. Wowk, R. Rajapakshe and S. Shalev, "Monte Carlo optimization of metal/phosphor screens at megavotlage energies," *Med. Phys.*, vol. 20, p. 1161, 1993. 33

[63] R. Fasbender, H. Li and A. Winnacker, "Monte Carlo modeling of storage phosphor plate readout," *Nucl. Inst. Meth. Phys. Res. A*, vol. 512, p. 610, 2003. 33

[64] C. Kausch, B. Schreiber, F. Kreuder, R. Schmidt and O. Dossel, "Monte Carlo simulation of the imaging performance of metal/plate phosphor screens used in radiotherapy," *Med. Phys.*, vol. 26, p. 2113, 1999. 33

[65] A. Badano, I.S. Kyprianou and R.J. Jennings, "Anisotropic imaging performance in breast tomosynthesis," *Med. Phys.*, vol. 34, p. 4076, 2007. 33

[66] A. Badal and A. Badano, "Accelerating Monte Carlo simulation of photon transport in a voxelized geometries using a massively parallel graphic processing unit," *Med. Phys.*, vol. 36, p. 4878, 2009. 33

[67] A. Badal and A. Badano, "Monte Carlo simulation of X-ray imaging using a graphics processing unit," *IEEE Nuclear Science Symposium*, p. 4081, 2009. 33

[68] A. Badal, I. Kyprianou, D. Sharma and A. Badano, "Fast cardiact CT simulation using a graphics processing unit-accelerated Monte Carlo code," *Proc. SPIE*, vol. 7622, p. 762231, 2010. 33

[69] D. Sharma, A. Badal and A. Badano, "hybridMANTIS: a CPU-GPU Monte Carlo method for modeling indirect x-ray detector with columnar scintillators," *Phys. Med. Biol.*, vol. 57, p. 2357, 2012. 33

[70] D. Sharma and A. Badano, "Comparison of experimental, MANTIS, and hybridMantis x-ray response for a breast imaging CsI detector," *Proc. IWDM*, p. 56, 2012. 33

[71] A. Ginzburg and C. Dick, "Image Information transfer properties of x-ray intensifying screens in the energy range from 17 to 320 keV," *Med. Phys.*, vol. 20, p. 1013, 1993. 35

[72] R.K. Swank, "Absorption and noise in x-ray phosphors," *J. App. Phys.*, vol. 44, p. 4199, 1993. 35

[73] C.E. Dick and J.W. Motz, "Image information transfer properties of x-ray fluorescent screens," *Med. Phys.*, vol. 8, p. 4337, 1981. 35

[74] I.M. Blevis, D.C. Hunt and J.A. Rowlands, "X-ray imaging using amorphous selenium: Determination of Swank factor by pulse height spectroscopy," *Medical Physics*, vol. 25, pp. 638–641, 1998. 36, 37, 66

[75] I.M. Blevis, D.C. Hunt and J.A. Rowland, "Digital radiology using amorphous selenium and active matrix flat panel readout: photoconductive gain and gain fluctuations," *Proc. SPIE*, vol. 3336, p. 486, 1998. 36, 37

[76] I.M. Blevis, D.C. Hunt and J.A. Rowland, "Measurement of x-ray photogeneration in amorphous selenium," *J. Appl. Phys.*, vol. 85, pp. 7958–7962, 1999. 36, 37, 93

[77] "Untra-LEGe Detector (GUL)," Tech. Rep. Canberra Industries, 2012. 37

[78] R.G. Helmer and C. Van Der Leun *Nucl. Instrum. Methods A*, vol. A450, p. 35, 2000. 38

[79] R.W. Fink *Phys. Rev.*, vol. 180, p. 1220, 1969. 38

[80] Y. Hino and Y. Kawada *Appl. Radiat. Isot.*, vol. 40, p. 79, 1989. 38

[81] A. Grutter *Int. J. Appl. Radiat. Isotop.*, vol. 33, p. 533, 1982. 38

[82] R. Vennink, J. Kopecky, P.M. Endt and P.W.M. Glaudemans *Nucl. Phys.*, vol. A344, p. 421, 1980. 38

[83] J. M. Boone, T. R. Fewell and R. J. Jennings, "Molybdenum, rhodium, and tungsten anode spectral models using interpolating polynomials with application to mammography ," *Med. Phys.*, vol. 24, pp. 1863–1874, 1997. 41, 72

[84] J.C Knight and E.A. Davis, "Photogeneration of charge carrier in amorphous selenium," *J. Phys. Chem. Solids*, vol. 35, pp. 543–554, 1975. 45, 90, 93

[85] C.A. Klein, "Bandgap dependence and related features of radiation ionization energies in semiconductors," *J. Appl. Phys.* , vol. 39, p. 2029, 1968. 47

[86] W. Que and J.A. Rowlands, "X-ray photogeneration in amorphous selenium: Geminate versus columnar recombination," *Phys. Rev. B*, vol. 51, pp. 10500–10507, 1995. 47, 48, 49, 82, 93

[87] W. Que and J.A. Rowlands, "X-ray imaging using amorphous selenium: inherent spatial resolution," *Med. Phys.*, vol. 22, p. 365, 1995. 48

[88] S.O. Kasap and J.A. Rowlands, "Direct-conversion flat-panel x-ray image sensors for digital radiography," *Proc. IEEE*, vol. 9, p. 591, 2002. 48, 49

[89] L.K. Townsley and P.S. Broos and G. Chartas and E. Moskalenko and J.A. Nousek and G.G. Pavlov, "Simulating CCDs for the Chandra Advanced CCD Imaging Spectrometer," *Nucl. Instr. and Meth. A*, vol. 486, p. 716, 2002. 48

[90] O. Godet, P. Sizun, D. Barret, P. Mandrou, B. Cordier, S. Schanne and N. Remoue, "Monte-Carlo simulations of the background of the coded-mask camera for X-and Gamma-rays on-board the Chinese-French GRB mission SVOM," *Nucl. Instr. and Meth. A*, vol. 494, p. 775, 2009. 48

[91] J.R. Janesik, *Scientific Charge-Coupled Devices*. SPIE Press, Bellingham, WA. USA, 2001. 48

[92] C. Xu, M. Danielsson and H. Bornefalk, "Validity of spherical approximation of initial charge cloud shape in silicon detectors," *Nucl. Instr. and Meth. A*, vol. 648, p. S190, 2011. 48

[93] N. Bohr and K. Dan *Vidensk. Selsk. Mat. Fys. Medd.*, vol. 18, p. 1, 1948. 49

[94] H.H. Barrett and K.J. Myers, *pp 748-763*. Wiley Interscience, John Wiley and Sons, Inc., 2004. 50

[95] Y. Fang, A. Badal, N. Allec, K. S. Karim and A. Badano, "Spatiotemporal Monte Carlo transport methods in x-ray semiconductor detectors: Application to pulse-height spectroscopy in a-Se," *Med. Phys.*, vol. 39, pp. 308–319, 2012. 52, 75, 135

[96] W. M. Bartczak, M. P. DeHaas and A. Hummel, "Computer simulation of the recombination of the ions in tracks of high-energy electrons in nonpolar liquids," *Radiat. Phys. Chem.*, vol. 37, pp. 401–406, 1991. 59, 60

[97] W. M. Bartczak and A. Hummel, "Computer simulation of ion recombination in irradiated non-polar liquids," *J. Chem. Phys.*, vol. 87, p. 52222, 1987. 59, 60

[98] W. M. Bartczak and A. Hummel, "Computer simulation study of spatial distribution of ions and electrons in tracks of high-energy electrons and the effect on the charge recombination," *J. Phys. Chem.* , vol. 97, p. 1253, 1993. 59, 60

[99] W. M. Bartczak and A. Hummel, ""Monte Carlo calculation of diffusion-controlled ion recombination for single and multiple ion pairs in a nonpolar liquid," *International Journal of radiation applications and instrumentation*, vol. 27, p. 71, 1986. 59, 60

[100] S.O. Kasap and J.A. Rowlands, "Review X-ray photoconductor and stabilized a-Se for direct conversion digital flat-panel- X-ray image-detectors," *J. Mat. Sci.*, vol. 11, p. 179, 2000. 60

[101] "Radioactive decay data," www.ie.ibl.gov/decay.html. 66

[102] "Medical diagnosis X-ray equipment - Radiation conditions for use in the determination of characteristics," Tech. Rep. International Standard IEC 61267, 2005. 72, 96

[103] Y. Fang, A. Badal, K.S. Karim and A. Badano, "Spatio-temporal Monte Carlo modeling of a-Se detectors for breast imaging: energy-weighted Swank noise and detective quantum efficiency," *Proc. SPIE*, vol. 8313, p. 8313S, 2012. 75

[104] L. Onsager, "Initial recombination of ions," *Phys. Rev.*, vol. 54, p. 554, 1938. 82

[105] J. Hirsch and H. Jahankhani, "The carrier yield in a-Se under electron-bombardment," *J. Phy. Cond. Matt.*, vol. 45, p. 8789, 1989. 82

[106] Y. Fang, D. Sharma, A. Badal, K.S. Karim and A. Badano, "Monte Carlo simulations of a-Se x-ray detectors for breast imaging: Effect of nearest-neighbor recombination algorithm on Swank noise," *Proc. IWDM*, p. 575, 2012. 87

[107] Y. Fang, K.S. Karim and A. Badano, "Burst and recombination models for spatiotemporal Monte Carlo transport of interacting carriers in a-Se semiconductor x-ray detectors," *Submitted to Med. Phys.* 90

[108] K. Irisawa, K. Yamane, S. Imai, M. Ogawa, T. Shouji, T. Agano, Y. Hosoi and T. Hayakawa, "Direct-conversion 50 μm pixel-pitch detector for digital mammography using amorphous selenium as a photoconductive switching layer for signal charge readout," *Proc. SPIE*, vol. 7258, p. 72581I, 2009. 94

[109] G. Zentai, L. Partain, M. Richmond, K. Ogusu and S. Yamada, "50 μm pixel size a-Se mammography imager with high DQE and increased temperature resistance," *Proc. SPIE*, vol. 8453, 2010. 94

[110] G. Hajdok, J.J. Battista and I.A.Cunningham, "Fundamental x-ray interaction limits in diagnostic imaging detectors: Spatial resolution," *Med. Phys.*, vol. 35, p. 3180, 2008. 94

[111] G. Hajdok, J. Yao, J.J. Battista and I.A.Cunningham, "Signal and noise transfer properties of photoelectric interactions in diagnostic x-ray imaging detectors," *Med. Phys.*, vol. 33, p. 3601, 2006. 94

[112] G. Hajdok, J.J. Battista and I.A.Cunningham, "Fundamental limitations imposed by x-ray interactions on the modulation transfer function of existing x-ray detectors," *Proc. SPIE.*, vol. 5030, 2003. 94

[113] Y. Fang, A. Badal, A. Badano, and K.S. Karim, "Spatial resolution characteristics of a-Se imaging detectors using spatiotemporal Monte Carlo methods with detailed transport of x rays, electrons and electron-hole pairs under applied bias," *Proc. SPIE.*, vol. 8668, p. 86683R, 2013. 94

[114] H.H. Barrett and K.J. Myers, *pp 709, 1114-1115*. Wiley Interscience, John Wiley and Sons, Inc., 2004. 94

[115] J.C. Dainty and R. Shaw, *Image Science*. Academic Press, New York, 1974. 95

[116] R. Shaw, "The equivalent quantum efficiency of the photographic process," *J. Photogr. Sc.*, vol. 11, p. 199, 1963. 95

[117] F. Nariyuki, S. Imai, H. Watano, T. Nabeta and Y. Hosoi, "New development of large-area direct conversion detector for digital radiography using amorphous selenium with a C60-doped polymer layerNew development of large-area direct conversion detector for digital radiography using amorphous selenium with a C60-doped polymer layer," *Proc. SPIE*, vol. 7622, p. 762240, 2010. 95, 133